Solubilisation of carbon nanotubes with a non-conjugated polymer for device applications

Giulio Mazzotta

University College

A thesis submitted for the degree of

Doctor of Philosophy

at the University of Oxford

Trinity Term 2018

Solubilisation of carbon nanotubes with a non-conjugated polymer for device applications

Giulio Mazzotta, University College

A thesis submitted for the degree of *Doctor of Philosophy*
at the University of Oxford.

Trinity Term 2018

Abstract

Carbon nanotubes (CNT) solubilisation represents a major challenge for their use on a large scale in electronic devices, as CNT's tendency to aggregate prevents an easy and uniform deposition of CNT films. This thesis demonstrate a novel way to solubilise CNTs using the non-conjugated polymer ethylene-vinyl acetate (EVA). The characterisation of the optical and electrical properties of the resulting EVA-CNT nano-hybrids is analysed, and their performance as a holes extraction layer in photovoltaic devices discussed.

First, it is shown that EVA can solubilise single- and multi-walled carbon nanotubes, and by photoluminescence excitation mapping is demonstrated that the polymer creates a strong binding with the CNT inducing a mechanical stress. Raman spectroscopy studies show a non-selective wrapping process, with a tendency to wrap more metallic CNTs. By atomic force microscopy it is confirmed that the nanotubes are individually wrapped. This causes the screening of the aggregation forces in solution and enables the production of uniform and aggregate-free dispersions.

These dispersions allow the fabrication of uniform thin films by spray-coating, conducting and semi-transparent, with conductivities of up to 34 S/cm, two higher of magnitudes ever reached for this combination of materials. The films have been the subject of percolation studies, showing that the films with increasing density show an increase in conductivity which can be well fitted by the expected behaviour for a 2D percolation model.

Finally, to test the electronic properties of such produced CNT films in devices, they have been used as hole transporting layers in perovskite solar cells. It is shown that despite the insulating polymer wrapping the nanotubes, it is possible to use them in conjunction with undoped 2,2',7,7'-Tetrakis[N,N-di(4-methoxyphenyl)amino]-9,9'-spirobifluorene (spiro-OMeTAD) to efficiently extract charges from the perovskite layer, obtaining solar cells with a power conversion efficiency of 16.8% with EVA-SWCNTs. and 17.3% with EVA-MWCNTs. With further optimisation it is expected that they can replace CNT wrapped with conjugated polymers, offering favourable optical properties at lower cost.

Acknowledgments

A DPhil thesis is the end of a very challenging journey, mentally demanding and physically tiring too sometimes, especially when your labs are spread across two buildings and three floors. This work describes what I have learnt and discovered from a scientific point of view, and a big part of this result has undoubtedly been achieved thanks to the amazing people I have met during these years in Oxford. Writing these few lines to acknowledge everyone who helped me directly or indirectly (with apologies to people I will inevitably forget) is really a duty, as it is the very minimum to recognise their contribution to this work.

I would like to thank my supervisors, Prof Robin Nicholas and Dr Moritz Riede, for the invaluable guidance offered during these years. I was once asked to choose a "main" and a "second" supervisor. I panicked and avoided answering, and even today I wouldn't be able to choose. They both gave me absolute freedom to follow my curiosity, their doors have always been open for any discussion, and their advice has always been extremely helpful, both on an academic and a personal level.

As a consequence of having two supervisors, I was lucky enough to have two homes in the department. Thanks to the AFMD group for being one of the two, and especially to the early members - Ivan and Josué. During my first week in the department Ivan showed me the lab. I had to wear a high vis jacket and a helmet, as I was brought into an empty room with construction works. Starting a lab from scratch was fun but extremely stressful, and sharing all the laughing, crying, building and destroying with two friends made it a very special experience. Thankfully the group expanded soon with amazing new members, so I would like to thank Grey (like the colour), Ross, Hanyang, Sameer, Anna, Andreas and Alberto for making this group a wonderful environment, both on a working and a non-working level.

Thanks then to my other home, the RJN group, especially to Severin for teaching me everything I know about carbon nanotubes and sharing with me too many coffees

in Korea, Markus for sharing chats, lunches and beers, and Nate for pointing the right cupboard every time I needed something.

In addition to two amazing homes, I had amazing neighbours. Thanks to the HJS group for sharing spaces, science and breaks. Especially to Prof Henry Snaith for letting me use his labs and throwing me numerous ideas, to Clare for being the solution to all the CDT-related problems, and to Ping for providing me with extremely good devices to test my carbon nanotubes. A special thanks also to the HJS group members (and adopted) for all the coffee breaks and the unforgettable dinners and nights out: Derek, Max, David, Alba, Kita, Jay, Martina, Jong, Fede, Jonny, Olivia, Alex and many others. They have been fundamental to my survival up to this point.

A lot of indirect help came from outside the department. Thanks to the CDT-PV cohort 1, for sharing with me a crazy training programme around England, and providing me with some of the best memories from my first year. Thanks to Franco, a friend I can always count on for the usual Sunday evening beer, chatting about our projects and our futures. Thanks to my housemates James and Shane, for dealing with my moaning every time they (tried to) cook Italian food and for teaching me most of what I know about British culture. Thanks to Barclay for feeding me once per week in the coolest supper club in Oxford. Thanks to my College friends, especially from the Boat Club, for helping me to run away from the lab and switch off my brain when needed.

Spiritual help is paramount, but if I have been able to eat and sleep under a roof I also need to acknowledge the EPSRC and the Oxford Physics Department for a part of my funding, and University College for the Oxford-Radcliffe scholarship.

And finally but most importantly thanks to my family, for having built the foundations that made everything possible. Fighting to get a DPhil can be very stressful, nevertheless I always pride myself on being calm and relaxed all the time. This probably wouldn't be the case without the knowledge that it doesn't matter how bad things can go, I will always find help and shelter at home.

Contents

List of Figures

List of Tables

List of Publications

J. F. M. Hardigree, I. R. Ramirez, G. Mazzotta, C. Nicklin, and M. Riede, "In-situ observation of stacking fault evolution in vacuum-deposited C_{60}", *Applied Physics Letters* 111, 233305 (2017).

F. Pulvirenti, B. Wegner, N. K. Noel, G. Mazzotta, R. Hill, J. Patel, L.M. Herz, M.B. Johnston, M.K. Riede, H.J. Snaith, N. Koch, S. Barlowa and S.R. Marder, "Modification of the fluorinated tin oxide/electron-transporting material interface by a strong reductant and its effect on perovskite solar cell efficiency", *Molecular Systems Design & Engineering*, 2018, 3, 741-747.

Y. Tazawa, S. N. Habisreutinger, N. Zhang, G. Nagamine, S. V. Kesava, G. Mazzotta, H.E. Assender, M. Riede, L. A. Padilha, R. J. Nicholas, A.A.R. Watt, "Carbon Nanotubes for Quantum Dot Photovoltaics with Enhanced Light Management and Charge Transport", *ACS Photonics* 2018, 5, 12, 4854-4863.

G. Mazzotta, M. Dollmann, S. N. Habisreutinger, M.G. Christoforo, Z. Wang, H.J. Snaith, M.K.Riede, R.J. Nicholas, "Solubilization of carbon nanotubes with ethylene-vinyl acetate for solution-processed conductive films and charge extraction layers in perovskite solar cells", *ACS Applied Materials & Interfaces* 2019, 11, 1, 1185-1191.

J.F.M. Hardigree, I.R. Ramirez, G. Mazzotta, P.Ufimkin, P.Tiwana, G.E. Morse, J.R. Rawle, C. Nicklin, O.R. Lozman, and M.K. Riede, "Relating Microstructural Evolution to the Open-Circuit Voltage of Polymer Bulk-Heterojunction Solar Cells", in preparation.

List of Abbreviations

AFM atomic force microscopy

ALD atomic layer deposition

c-AFM conductive AFM

CCVD Catalytic Chemical Vapor Deposition

CNT carbon nanotube

CoMoCAT Cobalt–Molybdenum catalysts

CT charge transfer

D_2O deuterium oxide

DNA deoxyribonucleic acid

DMF N,N-dimethylformamide

DOS density of states

dsDNA double-strand DNA

E_G energy bandgap

EQE external quantum efficiency

EVA ethylene-vinyl acetate

F8BT poly[(9,9-dioctylfluorenyl-2,7- diyl)-alt-co-(1,4-benzo-2,1,3-thiadiazole)

FA formamidinium

FF fill factor

FTIR Fourier-transform infrared spectroscopy

FTO fluorine-doped tin oxide

HiPCO high-pressure carbon monoxide disproportionation

HOMO highest occupied molecular orbital

ITO indium-doped tin oxide

J_{SC} short-circuit current

Li-TFSI lithium bis(trifl uoromethanesulfonyl)imide

LUMO lowest unoccupied molecular orbital

MA methylammonium

MPP maximum power point

MWCNT multi-walled carbon nanotube

NMP N-methylpyrrolidinone

O-DCB o-dichlorobenzene

P3HT poly(3-hexylthiophene)

P3AT poly(3-alkylthiophene)

PBD poly-butadiene

PC polycarbonate

$PC_{60}BM$ phenyl-C61-butyric acid methyl ester

PCE power conversion efficiency

PEDOT:PSS poly(3,4-ethylenedioxythiophene) polystyrene sulfonate

PEO poly(ethylene oxide)

PFO poly(9,9-dioctyl-fluorenyl-2,7-diyl)

PI polyisoprene

PL photoluminescence

PLE photoluminescence excitation

PMMA poly(methyl methacrylate)

PmPV poly[(m-phenylenevinylene)-co-(2,5-dioctoxy-p-phenylenevinylene)]

PPV poly(p-pheny-lenevinylene)

PS polystyrene

RBM radial breathing mode

RSS resonant Raman scattering

SDBS sodium dodecylbenzenesulfonate

SDS sodium dodecyl sulfate

spiro-OMeTAD 2,2',7,7'-Tetrakis[N,N-di(4-methoxyphenyl)amino]-9,9'-spirobifluorene

SPO steady-state power output

SRH Shockley-Read-Hall

ssDNA single-strand DNA

SWCNT single-walled carbon nanotube

tBP 4-*tert* butylpyridine

TCSPC time-correlated single photon counting

V$_{MPP}$ maximum power point voltage

V$_{OC}$ open circuit voltage

WVTR water vapour transmission rate

CHAPTER 1

Introduction

1.1 Nanotechnology and carbon nanotubes

On the 29th December 1959, Richard Feynman gave a talk at the American Physical Society meeting at the California Institute of Technology titled "There's Plenty of Room at the Bottom",[1] which is symbolically regarded by many as the start of the field of nanotechnology. Starting from the 80s the field moved from ideas and concepts from a lecture to the actual ability to study and manipulate matter on the atomic scale.

Nanotechnology played an important role in the last decades, bringing advances in many fields including medicine, telecommunications, electronics, drastically accelerate the development of the society. The field of nanotechnology is highly interdisciplinary, linking the competences of chemists, physicists, biologists, material scientists and medics.

Carbon nanotubes, long carbon based tubes with a diameter in the order of few nanometers and length of several micrometers, belong to this class of technologies.

Studied from the 90s with the seminal work of Sumio Iijima at NEC,[2] carbon nanotubes have attracted a big interest for their unique mechanical and electronic properties, with numerous potential technological applications including transistors, thermal conductors, fibres and fabrics, structural reinforcements, drug delivery, energy production and storage, and several Nobel prizes have been awarded for research in this field.

Despite many prototypes have been produced, their commercialisation has been hindered by technological challenges, including the challenges in processing CNTs on large scale due to the difficult handling in their dry form and their poor solubility in common solvents, which would be needed for deposition.

As it will be described in more detail in Chapter 2, many approaches to solubilise CNTs have been developed, but these are often too expensive or introduce detrimental effects for the electronic properties of CNTs. In this context, this thesis investigates the use of a common, inexpensive polymer, EVA to solubilise carbon nanotubes in organic solvents to enable a facile large-scale deposition from solution for device applications.

1.2 Structure of this thesis

This thesis will describe the result of investigations on the use of a non-conjugated polymer, ethylene-vinyl acetate (EVA), to solubilise CNTs and produce thin films for electronic devices, with a specific application in solar energy cell technologies.

Chapter 2 and 3 will give an introduction to the relevant scientific knowledge, strating with describing CNTs in Chapter 2 from a theoretical point of view. Starting point is the graphene lattice, and it will be shown how CNTs optoelectronic properties are strictly related to their geometry. A brief overview of the optical characterisation will be presented, and a discussion on their electrical properties illustrated. Finally, the problem of the carbon nanotubes solubilisation for large-scale deposition will be discussed, with an overview of the main methodologies to achieve uniform dispersions to date.

Chapter 3 will briefly summarise the physics of semiconductors and their use in photovoltaic devices. A particular focus will be put on perovskite devices, and specifically on the use of carbon nanotubes in these devices.

Chapter 4 will describe the further materials used in this work, the fabrication procedures of film and devices and the characterisation techniques.

The experimental work is starting from Chapter 5, which will focus on the studies on the solubilisation of CNTs with the non-conjugated EVA polymer, and the fabrication of EVA-CNT nano-hybrids, with a characterisation with photoluminescence excitation (PLE) spectroscopy, Raman spectroscopy and atomic force microscopy.

Studies on the electrical properties of this films produced with EVA-CNT nano-hybrids will be shown in 6, where percolation studies on film with different densities are illustrated, and optical and electrical measurements are used to characterise the films.

Chapter 7 will demonstrate how the use of the EVA-CNT nano-hybrids in photovoltaic devices and how well they perform. For this, perovskite solar cells employing them as hole transporting layer are fabricated and characterised.

Finally, Chapter 8 will summarise the key findings, and present the scope for future work.

Bibliography

1. R. P. Feynmann, "There's Plenty of Room at the Bottom," *Engineering & Science Magazine*, vol. 23, no. 5, pp. 22–36, 1960.

2. S. Iijima, "Helical microtubules of graphitic carbon," *Nature*, vol. 354, no. 6348, pp. 56–58, 1991.

CHAPTER 2

Carbon nanotubes

This section gives a brief introduction to the characteristics of CNTs, with a specific focus on the properties most relevant to the experimental work of this thesis. It is largely based on the books of Saitō, R, Dresselhaus, G, and Dresselhaus, MS, *Physical Properties of Carbon Nanotubes*, 1998, Imperial College Press[1] and of Jorio, A, Dresselhaus, MS, and Dresselhaus, G, *Carbon Nanotubes: Advanced Topics in the Synthesis, Structure, Properties and Applications*, 2008, Springer[2] which can be used as a reference for a more comprehensive description.

2.1 Single-Walled Carbon Nanotubes

2.1.1 Crystal structure

CNTs are cylindrical allotropes of carbon. They are categorized as SWCNTs when made of a single cylinder, and MWCNTs when made of several concentric cylinders. The simplest way of describing the structure of SWCNTs is by starting with the

description of graphene. Graphene is a covalent solid made of carbon atoms arranged in a honeycomb structure, forming a triangular lattice having two carbon atoms per unit cell, which is the two-dimensional rhombus having the unit vectors as sides, as represented in Figure 2.1. The unit vectors are defined in Cartesian coordinates as

$$\mathbf{a}_1 = a_0 \left(\frac{\sqrt{3}}{2}, \frac{1}{2} \right) ; \mathbf{a}_2 = a_0 \left(\frac{\sqrt{3}}{2}, -\frac{1}{2} \right) \tag{2.1}$$

.

where $a_0 = \sqrt{3} a_{C-C} = 0.249$ nm is the lattice constant and $a_{C-C} = 0.144$ nm is the $C - C$ bond length (This is $a_{C-C} = 0.142$ nm in graphite,[3] but slightly larger in CNTs depending on the curvature, typically $a_{C-C} = 0.144$ nm[1]). These two vectors have a length of $|\mathbf{a}_1| = |\mathbf{a}_2| = a_0 = 0.249$ nm and open at an angle of 60°.

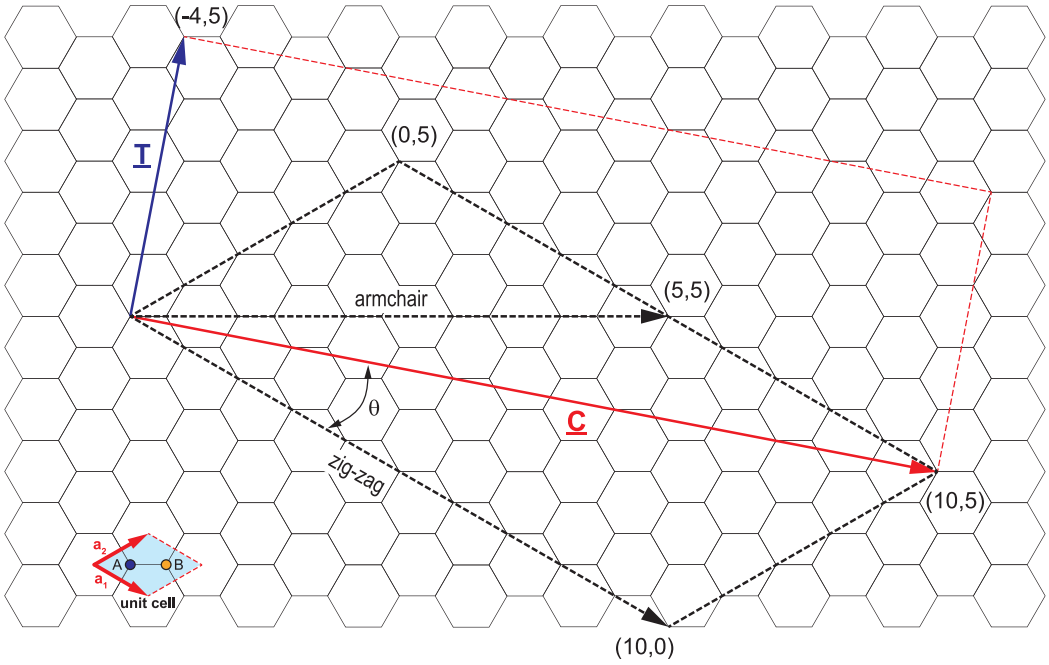

Figure 2.1: Costruction of a (10,5) SWCNT on a graphene sheet. $\mathbf{a}_1$ and $\mathbf{a}_2$ are the unit vectors of the crystal. The chiral vector **C** can be written with the unit vectors as $\mathbf{C} = 10\mathbf{a}_1 + 5\mathbf{a}_2$, and the perpendicular translational vector **T** is given by $\mathbf{T} = -4\mathbf{a}_1 + 5\mathbf{a}_2$. The tube is constructed cutting the graphene sheet along the **T** vector and the blue dashed line, and rolling up the sheet to have the **C** vector as the diametre of the tube. The angle θ between the $\mathbf{a}_1$ and the **C** defines the chiral angle. The chiral vectors of the special cases of a zig-zag tube (10,0) and an armchair tube ((5,5) are also represented.

CNTs can be constructed by defining a vector **C** joining two equivalent points on

the graphene lattice and rolling up the sheet such that its end points are superimposed. The **C** vector can be written as

$$\mathbf{C} = n\mathbf{a}_1 + m\mathbf{a}_2 \tag{2.2}$$

where $n \geq m$ are the chiral indices, which uniquely define a carbon nanotube and its properties.

The magnitude of the **C** vector is

$$|\mathbf{C}| = a_0\sqrt{n^2 + nm + m^2} \tag{2.3}$$

and the diameter of the tube is

$$d_t = \frac{a_0\sqrt{n^2 + nm + m^2}}{\pi} \tag{2.4}$$

.

The chiral angle θ is defined as the angle between the **C** and $\mathbf{a}_2$ vectors, and denotes the tilt of the hexagonal helix with respect to the axis of the tube. It is defined as

$$\cos\theta = \frac{\mathbf{C}\cdot\mathbf{a}_2}{|\mathbf{C}||\mathbf{a}_2|} = \frac{2n+m}{2\sqrt{n^2+m^2+nm}} \tag{2.5}$$

.

Due to the hexagonal symmetry of the honeycomb lattice all the unique tubes are described in the range $0° \leq |\theta| \leq 30°$, (*i.e.* $n \geq m \geq 0$). All the nanotubes with $0° < |\theta| < 30°$ exhibit a spiral symmetry. Their mirror image cannot be superposed to the original one, and they are called chiral nanotubes. The special case of achiral tubes are referred to "zig-zag" when $\theta = 0°$ ($m = 0$) and "armchair" when $\theta = 30°$ ($n = m$), and they take the name from the shape drawn by the carbon bonds as illustrated in Figure 2.2. An example of both is also represented on the graphene lattice of Figure 2.1.

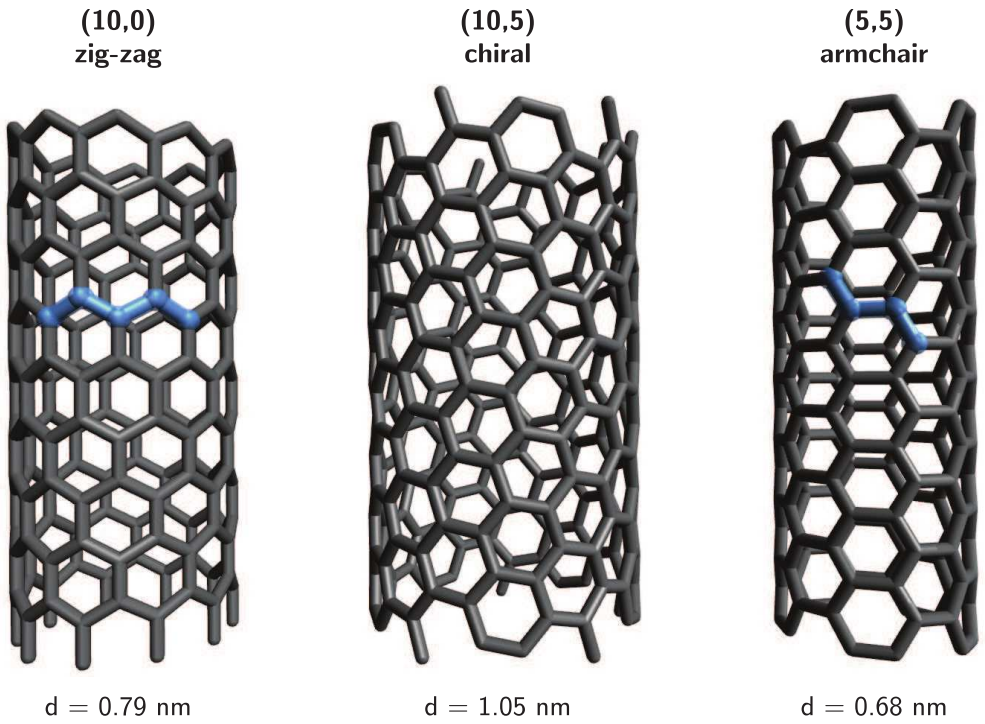

Figure 2.2: 3D representation of a *zig-zag* tube (10,0), a chiral tube (10,5) and an armchair tube (5,5). The blue marks highlight the geometry of the bonds that gives the name to the structure.

The rolled up sheet of graphene is also a crystal lattice. Its unit vectors are the above defined **C** vector and the translational vector

$$\mathbf{T} = t_1\mathbf{a}_1 + t_2\mathbf{a}_2. \tag{2.6}$$

This is perpendicular to the **C** vector, (*i.e.* parallel to the tube axis) and its length is defined by the smallest translational period along the tube axis. It is possible to calculate the coefficients t_1 and t_2 using the condition $\mathbf{C} \cdot \mathbf{T} = 0$ giving

$$t_1 = \frac{2m+n}{N_R}, t_2 = -\frac{2n+m}{N_R} \tag{2.7}$$

where N_R is the greatest common divisor of $2m+n$ and $2n+m$, and the modulus of the vector is then

$$|\mathbf{T}| = \sqrt{3}|\mathbf{C}|/N_R \tag{2.8}$$

The unit cell of the lattice is the cylinder of diameter d_t and height $|\mathbf{T}|$. Dividing the area of the unit cell by the area of the hexagon, it is possible to obtain the number of hexagons per unit cell

$$N_{hex} = \frac{|\mathbf{C} \times \mathbf{T}|}{|\mathbf{a}_1 \times \mathbf{a}_2|} = \frac{2(m^2 + n^2 + nm)}{N_R} \tag{2.9}$$

and having 2 carbon atoms per hexagon, there are $2N_{hex}$ carbon atoms per unit cell (*i.e.* $2p_z$ orbitals).

An example is shown in Figure 2.1, where the construction of a (10,5) tube is shown. The $\mathbf{C} = 10\mathbf{a}_1 + 5\mathbf{a}_2$ vector is shown in red, and the corresponding $\mathbf{T} = -4\mathbf{a}_1 + 5\mathbf{a}_2$ in blue. The chiral angle is drawn between the (0,5) vector, parallel to $\mathbf{a}_2$ and the $\mathbf{C}$ vector.

Having defined the graphene sheet and the carbon nanotube in the real space, it is now possible to calculate the first Brillouin zone in the reciprocal space. Starting with the graphene sheet, the reciprocal lattice of a hexagonal lattice is again hexagonal, and the reciprocal primitive vectors $\mathbf{k}_1$ and $\mathbf{k}_2$ can be calculated from the relation $\mathbf{a}_i \cdot \mathbf{k}_j = 2\pi\delta_{ij}$, leading to

$$\mathbf{k}_1 = \frac{4\pi}{\sqrt{3}a_0}\left(\frac{1}{2}, \frac{\sqrt{3}}{2}\right); \mathbf{k}_2 = \frac{4\pi}{\sqrt{3}a_0}\left(\frac{1}{2}, -\frac{\sqrt{3}}{2}\right) \tag{2.10}$$

Similarly, for the nanotube the reciprocal lattice vectors $\mathbf{k}_\parallel$ and $\mathbf{k}_\perp$ can be defined using the relations

$$\mathbf{C} \cdot \mathbf{k}_\parallel = 2\pi, \qquad \mathbf{T} \cdot \mathbf{k}_\parallel = 0, \tag{2.11}$$

$$\mathbf{C} \cdot \mathbf{k}_\perp = 0, \qquad \mathbf{T} \cdot \mathbf{k}_\perp = 2\pi. \tag{2.12}$$

getting

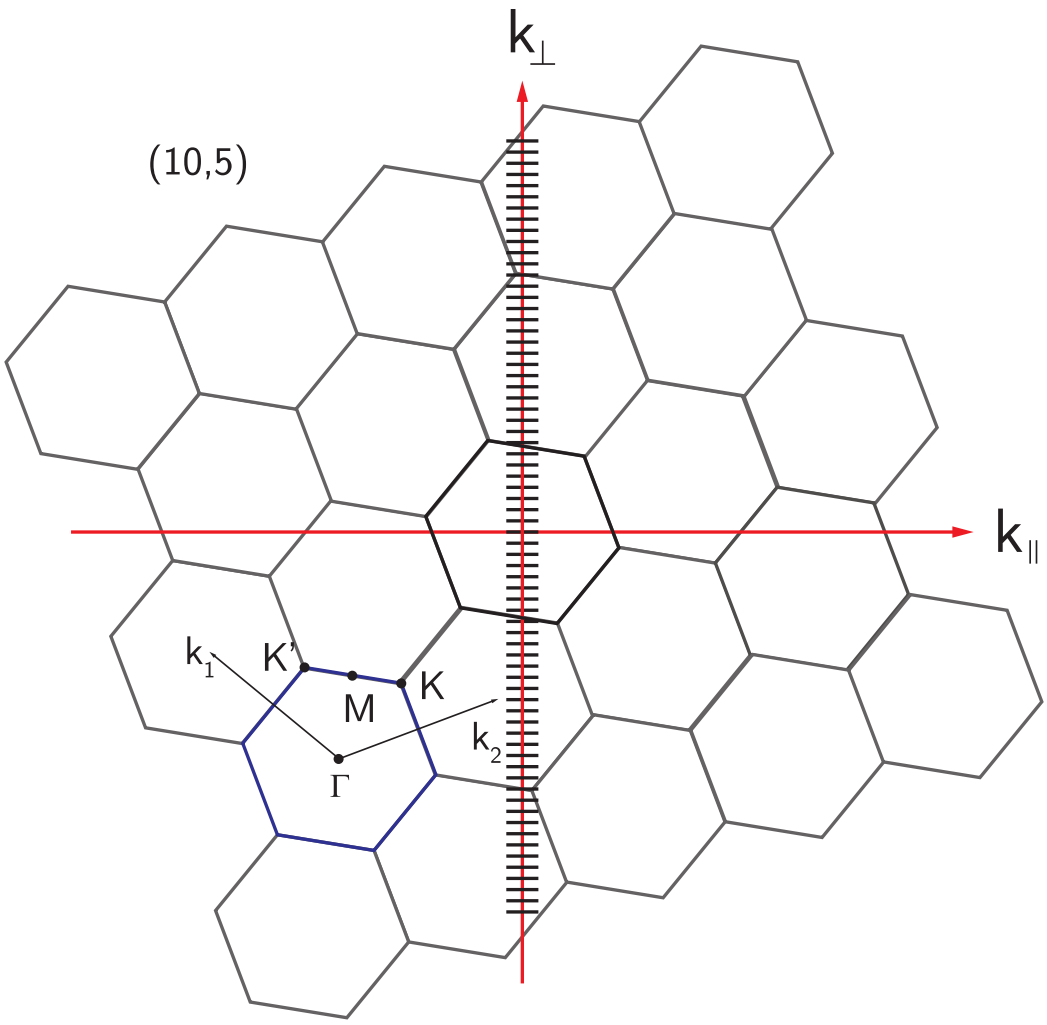

Figure 2.3: Brilloin zone of a (10,5) carbon nanotube. The vectors $\mathbf{k}_\perp$ and $\mathbf{k}_\parallel$ are the reciprocal vectors of **C** and **T**. The allowed wavevectors are the $N_{hex} = 70$ segments along the $\mathbf{k}_\perp$ vector, having a length of $2\pi/T$ and spanning a distance of $2N_{hex}/d_t$. The Brilluoine zone of graphene is also shown in the blue hexagon with the two reciprocal vectors k_1 and k_2, and the high symmetry points Γ, M, K and K'.

$$\mathbf{k}_\parallel = \frac{1}{N_{hex}}\left(\frac{2n+m}{N_R}\mathbf{k}_1 + \frac{2m+n}{N_R}\mathbf{k}_2\right), \mathbf{k}_\perp = \frac{1}{N_{hex}}\left(-m\mathbf{k}_1 + n\mathbf{k}_2\right), \tag{2.13}$$

The reciprocal of the translational vector $\mathbf{k}_\parallel$ is continuous as the carbon nanotube is regarded as infinitely long and its length is $|\mathbf{k}_\parallel| = 2\pi/a_0$. The $\mathbf{k}_\perp$ is quantized due to the Born–von Karman boundary conditions, as the wave functions of particles in nanotubes around the circumference with a phase shift different from 2π vanish due

to destructive interference, which correspond to imposing the condition

$$i \cdot \lambda = |\mathbf{C}| = \pi \cdot d_t \Longleftrightarrow |\mathbf{k}_\perp| = \frac{2\pi}{\lambda} = \frac{2\pi}{|\mathbf{C}|} \cdot i = \frac{2}{d_t} \cdot i. \tag{2.14}$$

where i takes values $\{-N_{hex}/2+1, -N_{hex}/2+2, ..., -1, 0, 1, ..., N_{hex}/2\}$. The only allowed wavevectors along the $\mathbf{k}_\perp$ direction are then discrete lines spaced at a distance of $2/d_t$ apart. The resulting Brillouin zone is then made of N_{hex} parallel segments with a length of $2\pi/T$ covering a total distance of $2N_{hex}/d_t$.

This is shown in Figure 2.3 for a (10,5) tube. The allowed momenta are represented by the $N_{hex} = 70$ segments along the $\mathbf{k}_\perp$ direction, whose relative direction in respect of the graphene reciprocal lattice is given by Equation 2.13.

2.1.2 Electronic structure

Energy dispersion relations

The energy dispersion relations of CNT can be derived using again graphene as a starting point. In graphene three sp^2 hybridised carbon orbitals per atom form very strong localised σ bonds. These are responsible for the mechanical properties of graphene and do not contribute to the conduction.

The remaining p_z orbitals are perpendicular to the graphene plane and can be treated independently for symmetry reasons. The overlap of each p_z orbital with their neighbours forms de-localised π (bonding) and π^* (anti-bonding) orbitals responsible for the electronic properties of the material.

Due to the weak coupling of the p_z orbitals, the electrons are tightly bound to their respective atoms, allowing the derivation of the band structure by a tight binding approximation for the π-electrons as originally shown by Wallace[3].

With this approximation the dispersion relation can be written as[4]

$$E_{2D}^{\pm} = \frac{\epsilon_2 p \mp \gamma_0 \sqrt{f(\mathbf{k})}}{1 \mp s_0 \sqrt{f(\mathbf{k})}} \tag{2.15}$$

where $\epsilon_2 p$ is the site energy of the $2p_z$ orbitals, γ_0 is the transfer integral (*i.e.* the carbon-carbon interaction energy) and and s_0 is the overlap integral between a carbon atom and one of its neighbours.

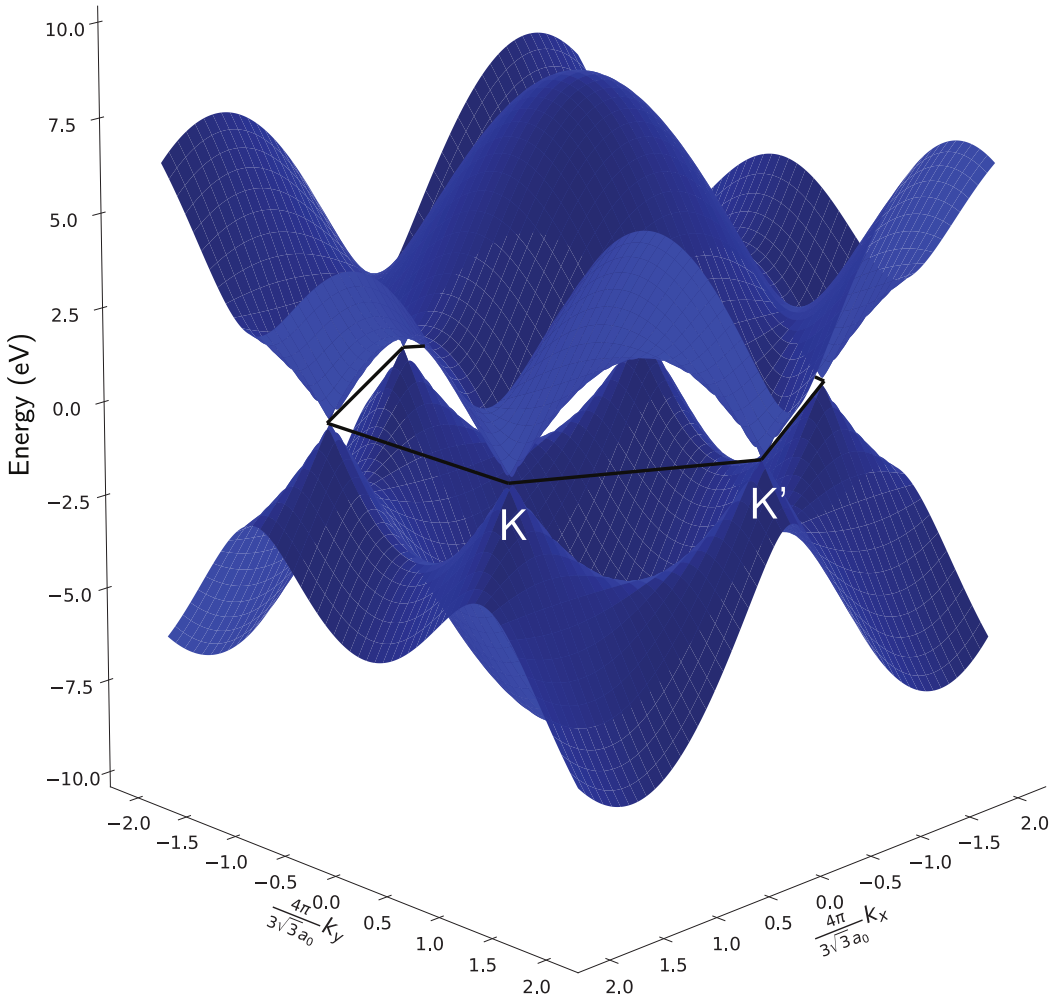

Figure 2.4: 3D plot of the $E_{2D}^{\pm}$ bands (Eq. 2.15) for graphene calculated with the tight-binding approximation. The bonding and anti-bonding bands (π and $\pi*$) cross over at the K points, resulting in a metallic character.

$$f(\mathbf{k}) = 3 + 2\cos(\mathbf{k}\cdot\mathbf{a}_1) + 2\cos(\mathbf{k}\cdot\mathbf{a}_2) + 2\cos[\mathbf{k}(\mathbf{a}_1 - \mathbf{a}_2)] \tag{2.16}$$

which can be rewritten in terms of k_x and k_y coordinates as

$$f(k_x, k_y) = \sqrt{1 + 4\cos\left(\frac{\sqrt{3}k_x a_0}{2}\right)\cos\left(\frac{k_y a_0}{2}\right) + 4\cos^2\left(\frac{k_y a_0}{2}\right)} \tag{2.17}$$

The band structure of graphene can now be used to describe the structure of single-walled CNTs using the *zone-folding* approximation. This is done by overlaying the discrete $\mathbf{k}_\perp$ vectors of the SWCNT described in the previous section onto the Brillouin zone of graphene. The bands of SWCNTs are then described as the cross sections along these allowed momenta, and are given by:

$$E^{\pm}_{SWCNT}(i, k_\parallel) = E^{\pm}_{2D}\left(i\mathbf{k}_\perp + k_\parallel \frac{\mathbf{k}_\parallel}{|\mathbf{k}_\parallel|}\right), \tag{2.18}$$

where i takes values $\{-N_{hex}/2 + 1, -N_{hex}/2 + 2, ..., -1, 0, 1, ..., N_{hex}/2\}$ and $-\frac{\pi}{a} \leq k_\parallel \leq \frac{\pi}{a}$

It is important to note that the orientation and number of the discrete *k* lines change depending on the nanotube geometry. As it can be seen from Figure 2.4, if these cross the K point of the graphene Brilloin zone, the valence and conduction bands will cross at this point and the tube will be metallic. In all the other cases there will be a band gap, and the tube will be semiconducting. This is illustrated in Figure 2.5 for (5,5) metallic and (10,0) semiconducting nanotubes.

Analytically we will have an allowed wave vector passing through the K point when

$$\mathbf{K} \cdot \mathbf{C} = 2\pi \cdot p, \qquad p \in \mathbb{N} \tag{2.19}$$

and substituting the position of the K point $\mathbf{K} = \frac{1}{3}(\mathbf{k}_1 - \mathbf{k}_2)$ we get

$$\frac{1}{3}(\mathbf{k}_1 - \mathbf{k}_2) \cdot (m\mathbf{a}_1 + n\mathbf{a}_2) = 2\pi p \tag{2.20}$$

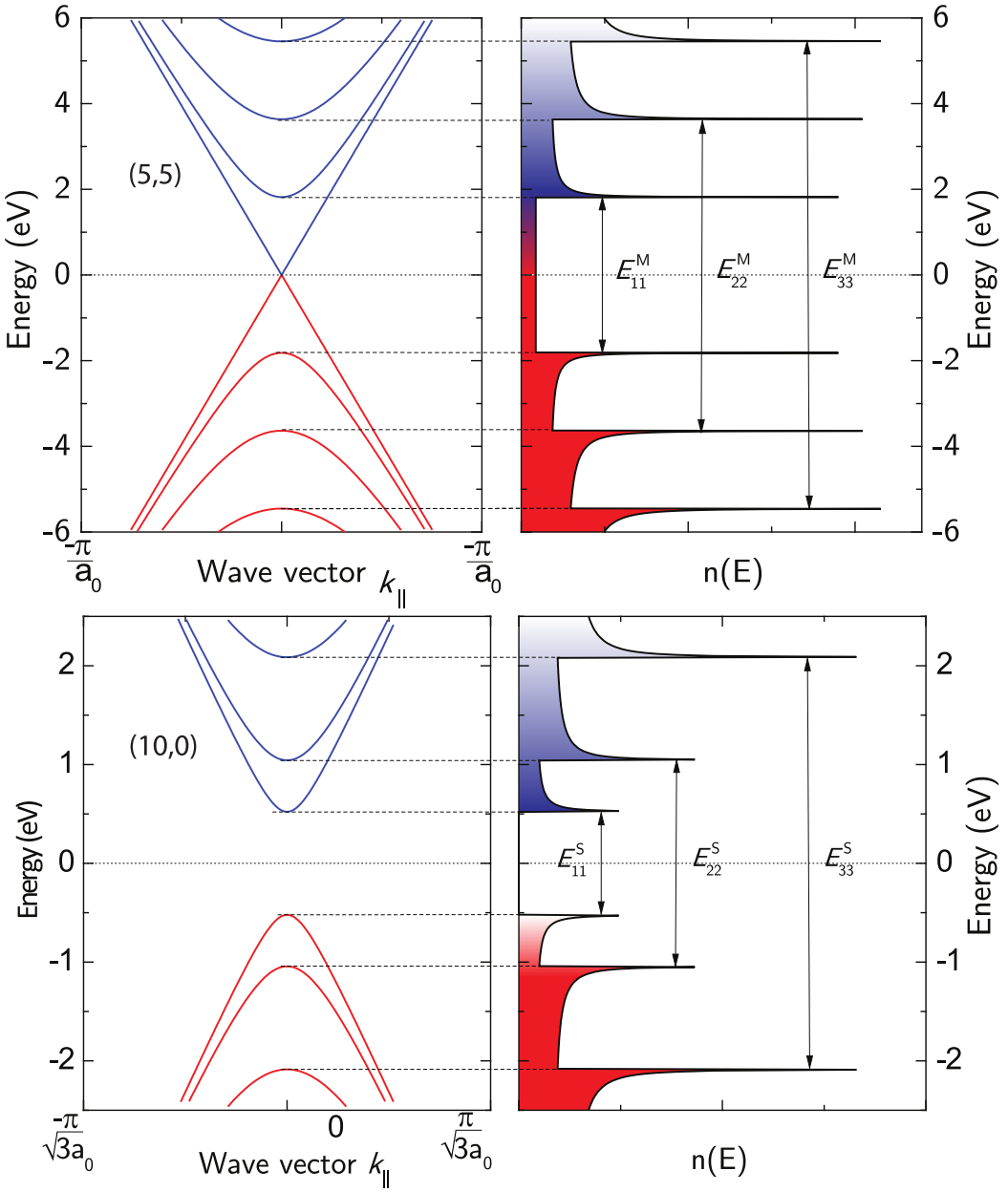

Figure 2.5: Band structure (left) and density of states (right) for a (10,0) semiconducting tube and a (5,5) metallic tube. The band structure is calculated with the tight-binding approximation of Eq. 2.18. The bands of the (10,0) tube cross at 0 eV, and this corresponds to a non-zero density of states around this energy. On the contrary, the (5,5) tube shows a bandgap, and consequently a region with no available states in the bandgap.

and since $\mathbf{a}_i \cdot \mathbf{k}_j = 2\pi\delta_{ij}$ we obtain

$$m - n = 3p \tag{2.21}$$

which means that a tube will be metallic if the difference of its chiral indeces is a multiple of three. This can be generalised to give

$$m - n = 3p + q, \quad q = \begin{cases} 0, & \text{metallic.} \\ \pm 1, & \text{semiconducting.} \end{cases} \tag{2.22}$$

From this follows that one third of all the nanotubes are metallic and the remaining $q = \pm 1$ correspond to two families of semiconducting nanotubes.

Density of states

The density of states (DOS) is the number of available sites for electron to occupy at a given energy. A general expression for the DOS of CNT was derived by Mintmire *et al.*[5] and is given by

$$n(E) = \frac{2}{Q|\mathbf{k}_\parallel|} \sum_j \int dk_\parallel \delta(k_\parallel - k_j) \left| \frac{\partial E^\pm(k_\perp, k_\parallel)}{\partial k_\parallel} \right|^{-1} \tag{2.23}$$

where k_j si given by $E - E^\pm(k_\perp, k_\parallel) = 0$ and

$$Q|\mathbf{k}_\parallel| = \frac{3\pi^2 d}{\sqrt{3}{a_0}^2} \tag{2.24}$$

To calculate the DOS for values of **k** near the Fermi level it is possible to expand the dispersion relation of graphene (Equation 2.15)

$$E^\pm \approx \pm \frac{\sqrt{3}}{2} a_0 \gamma_0 |\mathbf{k} - \mathbf{K}|. \tag{2.25}$$

Any distance between **k** to the nearest K point can be written as

$$|\mathbf{k}-\mathbf{K}| = \sqrt{{\Delta k_\perp}^2 + {\Delta k_\parallel}^2} \tag{2.26}$$

As described in section 2.1.1, $\Delta k_\parallel$ can have continuous values while $\Delta k_\perp$ is quantised and is given by the projection of $(\mathbf{k}-\mathbf{K})$ onto $\mathbf{k}_\perp$:

$$\Delta k_\perp = \left|(\mathbf{k}-\mathbf{K})\cdot\frac{\mathbf{k}_\perp}{|k_\perp|}\right| = \frac{2}{3d}|3i-q|, \tag{2.27}$$

where q is defined in Equation 2.22 and i takes integer values.

The derivative term can be written as

$$\left|\frac{\partial E^\pm(k_\perp,k_\parallel)}{\partial k_\parallel}\right|^{-1} = \left|\frac{\sqrt{3}}{2}a_0\gamma_0\frac{\partial\sqrt{{\Delta k_\perp}^2+{\Delta k_\parallel}^2}}{\partial k_\parallel}\right|^{-1} = \left(\frac{2}{\sqrt{3}a_0\gamma_0}\right)\frac{|E^\pm|}{\sqrt{(E^\pm)^2-{E_i}^2}}, \tag{2.28}$$

where

$$E_i = \frac{\sqrt{3}}{2}a_0\gamma_0\Delta k_\perp = |3i-q|\frac{a_0\gamma_0}{\sqrt{3}d}. \tag{2.29}$$

These expression can now be inserted in 2.23 and integrating over $k_\perp$ obtaining

$$n(e) = \frac{4a_0}{\pi^2 d\gamma_0}\sum_{i=-\infty}^{\infty} g(E,E_i), \quad g(E) = \begin{cases} \frac{|E|}{\sqrt{E^2-{E_i}^2}}, & |E|>|E_i| \\ 0, & |E|<|E_i|. \end{cases} \tag{2.30}$$

It can be seen that for $E=E_i$ the density of states diverges. These singularities are called *van Hove singularities*, and are given by $E_i = \frac{ia_0\gamma_0}{\sqrt{3}d}$ with $i=0,3,6,...$ for metallic and $i=1,2,4,5,7,...$ for semiconducting nanotubes. The bandgap for semiconducting tubes is then

$$E_{11} = 2E_1 = 2\frac{a_0\gamma_0}{\sqrt{3}d}. \tag{2.31}$$

An example of the DOS of a metallic and a semiconducting tube is represented in Figure 2.5, where the band structure and the density of states are represented for a (5,5) and a (10,0) tubes. While the metallic tube has a non-zero number of states for every value of the energy, the semiconducting tube has a gap with no available states of width E_{11}.

2.2 Optical properties

Absorption

Having described the density of states, it is now possible to study the optical transitions in CNT. The main allowed transitions occurs vertically (due to conservation of angular momentum) between bands with same index. They are labelled with E_{ii} and are allowed for light polarised parallel to the tube axis. Transitions for perpendicular polarization are allowed for bands that differ by one (*i.e.* $E_{i,i-1}$ or $E_{i-1,i}$), but these are strongly suppressed due to the large geometrical anisotropy (*Antenna effect*[6]).

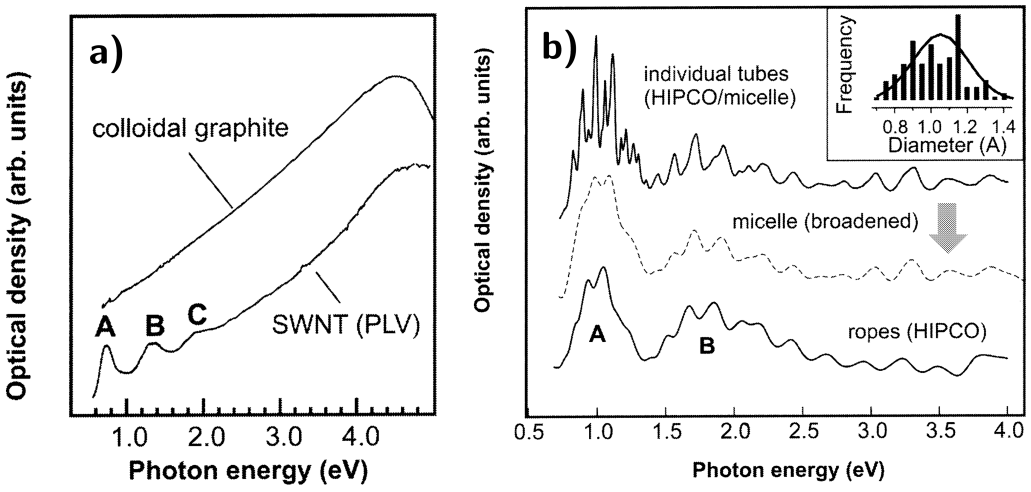

Figure 2.6: UV-VIS-NIR absorption of different SWCNT samples. (a) shows the comparison between colloidal graphite and rope materials of SWCNT (produced via Pulsed Laser Deposition). A, B, and C features can be attributed to symmetric transitions between the lowest subbands in semiconducting (A, B) and metallic (C) tubes. (b) Comparison of background-corrected spectra from SWCNT (produced with the HIPCO method) rope material with that of individual tubes in micelles. The inset shows the diameter distribution in the sample. Adapted with permission from reference [7]. Copyright 2003 American Chemical Society.

Despite the very sharp DOS, the peaks found experimentally in the absorption spectra of CNTs are generally very broad. This is due to the large heterogeneity of the sample, as it can normally consist of many different species (m, n) adding up to produce a broad peak. This is shown in Figure 2.6a, where the spectrum of CNTs is very similar to the one of graphite, with exception of the peaks below 2 eV, attributed to the lowest subbands in semiconducting (A, B) and metallic (C) tubes. In the case of samples with a few nanotubes species (as shown in the lowest curve of Figure 2.6b) peaks result quite broad due to bundling. An appropriate sample preparation (further details discussed in section 2.4) allows the separation of individual tubes and results in sharper peaks, as shown in Figure 2.6.

Photoluminescence

If the absorbed photons involve an excitation to states higher than $E_1^{\pm}$, an exciton is created and a rapid non-radiative relaxation of tue electron-hole pair occurs to the $E_1^{\pm}$ energies.[8] In semiconducting SWCNT, the carriers then recombine radiately causing the emission of photon of energy E_{11}. This process is called photoluminescence.

Similarly to absorption, CNTs need to be prepared for photoluminescence measurements, as in case of bundled tubes any photoexcited carriers can decay non radiatively through the surrounding tubes. Due to the large number of available states at the singularities, the photoluminescence fetures are very sharp. These, combined with the absorptions features, can be use to construct a PLE map. As each specific nanotube will absorb photons of energy E_{22} and re-emit photons of energy E_{11} depending on its the chirality, each set of (E_{11}, E_{22}) energies will uniequly corresponds to a (m, n) nanotube.

Raman scattering

Raman scattering[9] is the inelastic scattering of photons by molecules. In an inelastic Raman process the incident photon produces an excitation to a virtual energy state in

the molecule. If the material absorbs the energy by exciting a molecular or electronic vibration, the re-emitted photon will have a lower energy, and the process is called Stokes scattering. If the material loses energy, the emitted photon will have a higher energy the the incident one, and the process is called anti-Stokes scattering. The difference in energy between the incident photons and the scattered ones corresponds to the energy of the vibrational mode.

The process can happen at any energy of the incident photon, but if this matches any allowed optical transition the intensity of the signal is enhanced, and the process is called resonant Raman scattering (RSS).

RSS spectroscopy is a very powerful tool to characterise CNTs as it strongly depends on their chirality. The main features observed in the CNT are the radial breathing mode (RBM), the G-band, the D-band and the G'-band.

The RBM is a symmetric mode originated by the radial vibrations of atoms in respect of the nanotube axis, and its frequency is linked to the nanotube diameter by the formula

$$\omega_{RBM} = \frac{A}{d_t} + B \tag{2.32}$$

where d_t is the tube diameter, and A and B are parameters determined experimentally depending on the sample environment (e.g. A = 248, B = 0 for nanotubes on a SiO_2 substrate; A = 239, B = 0 for bundled nanotubes; A = 218, B = 16 for nanotubes dispersed in aqueous solution; A = 204, B = 27 for free-standing nanotubes).

The graphite-like band (G-band) is originated by the in-plane stretching of the bond between the two carbon atoms in the unit cell. Differently from graphite, where the band has a Lorentzian shape at $\omega_G \sim 1582$ cm^{-1}, in CNT it is composed of several peaks originating from the quantisation of the $\mathbf{k}_\perp$ wave vector. Typically two peaks are observed, the so called G^-, associated with the vibrations along the circumferential direction, and the G^+, associated with the longitudinal vibrations. The position of the

peaks, around $\omega_{G^-} \sim 1570$ cm^{-1} and $\omega_{G^+} \sim 1590$ cm^{-1}, changes depending on the diameter and the metallic or semiconducting character of the nanotubes.

The D-band is the disorder induced band, observed in the range $\omega_D \sim 1300 \div 1400$ cm^{-1}. It is common to all the sp^2-hybridized carbon materials, and it is active in the presence of defects, finite size effects and molecules linked to the nanotubes wall. It depends on the incident light energy E_L, following the relation $\omega_D = 1210 + 53E_L$ for nanotubes bundles, and being tube-specific for isolated SWCNT, decreasing with the tube diameter.[10,11,12,13]

The G'-band appears at $\omega_{G'} = 2\omega_D$, but while the D-band originates from a double resonance process involving a phonon and a defect, the G'-band involves two phonons. Carbon nanotubes sometimes show two G'-bands, due two resonance with two different van Hove singularities.

2.3 Electrical transport

Electrical transport properties are among the most significant properties of CNT. Due to their size, they can be considered as quantum wires, where transport properties are not ruled by classical laws any more. In a macroscopic conductor, the electrical properties solely depend on the properties of material, specifically on its resistivity ρ, which is generally size and voltage independent, and the electrical resistance of a square conductor with length L and section $W \times W$ is given by

$$R = \rho \frac{L}{W^2}. \tag{2.33}$$

and its inverse, conductance (G), is defined as:

$$G = \sigma \frac{W^2}{L}. \tag{2.34}$$

where $\sigma = \rho^{-1}$ is the conductivity.

The classical description is not valid any more when the dimensionality of the system becomes comparable with the typical characteristic lengths of electrical transport, specifically with the mean free path (L_m), defined as the average length that an electron travels before being scattered by a scattering centre (defects, impurities...) and the phase relaxation length L_φ, defined as the length over which an electron retains its coherence as a wave. Specifically, when $L \ll L_m, L_\varphi$, we observe a ballistic regime.

In this situation, the current between two contacts with potentials ϕ_1 and ϕ_2 ($\phi_1 > \phi_2$) is given by the electrons with wave vector $k > 0$ and energy $\phi_1 < E < \phi_2$. As there are several sub-bands (cfr. 2.1.2) for every k value, the current I is given by the sum of all the currents for all the $k > 0$ of all the sub-bands $E_j(k)$ with energy $\phi_1 < E_j(k) < \phi_2$. These sub-bands are called channels $M(E)$. Thus every electron in an unoccupied state with energy $\phi_1 < E < \phi_2$ brings a contribution to the current given by $I_e = \frac{e}{t_t}$, where t_t is the carrier transit time $t_t = L/v$ and $v = \hbar^{-1}(\partial E/\partial k)$ is the velocity of the electron. The total current will be

$$I = \frac{e}{L} \cdot \frac{2L}{2\pi} \sum_j \int_{k>0} \frac{1}{\hbar} \frac{\partial E_k(k)}{\partial k} [f(E_j - \phi_1) - f(E_j - \phi_2)] dk \tag{2.35}$$

where $f(E_j - \phi_i)$ is the Fermi distribution. Considering the spin degeneracy of 2 and that each k level occupies $\Delta k = 2\pi/L$, it is possible to write $M(E) = 2\int_{k>0} \frac{dk}{2\pi/L}$, so changing the integration variable and converting the sum on k to the integral, the current can be written as:

$$\begin{aligned} I &= \frac{2e}{h} \int [f(E_j - \phi_1) - f(E_j - \phi_2)] M(E) dE \\ &= \frac{2e^2}{h} M \frac{(\phi_1 - \phi_2)}{e}, \end{aligned} \tag{2.36}$$

where $M(E)$ is considered constant over $\phi_1 < E < \phi_2$.

Since the voltage between the electrodes is $V = (\phi_1 - \phi_2)/e$, the resistance is

$$R = \frac{I}{V} = \frac{h}{2e^2}\frac{1}{M} = \frac{R_0}{M} \tag{2.37}$$

where

$$R_0 = \frac{h}{2e^2} = 12.9064\text{k}\Omega \tag{2.38}$$

is the resistance quantum, whose inverse

$$G_0 = \frac{2e^2}{h} = 77.4809 \cdot 10^{-6}\text{S} \tag{2.39}$$

is the conductance quantum, and the conductivity is then

$$G = ME \tag{2.40}$$

This conduction regime only happens in case of perfect ohmic contacts between the CNT and the probes. In this scenario, the conductivity is easily calculated from band structure calculations. For example, metallic nanotubes have two quantum channels at the Fermi energy E_F (cfr. Figure 2.5), resulting in $G(E_F) = 2G_0$.[14]

This value is the maximum theoretically measurable, although in practical situations the reflection-less transmission between contacts and CNT is not achievable, limiting this value. This is taken in account introducing the transmission probability T, which is the probability for one electron to go from the contact 1 to the contact 2, redefining the conductance as

$$G = \frac{2e^2}{h}MT = \frac{2e^2}{h}\sum_{ij}^{M}|t_{ij}|^2, \tag{2.41}$$

where T is written as the sum of transmission probability from the ith to the jth channel. This equation is known as the Landauer formula.

This has experimentally observed on both metallic[15,16,17,18] and semiconducting[19] CNTs, with L_m of over 700 nm at room temperature, and 1 μm at 1.5 K.[20]

Ballistic transport has also been observed in MWCNTs, and it has been shown that the current only flows in the outermost layers.[21,22,23]

If individual CNTs offer interesting electrical properties, for applications networks of CNTs are the most practical solution. The conductivity in this case is influenced by the morphology of the network and its composition.

The tube length is an important factor for the network conductivity. With longer tubes, charges need to cross less tube junctions travelling through the network, and it has been shown that the conductivity scales with the length of nanotubes.[24]

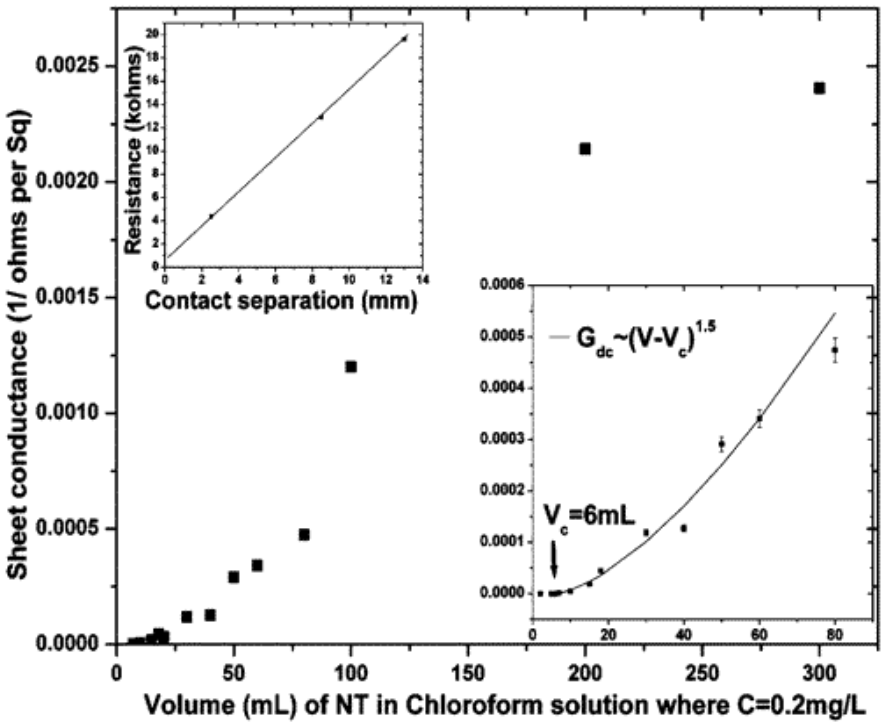

Figure 2.7: Sheet conductance of the CNT network vs volume of CNT in chloroform solution used to fabricate the film. The volume of CNT solution is directly proportional to the network density. The onset of conduction when the first percolative path across the sample is formed is obtained for V_C=6ml in the lower right inset. This inset shows the power fit in the percolation region, where the critical exponent is α=1.5. Outside of the percolation region the fit shows a linear regime. The inset in the upper left is the measured network resistance versus the contacts distance, for networks of the same density, to verify that the resistance with the contact probes is negligible for this study. Reproduced with permission from reference [25]. Copyright 2004, American Chemical Society

Another important factor is the density of tubes per unit area, as according to the standard percolation theory[26] the conductivity scales with the network density as

$$\sigma \propto (N - N_C)^{\alpha} \tag{2.42}$$

where N is the network density (conductive sticks/μm^2), N_C is the critical density above which percolation is achieved and α is a parameter which has been experimentally found to be 1.5 for a network of CNTs[25] (see Figure 2.7).

Regardless of general considerations on the morphology, in case of carbon nanotubes networks the resistivity is dominated by the junction resistances between nanotubes.[27,28,29,24]

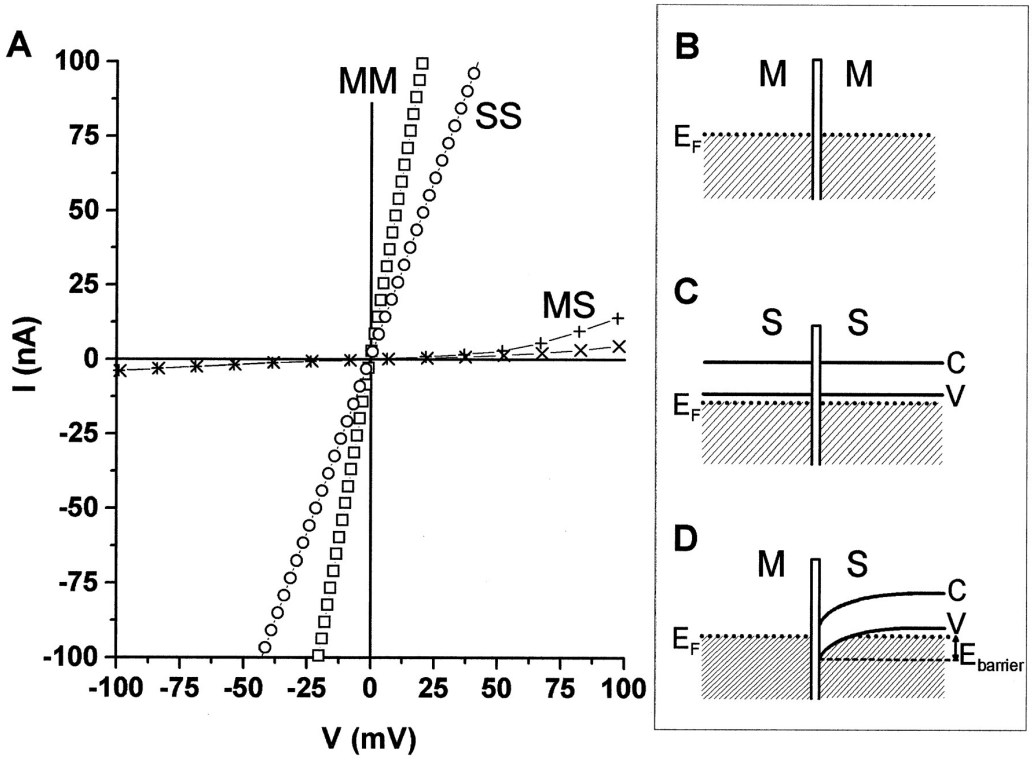

Figure 2.8: (A) I-V characteristics of several SWCNT junctions. Open squares, four-terminal measurement of an metallic-metallic (MM) junction at 200 K; open circles, two-terminal measurement of an semiconducting-semiconducting (SS) junction at 200 K; crosses and plus signs, two-terminal measurements of metallic-semiconducting (MS) junctions at 50 K and V_G= -25V. (B through D) The expected band structures near the junctions. There exists a finite density of states on either side of the junction for (B) the metallic-metallic and (C) the SS junctions. (D) In the MS junction, a Schottky barrier of height $E_{barrier}$ forms in the semiconducting SWCNT because of charge transfer from the metallic SWCNT. (The conduction and valence bands of the semiconducting SWCNTs are denoted by C and V and the Fermi level by E_F). Reproduced with permission from reference [30]. Copyright 2000, The American Association for the Advancement of Science

On this aspect, an important morphological parameter influencing the conductivity

is the size of bundles. Nirmalraj *at al.*[28] were able to show through conductive AFM (c-AFM) measurements the key role of de-bundling CNTs in order to increase conductivity of films, measuring an average junction resistance of 230 kΩ between single tubes and small diameter bundles (1.2 - 1.8 nm), 294 kΩ between medium size bundles (4.5 - 6.8 nm) and 2.7 MΩ for junctions between larger bundles (7 - 14 nm).

The type of junction also affects heavily the conductivity. Specifically, Stadermann *et al.*[30] studied the resistance of metallic-metallic, semiconducting-semiconducting and metallic-semiconducting tube junctions by fabricating junctions of two individual crossed single-walled CNT with electrical contacts at each end of each nanotube. The first two cases delivered a resistance of ∼200 kΩ and ∼2 MΩ respectively, and the latter showed a Schottky barrier junction, with a resistance over the linear response of ∼200MΩ (see Figure 2.8).

For these reasons, the composition of the network influences the conductivity of the network. This was studied in detail by Yanagi *et al.*[31]. Remarkably, they were able to observe quantum transport in pure metallic SWCNTs networks, while with the presence of semiconducting SWCNT hopping barriers appear, and no quantum transport occurred.

2.4 Carbon nanotube solubilisation

Carbon nanotubes have a limited solubility and processability in water or organic solvents due to their aspect ratio and strong Van Der Waals interactions, causing their aggregation in bundles.

An effective de-bundling and dispersion in solution of CNTs is essential for spectroscopic studies (see section 2.2) but also for their use in networks, as described in section 2.3.

Some organic solvents (such as N,N-dimethylformamide (DMF), N-methylpyrrolidinone (NMP), o-dichlorobenzene (O-DCB)) are able to disperse CNTs

to some extent, but maximum concentration achievable and the degree of isolation and stability are not sufficient for many applications.[32,33,34,35]

A common strategy to improve the solubilisation is covalent modification of the CNTs surface, with the most used consisting in the oxidation of the CNT wall to introduce carboxylic groups or other functional groups[36,37,38] to improve the dispersability and prevent aggregation. This techniques offers a very high dispersion stability, but the disruption of the graphene lattice heavily affects the intrinsic properties of CNTs, changing their conductivity and mechanical properties.

Alternately, non-covalent functionalisation offers an effective strategy to dissolve CNTs in aqueous or organic solvents relying on the interaction between a surfactant and the CNT walls.

One of the most common non-covalent solubilisation in aqueos solvents uses sodium dodecyl sulfate (SDS)[39] or sodium dodecylbenzenesulfonate (SDBS)[40] as surfactant, which are molecules consisting of an hydrophilic head-group and a hydrophobic tail-group. The technique consists in sonicating the nanotubes in a solution containing the surfactants to break the CNTs bundles and allow the surfactant tail to interact with the tubes via an hydrophobic interaction. This created a dynamic equilibrium in which SDS or SDBS create micelles around the tube preventing re-aggregation and effectively stabilising the CNTs in the aqueous solvent.

Another effective technique makes use of single-strand DNA (ssDNA) or double-strand DNA (dsDNA). In these cases the aromatic nucleic-acids have a strong interaction with the CNT walls due to the $\pi - \pi$ stacking, causing the deoxyribonucleic acid (DNA) to wrap helically around the tube leaving the phosphate backbones exposed to water, making the CNT soluble.[41,42] This has been shown to be highly sequence dependant, allowing a selection of chiralities.[43]

The use of water-soluble surfactants or DNA have the major disadvantage of not being compatible with organic solvents, making them unsuitable to many electronic processes which are not water compatible.

Among solubilisation processes compatible with organic solvents, wrapping CNTs with π-conjugated polymers has been one of the most explored routes, as a strong $\pi-\pi$ interaction is expected. The first studies made use of poly(p-pheny-lenevinylene)s (PPVs) derivatives such as PmPV[44], which showed the ability to produce stable CNTs dispersions, suggesting the ability of the polymer to wrap the CNT, with the property of preferentially solubilising nanotubes of specific diameters or a range of diameters.[45]

Similarly, π-conjugated polymers also showed the ability to selectively extract semiconducting SWCNTs. Nish *et al.*[46] demonstrated that through the use of poly(9,9-dioctyl-fluorenyl-2,7-diyl) (PFO) or poly[(9,9-dioctylfluorenyl-2,7- diyl)-alt-co-(1,4-benzo-2,1,3-thiadiazole) (F8BT) it is possible to produce solutions containing only semiconducting polymers, removing all the metallic tubes. Figure 2.9 shows the Raman and PLE spectra of PFO-wrapped SWCNTs in toluene. It is clear from the PLE map that only (7,5) tubes can be found in the emission, while the Raman shows the absence of metallic tubes, which are clearly visible in the red curve from the peak around 200 cm^{-1} when dispersed with SDBS.

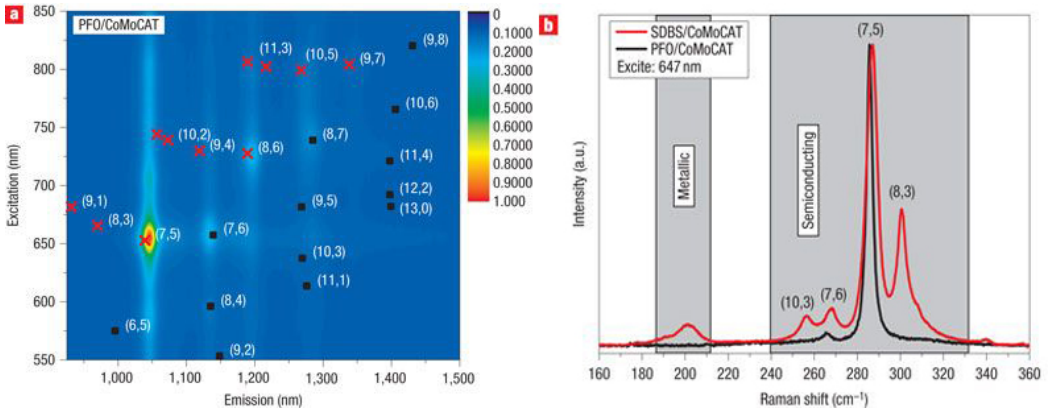

Figure 2.9: PL and Raman spectra of SWCNT solubilised with the PFO polymer. (a) The PLE map shows the strength of the PL emission as a false colour plot, with the different species labelled by their (n,m) indices. The emission is dominated by a very prominent (7,5) peak. (b) A comparison between the Raman spectra, taken using a 647 nm light source, of surfactant-wrapped SWNTs (red line) and PFO wrapped SWNTs (black line), normalized with respect to the semiconducting (7,5) nanotube. This figure also emphasizes the removal of both the metallic and other semiconducting species by the PFO/toluene solution. Adapted with permission from reference [46]. Copyright 2007, Springer Nature

poly(3-alkylthiophene)s (P3ATs), such as poly(3-hexylthiophene) (P3HT) are also widely used to solubilise CNTs, where also the sulphur atom in the backbone might contribute to the adhesion to the CNT wall.[47] Interestingly P3HT, which normally shows a rapid degradation when dissolved in organic solvents containing oxygen and exposed to UV, does not degrade when wrapped to CNTs.[48] It has been proposed that the electron transfer from the P3HT to CNT changes the redox potential of P3HT to oxygen enhancing the oxidative stability of P3HT, but also the $\pi - \pi$ interaction between the P3HT and the CNT might improve the stability of the π-conjugation offering less opportunities for the singlet oxygen to react with P3HT.

Poly(3-alkylthiophenes) generally do not show any selectivity when dissolved in chlorinated solvents, while it has been found that with less polar solvents like toluene, P3ATs are able to selectively solubilise semiconducting SWCNTs.[49]

Another strategy to solubilise CNTs relies on the CH-π interaction between polymers and CNT. Baskaran *et al.*[50] demonstrated that non-conjugated polymers rich in -CH groups such as poly-butadiene (PBD), polyisoprene (PI), polystyrene (PS), poly(methyl methacrylate) (PMMA) and poly(ethylene oxide) (PEO) are able to produce stable dispersions of MWCNT, and studying the shift of the -CH vibration in the Fourier-transform infrared spectroscopy (FTIR) spectra of the composites they attributed the binding to the interaction of the -CH groups with the π orbitals on the CNT wall.

Other non-conjugated polymer which have been reported to successfully wrap CNTs include Poly(vinyl alcohol) (PVA)[51] and poly(vinylpyrrolidone) (PVP),[52] or biopolymer such as gelatin[53] or carboxymethyl cellulose sodium salt (CMC).[54]

2.5 Summary

This chapter gave a brief introduction to carbon nanotubes, describing their structure and fundamental properties. Starting from the graphene lattice, the crystal structure of carbon nanotubes is described, and it is shown how their structure implies a

quantisation of the circumferential $\mathbf{k}_\perp$ vector. It is shown how this quantisation causes the CNTs to have a metallic or semi-conducting character, depending on whether the allowed k vectors cross the Dirac point of the graphene band structure. The density of states for CNTs is then shown, describing the characteristic *van Hove singularities*. Most importantly, the electronic properties strictly depend on the geometry.

A brief description of the optical properties of carbon nanotubes is then presented, describing the absorption and photoluminescence properties, and their characteristic Raman features. These offer powerful tools to characterise CNT, as the PL and Raman emission strictly depend on the chirality of the CNT.

The next section describes the electrical properties of carbon nanotubes, with a short introduction to quantum transport which is characteristic of CNTs. It is then shown how the transport properties change in networks of CNTs, where the resistance is dominated by the inter-tube connections.

Finally, a quick overview of the solubilisation techniques is presented, which are fundamental for the use of CNTs in many device applications. Among the most successful ones, solubilisation and individualisation of CNTs via polymer wrapping is one of the most studied, and will be the subject of studies in the experimental section of this thesis.

Bibliography

1. R. Saitō, G. Dresselhaus, and M. S. Dresselhaus, *Physical Properties of Carbon Nanotubes*. London, UK: Imperial College Press, 1998.

2. A. Jorio, G. Dresselhaus, and M. S. Dresselhaus, *Carbon nanotubes : advanced topics in the synthesis, structure, properties and applications*, vol. 111 of *Topics in Applied Physics*. Berlin, Heidelberg: Springer Berlin Heidelberg, 2008.

3. P. R. Wallace, "The band theory of graphite," *Physical Review*, vol. 71, no. 9, pp. 622–634, 1947.

4. S. Reich, J. Maultzsch, C. Thomsen, and P. Ordejón, "Tight-binding description of graphene," *Physical Review B*, vol. 66, no. 3, p. 035412, 2002.

5. J. W. Mintmire and C. T. White, "Universal Density of States for Carbon Nanotubes," *Physical Review Letters*, vol. 81, no. 12, pp. 2506–2509, 1998.

6. H. Ajiki and T. Ando, "Carbon Nanotubes: Optical Absorption in Aharonov-Bohm Flux," *Japanese Journal of Applied Physics*, vol. 34, no. S1, p. 107, 1995.

7. A. Hagen and T. Hertel, "Quantitative Analysis of Optical Spectra from Individual Single-Wall Carbon Nanotubes," *Nano Letters*, vol. 3, no. 3, pp. 383–388, 2003.

8. J. S. Lauret, C. Voisin, G. Cassabois, C. Delalande, P. Roussignol, O. Jost, and L. Capes, "Ultrafast Carrier Dynamics in Single-Wall Carbon Nanotubes," *Physical Review Letters*, vol. 90, no. 5, p. 4, 2003.

9. C. Raman, "A New Radiation," 1928.

10. M. a. Pimenta, E. B. Hanlon, A. Marucci, P. Corio, S. D. M. Brown, S. a. Empedocles, M. G. Bawendi, G. Dresselhaus, and M. S. Dresselhaus, "The anomalous dispersion of the disorder-induced and the second-order Raman Bands in Carbon Nanotubes," *Brazilian Journal of Physics*, vol. 30, no. 2, pp. 423–427, 2000.

11. A. G. Souza Filho, A. Jorio, G. Dresselhaus, M. S. Dresselhaus, R. Saitō, A. K. Swan, M. S. Ünlü, B. B. Goldberg, J. H. Hafner, C. M. Lieber, and M. A. Pimenta, "Effect of quantized electronic states on the dispersive Raman features in individual single-wall carbon nanotubes," *Physical Review B*, vol. 65, no. 3, p. 035404, 2001.

12. S. D. M. Brown, A. Jorio, M. S. Dresselhaus, and G. Dresselhaus, "Observations of the D -band feature in the Raman spectra of carbon nanotubes," *Physical Review B*, vol. 64, no. 7, p. 073403, 2001.

13. M. A. Pimenta, A. Jorio, S. D. M. Brown, A. G. Souza Filho, G. Dresselhaus, J. H. Hafner, C. M. Lieber, R. Saitō, and M. S. Dresselhaus, "Diameter dependence of the Raman D-band in isolated single-wall carbon nanotubes," *Physical Review B*, vol. 64, no. 4, p. 041401, 2001.

14. C. T. White and T. N. Todorov, "Carbon nanotubes as long ballistic conductors," *Nature*, vol. 393, no. 6682, pp. 240–241, 1998.

15. S. J. Tans, M. H. Devoret, H. Dai, A. Thess, R. E. Smalley, L. J. Geerligs, and C. Dekker, "Individual single-wall carbon nanotubes as quantum wires," *Nature*, vol. 386, no. 6624, pp. 474–477, 1997.

16. P. L. McEuen, M. Bockrath, D. H. Cobden, Y.-G. Yoon, and S. G. Louie, "Disorder, Pseudospins, and Backscattering in Carbon Nanotubes," *Physical Review Letters*, vol. 83, no. 24, pp. 5098–5101, 1999.

17. W. Liang, M. Bockrath, D. Bozovic, J. H. Hafner, M. Tinkham, and H. Park, "Fabry - Perot interference in a nanotube electron waveguide," *Nature*, vol. 411, no. 6838, pp. 665–669, 2001.

18. J. Kong, E. Yenilmez, T. W. Tombler, W. Kim, H. Dai, R. B. Laughlin, L. Liu, C. S. Jayanthi, and S. Y. Wu, "Quantum Interference and Ballistic Transmission in Nanotube Electron Waveguides," *Physical Review Letters*, vol. 87, no. 10, p. 106801, 2001.

19. A. Javey, J. Guo, Q. Wang, M. Lundstrom, and H. Dai, "Ballistic carbon nanotube field-effect transistors," *Nature*, vol. 424, no. 6949, pp. 654–657, 2003.

20. M. S. Fuhrer, "Ballistic transport in semiconducting carbon nanotubes," in *AIP Conference Proceedings*, vol. 591, pp. 401–404, AIP, 2001.

21. A. Bachtold, C. Strunk, J.-P. Salvetat, J.-M. Bonard, L. Forró, T. Nussbaumer, and C. Schönenberger, "Aharonov–Bohm oscillations in carbon nanotubes," *Nature*, vol. 397, no. 6721, pp. 673–675, 1999.

22. S. Frank, P. Poncharal, Z. L. Wang, and W. A. de Heer, "Carbon nanotube quantum resistors," *Science (Washington, D. C.)*, vol. 280, no. 5370, pp. 1744–1746, 1998.

23. C. Schönenberger, A. Bachtold, C. Strunk, J.-P. Salvetat, and L. Forró, "Interference and Interaction in multi-wall carbon nanotubes," *Applied Physics A: Materials Science & Processing*, vol. 69, no. 3, pp. 283–295, 1999.

24. D. Hecht, L. Hu, and G. Grüner, "Conductivity scaling with bundle length and diameter in single walled carbon nanotube networks," *Applied Physics Letters*, vol. 89, no. 13, pp. 1–3, 2006.

25. L. Hu, D. S. Hecht, and G. Grüner, "Percolation in Transparent and Conducting Carbon Nanotube Networks," *Nano Letters*, vol. 4, no. 12, pp. 2513–2517, 2004.

26. S. Kirkpatrick, "Percolation and Conduction," *Reviews of Modern Physics*, vol. 45, no. 4, pp. 574–588, 1973.

27. M. Stadermann, S. J. Papadakis, M. R. Falvo, J. Novak, E. Snow, Q. Fu, J. Liu, Y. Fridman, J. J. Boland, R. Superfine, and S. Washburn, "Nanoscale study of conduction through carbon nanotube networks," *Physical Review B*, vol. 69, no. 20, p. 201402, 2004.

28. P. N. Nirmalraj, P. E. Lyons, S. De, J. N. Coleman, and J. J. Boland, "Electrical connectivity in single-walled carbon nanotube networks.," *Nano letters*, vol. 9, no. 11, pp. 3890–5, 2009.

29. K. Yanagi, H. Udoguchi, S. Sagitani, Y. Oshima, T. Takenobu, H. Kataura, T. Ishida, K. Matsuda, and Y. Maniwa, "Transport mechanisms in metallic and semiconducting single-wall carbon nanotube networks," *ACS Nano*, vol. 4, no. 7, pp. 4027–4032, 2010.

30. M. S. Fuhrer, J. Nygård, L. Shih, M. Forero, Y.-G. Yoon, M. S. C. Mazzoni, H. J. Choi, J. Ihm, S. G. Louie, A. Zettl, and P. L. McEuen, "Crossed nanotube junctions," *Science*, vol. 288, no. 5465, pp. 494–497, 2000.

31. K. Yanagi, H. Udoguchi, S. Sagitani, Y. Oshima, T. Takenobu, H. Kataura, T. Ishida, K. Matsuda, Y. Maniwa, and S. Figure, "Transport mechanisms in metallic and semiconducting single-wall carbon nanotube networks," *ACS Nano*, vol. 4, no. 7, pp. 4027–4032, 2003.

32. S. Giordani, S. Bergin, V. Nicolosi, S. Lebedkin, W. J. Blau, and J. N. Coleman, "Fabrication of stable dispersions containing up to 70% individual carbon nanotubes in a common organic solvent," *physica status solidi (b)*, vol. 243, no. 13, pp. 3058–3062, 2006.

33. D. S. Kim, D. Nepal, and K. E. Geckeler, "Individualization of Single-Walled Carbon Nanotubes: Is the Solvent Important?," *Small*, vol. 1, no. 11, pp. 1117–1124, 2005.

34. B. J. Landi, H. J. Ruf, J. J. Worman, and R. P. Raffaelle, "Effects of Alkyl Amide Solvents on the Dispersion of Single-Wall Carbon Nanotubes," *The Journal of Physical Chemistry B*, vol. 108, no. 44, pp. 17089–17095, 2004.

35. C. A. Furtado, U. J. Kim, H. R. Gutierrez, L. Pan, E. C. Dickey, and P. C. Eklund, "Debundling and Dissolution of Single-Walled Carbon Nanotubes in Amide Solvents," *Journal of the American Chemical Society*, vol. 126, no. 19, pp. 6095–6105, 2004.

36. M. Shaffer, X. Fan, and A. Windle, "Dispersion and packing of carbon nanotubes," *Carbon*, vol. 36, no. 11, pp. 1603–1612, 1998.

37. N. I. Kovtyukhova, T. E. Mallouk, L. Pan, and E. C. Dickey, "Individual Single-Walled Nanotubes and Hydrogels Made by Oxidative Exfoliation of Carbon Nanotube Ropes," *Journal of the American Chemical Society*, vol. 125, no. 32, pp. 9761–9769, 2003.

38. S. W. Kim, T. Kim, Y. S. Kim, H. S. Choi, H. J. Lim, S. J. Yang, and C. R. Park, "Surface modifications for the effective dispersion of carbon nanotubes in solvents and polymers," *Carbon*, vol. 50, no. 1, pp. 3–33, 2012.

39. M. J. O'Connell, S. M. Bachilo, C. Huffman, V. C. Moore, M. S. Strano, E. H. Haroz, K. L. Rialon, P. Boul, W. H. Noon, C. Kittrell, J. Ma, R. H. Hauge, R. B. Weisman, and R. E. Smalley, "Band Gap Fluorescence from Individual

Single-Walled Carbon Nanotubes," *Science*, vol. 297, no. 5581, pp. 593–596, 2002.

40. M. F. Islam, E. Rojas, D. M. Bergey, A. T. Johnson, and A. G. Yodh, "High Weight Fraction Surfactant Solubilization of Single-Wall Carbon Nanotubes in Water," *Nano Letters*, vol. 3, no. 2, pp. 269–273, 2003.

41. M. Zheng, A. Jagota, E. D. Semke, B. A. Diner, R. S. McLean, S. R. Lustig, R. E. Richardson, and N. G. Tassi, "DNA-assisted dispersion and separation of carbon nanotubes," *Nature Materials*, vol. 2, no. 5, pp. 338–342, 2003.

42. N. Nakashima, S. Okuzono, H. Murakami, T. Nakai, and K. Yoshikawa, "DNA Dissolves Single-walled Carbon Nanotubes in Water," *Chemistry Letters*, vol. 32, no. 5, pp. 456–457, 2003.

43. X. Tu, S. Manohar, A. Jagota, and M. Zheng, "DNA sequence motifs for structure-specific recognition and separation of carbon nanotubes," *Nature*, vol. 460, no. 7252, pp. 250–253, 2009.

44. S. A. Curran, P. M. Ajayan, W. J. Blau, D. L. Carroll, J. N. Coleman, A. B. Dalton, A. P. Davey, A. Drury, B. McCarthy, S. Maier, and A. Strevens, "A Composite from Poly(m-phenylenevinylene-co-2,5-dioctoxy-p-phenylenevinylene) and Carbon Nanotubes: A Novel Material for Molecular Optoelectronics," *Advanced Materials*, vol. 10, no. 14, pp. 1091–1093, 1998.

45. A. B. Dalton, C. Stephan, J. N. Coleman, B. McCarthy, P. M. Ajayan, S. Lefrant, P. Bernier, W. J. Blau, and H. J. Byrne, "Selective Interaction of a Semiconjugated Organic Polymer with Single-Wall Nanotubes," *The Journal of Physical Chemistry B*, vol. 104, no. 43, pp. 10012–10016, 2000.

46. A. Nish, J.-Y. Hwang, J. Doig, and R. J. Nicholas, "Highly selective dispersion of single-walled carbon nanotubes using aromatic polymers," *Nature Nanotechnology*, vol. 2, no. 10, pp. 640–646, 2007.

47. E. Zaminpayma and K. Mirabbaszadeh, "Investigation of molecular interaction between single-walled carbon nanotubes and conjugated polymers," *Polymer Composites*, vol. 33, no. 4, pp. 548–554, 2012.

48. P. J. Goutam, D. K. Singh, P. K. Giri, and P. K. Iyer, "Enhancing the Photostability of Poly(3-hexylthiophene) by Preparing Composites with Multiwalled Carbon Nanotubes," *The Journal of Physical Chemistry B*, vol. 115, no. 5, pp. 919–924, 2011.

49. H. W. Lee, Y. Yoon, S. Park, J. H. Oh, S. Hong, L. S. Liyanage, H. Wang, S. Morishita, N. Patil, Y. J. Park, J. J. Park, A. Spakowitz, G. Galli, F. Gygi, P. H. Wong, J. B. Tok, J. M. Kim, and Z. Bao, "Selective dispersion of high purity semiconducting single-walled carbon nanotubes with regioregular poly(3-alkylthiophene)s," *Nature Communications*, vol. 2, no. 1, p. 541, 2011.

50. D. Baskaran, J. W. Mays, and M. S. Bratcher, "Noncovalent and nonspecific molecular interactions of polymers with multiwalled carbon nanotubes," *Chemistry of Materials*, vol. 17, no. 13, pp. 3389–3397, 2005.

51. X. Zhang, T. Liu, T. V. Sreekumar, S. Kumar, V. C. Moore, R. H. Hauge, and R. E. Smalley, "Poly(vinyl alcohol)/swnt composite film," *Nano Letters*, vol. 3, no. 9, pp. 1285–1288, 2003.

52. M. J. O'Connell, P. Boul, L. M. Ericson, C. Huffman, Y. Wang, E. Haroz, C. Kuper, J. Tour, K. D. Ausman, and R. E. Smalley, "Reversible water-solubilization of single-walled carbon nanotubes by polymer wrapping," *Chemical Physics Letters*, vol. 342, no. 3-4, pp. 265–271, 2001.

53. T. Takahashi, K. Tsunoda, H. Yajima, and T. Ishii, "Isolation of single-wall carbon nanotube bundles through gelatin wrapping and unwrapping processes," *Chemistry Letters*, vol. 31, no. 7, pp. 690–691, 2002.

54. N. Minami, Y. Kim, K. Miyashita, S. Kazaoui, and B. Nalini, "Cellulose derivatives as excellent dispersants for single-wall carbon nanotubes as demonstrated by absorption and photoluminescence spectroscopy," *Applied Physics Letters*, vol. 88, no. 9, p. 093123, 2006.

CHAPTER 3

Solar Cells

This chapter gives a short overview of the basic principles of photovoltaic devices. The first section introduces the most important properties of semiconductors, the charge generation, recombination and transport processes, and it is largely based on Peter Würfel, *Physics of Solar Cells: From Basic Principles to Advanced Concepts*, 2nd ed, 2009, Wiley;[1] and Jenny Nelson, *The Physics of Solar Cells*, 2003, Imperial College Press.[2] The following section will then illustrate the most predominant solar cells technologies, with a focus on perovskite solar cells, and specifically the use of carbon nanotubes in this kind of devices.

3.1 Solar cells

A solar cell is a device that converts light directly into electric energy. Energy is absorbed by a semiconductor and excites electrons to a higher energy state. These electrons need to live in their excited states for long enough to extract them into an external circuit. This can happen in semiconducting materials, where the ground and

the excited states are separated by a gap of forbidden energies. The extraction of electrons is then achieved by building an asymmetric device, such that the extraction of carriers is facilitated.

The following sections describe the concepts here briefly summarised in greater detail, with the aim of providing a general understanding of the operating principles of a solar cell.

3.1.1 Classic semiconductors: Bands and Fermi level

Classic semiconductors have continuous ranges of allowed energies known as bands. This is caused by the Pauli exclusion principle, which allows only one electron per state, so bringing atoms together causes the energy levels to split, forming a continuous set of allowed states. The bands fully occupied by electrons at absolute zero temperature are called valence bands, while the bands with vacant states at absolute zero are known as conduction bands. The gap between the lowest unoccupied band and the highest occupied band is called energy bandgap (E_G). This gap is typically in the range 1 - 4 eV in semiconductors.

Above 0 K, electrons occupy available states in the conduction band following the Fermi-Dirac distribution:

$$f_e(E) = \frac{1}{\exp\left(\frac{E-E_F}{kT}\right)+1} \tag{3.1}$$

where E_e is the energy of the electron, k is the Boltzmann costant, T is the absolute temperature and E_F is the energy of the Fermi level. It can be seen that for $E_e \ll E_F$, the probability of a state to be occupied is $f_e \approx 1$, for $E_e \gg E_F$, $f_e \approx 0$, while $f_e(E_F) = \frac{1}{2}$.

The density of free electrons in the conduction is given by

$$n = \int_{E_C}^{\infty} D(E) f_e(E) dE = N_C \exp\left(-\frac{E_C - E_F}{k_B T}\right) \tag{3.2}$$

where $D(E) \propto (E_e - E_C)^{1/2}$ is the density of states and

$$N_C = 2\left(\frac{2\pi m_e^* kT}{h^2}\right)^{3/2} \tag{3.3}$$

is the effective density of states of the conduction band, with m_e^* being the effective mass of electrons in the conduction band.

Similarly, the few unoccupied states in the valence band, known as *holes*, have a density given by

$$p = \int_{E_V}^{\infty} D(E)[1 - f_e(E)]dE = N_V \exp\left(-\frac{E_F - E_V}{k_B T}\right), \tag{3.4}$$

$$N_V = 2\left(\frac{2\pi m_h^* kT}{h^2}\right)^{3/2} \tag{3.5}$$

As in a pure, intrinsic semiconductor the holes are generated by vacancies left by electrons in the conduction band, the densities are equal $n = p = n_i$. It is worth noting that

$$np = N_C N_V \exp\left(-\frac{E_G}{k_B T}\right) = n_i^2 \tag{3.6}$$

so the product of electron and hole densities does not depend on the position of the Fermi level.

The Fermi level can be moved by doping. Doping of classic semiconductors can be obtained for example by introducing impurity atoms having a different number of valence electrons compared to the semiconductor material to be doped. The impurity can be a donor, having more valence electrons than necessary for chemical bonding with the host material, or acceptor, having fewer electrons.

The introduction of a donor effectively increases the free electrons concentration in the material conduction band. The Fermi distribution then shifts upwards to take in account of the increased concentration, and this translates into having the Fermi

level closer to the conduction band compared to the intrinsic case. Similarly, the hole concentrations p in the valence band increases when acceptors are introduced, and the Fermi level shifts towards the valence band.

Semiconductors doped with electron donors are referred to as n-type, while they are called p-type when doped with electron acceptors.

3.1.2 Electron-hole generation

An electron-hole pair is generated by any process able to supply at least the energy E_G. In solar cells, the most important among these processes is light absorption. The probability of a photon to be absorbed is given by the absorption coefficient $\alpha(\omega\hbar)$, and the number of photons absorbed can be written as

$$j_{\gamma,abs} = \alpha j_{\gamma,in}, \tag{3.7}$$

where $j_{\gamma,in}$ is the incident photon current density. Each absorbed photon generate an electron-hole pair at a rate

$$G_e = G_h = \alpha j_{\gamma,abs}. \tag{3.8}$$

The energy distribution of generated electrons and holes initially reflects the spectrum of the absorbed photons, but they quickly thermalise within the band. This happens very rapidly ($\approx 10^{-14}$ s), after which the carriers exist for a short lifetime ($\approx 10^{-12}$ s). This is however long compared to their lifetime before they thermalise to the ground state and recombine ($\approx 10^{-6}$ s). Since under illumination the electron and hole densities are greater than in the dark, the population described by the Fermi-Dirac of Eq. 3.1 is no longer valid, as the distribution of electrons is closer to the conduction band, and the one for holes is closer to the valence band. It is then necessary to describe the populations with two different Fermi-Dirac distributions:

$$n = N_C \exp\left(-\frac{E_C - E_{F,C}}{kT}\right) \tag{3.9}$$

$$p = N_V \exp\left(-\frac{E_{F,V} - E_V}{kT}\right) \tag{3.10}$$

where $E_{F,C}$ is called quasi-Fermi level for electrons and $E_{F,V}$ is the quasi-Fermi level for holes. The product is no longer n_i^2 but is now increased by

$$np = n_i^2 \exp\frac{E_{F,C} - E_{F,V}}{kT} = n_i^2 \exp\frac{\Delta E_F}{kT}, \tag{3.11}$$

where ΔE_F is the splitting of the quasi-Fermi levels.

3.1.3 Recombination

Radiative recombination

The reverse process of generation is the recombination, consisting in the annihilation of electrons and holes. The main recombination process is radiative recombination, in which the thermalised e-h pair recombines re-emitting its energy by luminescence, and it is an unavoidable process. This has to be equal to the generation rate, and it is equal to

$$R_0 = \beta n_0 p_0 = \beta n_i^2 = G_0 \tag{3.12}$$

where the index 0 has been added to denote the situation of the semiconductor in equilibrium in the dark, and β is the bimolecular recombination coefficient.

When the semiconductor is illuminated, the carrier density is given by Eq. 3.11, so we have

$$R = \beta np = \frac{G_0}{n_0 p_0} = \frac{G_0}{n_i^2} = G_0 \exp\left(\frac{\Delta E_F}{kT}\right) \tag{3.13}$$

Non-radiative recombination

Additionally to radiative recombination, other recombination processes can have a significant contribution in semiconductors. These are primarily bimolecular recombination, Auger recombination, Shockley-Read-Hall (SRH) recombination and surface recombination, all depicted in Figure 3.1.

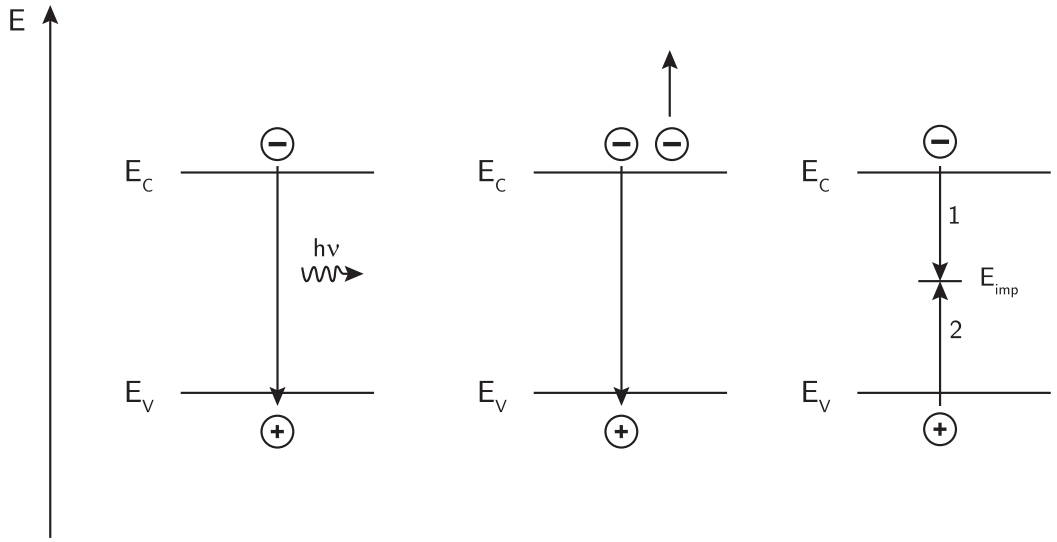

Figure 3.1: Recombinations mechanisms in semiconductors. The diagram on the left represents radiative recombination, where the energy from the recombination is emitted with a photon. This process can also happen non-radiatively. In the middle a diagram representing Auger recombination, where the energy of an excited electron is transferred to another electron, which gets excited and thermalises. On the right, trap-assisted recombination, where a carrier gets trapped into a state generated by an impurity, and subsequentially recombine with a hole.

Bimolecular recombination is a process analogous to radiative recombination, but the energy lost is transferred non-radiatively to the material.

Auger recombination occurs when the energy of a recombining electron is first transferred to another free electron, and is then lost to the lattice through collisions. It is then a three particle recombination, and its rate is given by

$$R_{Aug} = C_e n^2 p + C_h n p^2 = np(C_e n + C_h p), \tag{3.14}$$

where C_e and C_h are the Auger recombination rates for electrons and holes.

SRH happens via defects or impurities in the semiconductor, which can offer available energy states for electrons and holes in the bandgap. Recombination occurs when a free electron occupies one of these states and becomes immobile, and subsequentially recombination with a hole occurs.

The rate at which this occurs is

$$R_{SRH} = \frac{np - n_i^2}{\frac{n+N_C \exp(-(E_C-E_{imp})/kT)}{N_{imp}\sigma_p v_p} + \frac{p+N_V \exp(-(E_{imp}-E_V)/kT)}{N_{imp}\sigma_n v_n}} \tag{3.15}$$

where N_{imp} is the trap density, $\sigma_{n,p}$ is the cross-section of the trap with the electron or hole, and $v_{n,p}$ is the thermal velocity of the electron or hole.

Surface recombination happens due to the high density of states in the forbidden gap on the surface of the semiconductor, due to the absence of neighbouring atoms or to the absorption of impurities. The rate is given by

$$R_{sf} = s_n(n - n_0), \tag{3.16}$$

where the recombination velocity s_n is given by $s_n = N_{sf}\sigma_n v_n$, and N_{sf} is the two-dimensional density of traps.

3.1.4 Transport

The previous sections described the generation and recombination processes in terms of probabilistic events. In order to build a solar cell, excited carriers need to be extracted, so it is necessary to analyse their movement, starting with the driving forces causing it.

In semiconductors, the most relevant potentials are the chemical and electric potential. It can be shown that the electrochemical potential η is identical to the Fermi level, and it can be written for holes and electrons as

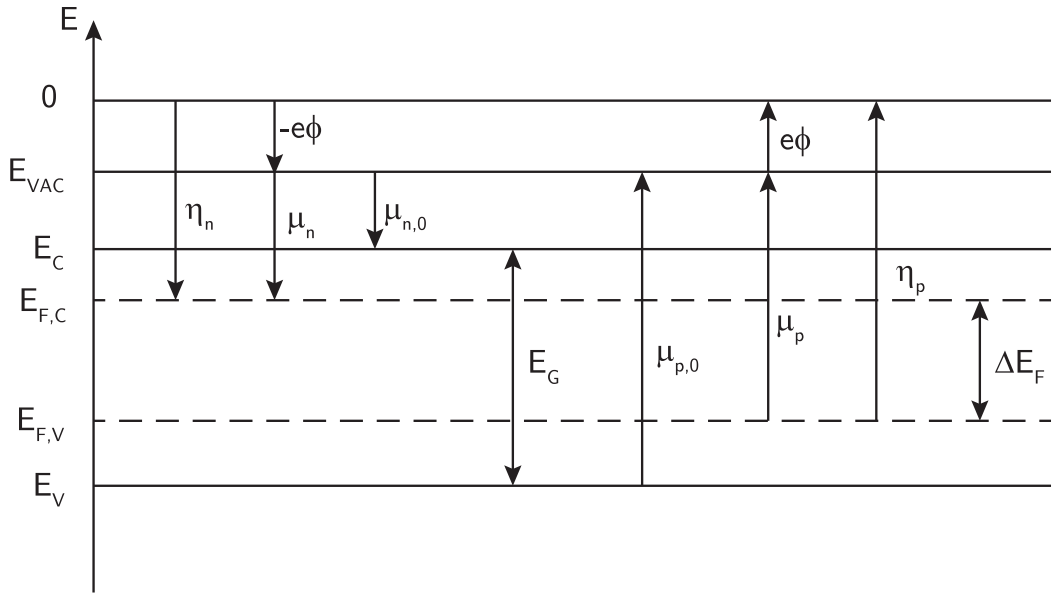

Figure 3.2: Energy diagrams for electrons and holes in a semiconductor. The diagram represents the electric potential ϕ, the chemical potentials μ and the electrochemical potential η. It is worth noting that the chemical potential in the dark is equal to the bottom of the conduction band, while under illumination it is equal to the quasi-Fermi level for electrons $E_{F,C}$. μ_e and μ_h depend on the charge density. Adapted with permission from reference [1]. Copyright 2009. John Wiley and Sons.

$$\eta_n(x) = -e\phi(x) + \mu_n(x) = E_{F,n}(x) \tag{3.17}$$

$$\eta_p(x) = e\phi(x) + \mu_p(x) = E_{F,p}(x) \tag{3.18}$$

At equilibrium, $E_F(x)$ is constant across the whole semiconductor. A gradient in $E_F(x)$ causes carriers to flow towards the lowest energy until equilibrium is reached and $E_F(x)$ is constant again.

A change in the electric or chemical potential along the semiconductor will cause a gradient in the Fermi levels, thus a current. This is represented in Figure 3.3.

If the electric potential is not constant, i.e. an electric field $E = -\nabla\phi$ is applied, a drift current will occur according to Ohm's law

$$j_{drift} = \sigma E = -\sigma\nabla\phi = e(nb_nE + pb_pE), \tag{3.19}$$

where $\sigma = e(nb_nE + pb_pE)$ is the conductivity of the semiconductor and $b_{n,p}$ are the electron and hole mobility (mobility is commonly denoted with the Greek letter μ, but the letter b is being used to avoid confusion with the chemical potential).

If the concentration of carriers is not constant across the semiconductor, according to Fick's law a diffusion current will occur

$$j_{diff} = enD\nabla n - epD\nabla p, \tag{3.20}$$

where D is the diffusion constant. By using

$$n\frac{\nabla n}{n} = n\nabla(\ln n/N_i - \ln N_C/Ni) = n\nabla(n/N_C) = n\frac{\nabla\mu}{kT}$$

and the Einstein relation for D:

$$D/b = kT/e$$

the current can be written in terms of the chemical potential:

$$j_{diff} = nb_n\nabla\mu_n - pb_n\nabla\mu_p \tag{3.21}$$

The total current is then the sum of the two:

$$j_n = -nb_ne\nabla\phi + nb_n\nabla\mu_n = nb_n\nabla E_{F,n} \tag{3.22}$$

$$j_p = -pb_be\nabla\phi - pb_p\nabla\mu_p = pb_p\nabla E_{F,p} \tag{3.23}$$

3.1.5 Solar cells characterization

The previous section described the photogeneration mechanism. If photogenerated carriers travel to the edges of the semiconductor, it is possible to extract electron and

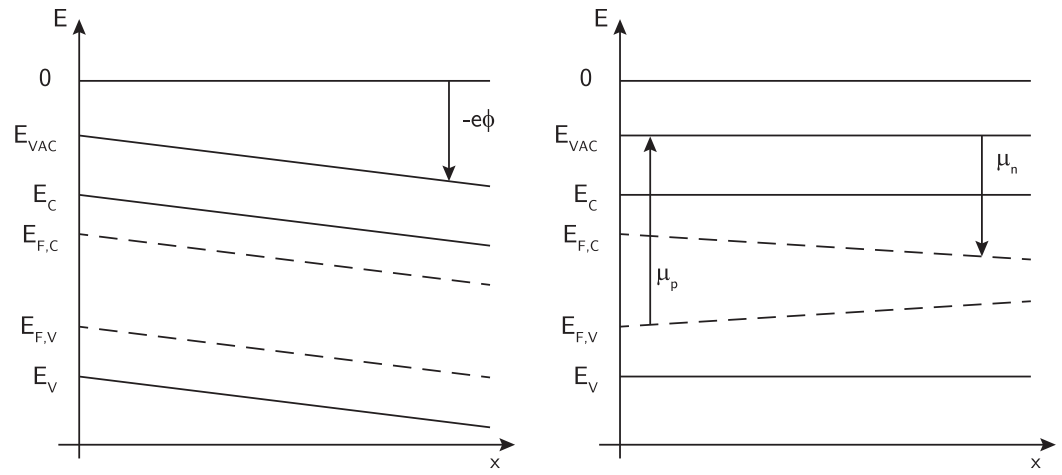

Figure 3.3: Spacial energy diagrams for a semiconductor with electric (left) and concentration (right) gradients. The presence of gradients causes a shift of the Fermi levels, causing a current in the semiconductor. Adapted with permission from reference [1]. Copyright 2009. John Wiley and Sons.

holes using selective contacts, *i.e.* contacts permeable to electrons only on one side, and holes only on the other, at different energies.

Solar cells are characterized by measuring their output current and voltage when connected to a load. When the load is zero (*i.e.* contacts are connected with an ideal wire with no resistance), the two terminals of the solar cells will have the same potential, so the potential difference across the device is zero. This is defined as *short-circuit* condition, and the current produced in this situation is defined as *short-circuit current (J_{SC})*.

The opposite situation is given by an infinitely big load, which is given by not having any contact between the terminals, so no current can flow. This is the *open-circuit* condition, and the voltage across the device in this situation is known as *open circuit voltage (V_{OC})*.

The photocurrent generated under illumination depends on the incident light and on the external quantum efficiency (EQE), which is the probability of a photon with energy E to be absorbed and deliver an electron to the external circuit. The current at short circuit will then be

$$J_{SC} = e \int j_{\gamma,in}(E) EQE(E) dE \tag{3.24}$$

where e is the elementary charge and $j_{\gamma,in}$ is the incoming photon flux.

Most solar cells behave like a diode in the dark, and the JV curve in the ideal case is given by the Shockley equation:

$$J_{\text{dark}} = -J_0 \left(e^{\frac{eV}{kT}} - 1 \right) \tag{3.25}$$

where $J_0 \propto \exp -E_g/kT$ is the saturation current. The sign convention is opposite to what normally used for electronic devices, such that the photogenerated current is positive for positive bias.

The JV curve of a solar cell under illumination will then be

$$J = J_{SC} - J_0 \left(e^{\frac{eV}{kT}} - 1 \right) \tag{3.26}$$

At open circuit, current cannot flow but charges generated cause the Fermi distribution to split. The photovoltage across the contacts can be calculated by putting $J = 0$ in Eq. 3.26, resulting in

$$V_{OC} = \frac{kT}{e} \ln \left(\frac{J_{SC}}{J_0} + 1 \right) \tag{3.27}$$

The solar device produces power between the 0 V and open circuit voltage. The optimum is reached when the product of current and voltage (the power) is maximum, and it defines the maximum power point (MPP). The ratio between this point, and the product of J_{SC} and V_{OC} defines the fill factor (FF)

$$FF = \frac{J_{MPP} V_{MPP}}{J_{SC} V_{OC}} \tag{3.28}$$

and is a measure of the *"squareness"* of the J-V curve, giving a measure of the ratio compared to an ideal current generator with no losses operating between J_{SC} and V_{OC}.

The power conversion efficiency (PCE) is then defined as the ratio of the power output and the incident light power density P_S

$$PCE = \frac{J_{MPP}V_{MPP}}{P_S} \tag{3.29}$$

.

The ideal behaviour of Eq. 3.26 is rarely seen in real applications. Non-idealities are taken into account by adding a factor m in the Shockley equation, which takes into account the weaker dependence on the voltage often seen in real devices:

$$J = J_{SC} - J_0 \left(e^{\frac{eV}{mkT}} - 1 \right) \tag{3.30}$$

where m, caled the *ideality factor*, normally varies between 1 and 2.

Additionally, real devices have parasitic resistances dissipating power. This can be modelled by two resistances in series (R_{s}) and in parallel (R_{sh}) as shown in the equivalent circuit of Figure 3.4. The series resistance takes into account of the electrical resistance of the material to the flow of charges, and it should ideally be equal to zero, while the parallel or shunt resistance is the result of leakage currents through the cells, and it should ideally be infinite. The Shockley equation can be modified to include these:

$$J = J_{SC} - J_0 \left(e^{\frac{e(V+JAR_S)}{mkT}} - 1 \right) - \frac{V + JAR_S}{R_{sh}} \tag{3.31}$$

where A is the area of the device.

Additional non-ideality factors exists and can be modelled depending on the relevance of their effect, e.g. voltage dependence of the photogenerated current or two diodes model due to additional recombination happening at the p-n junction.

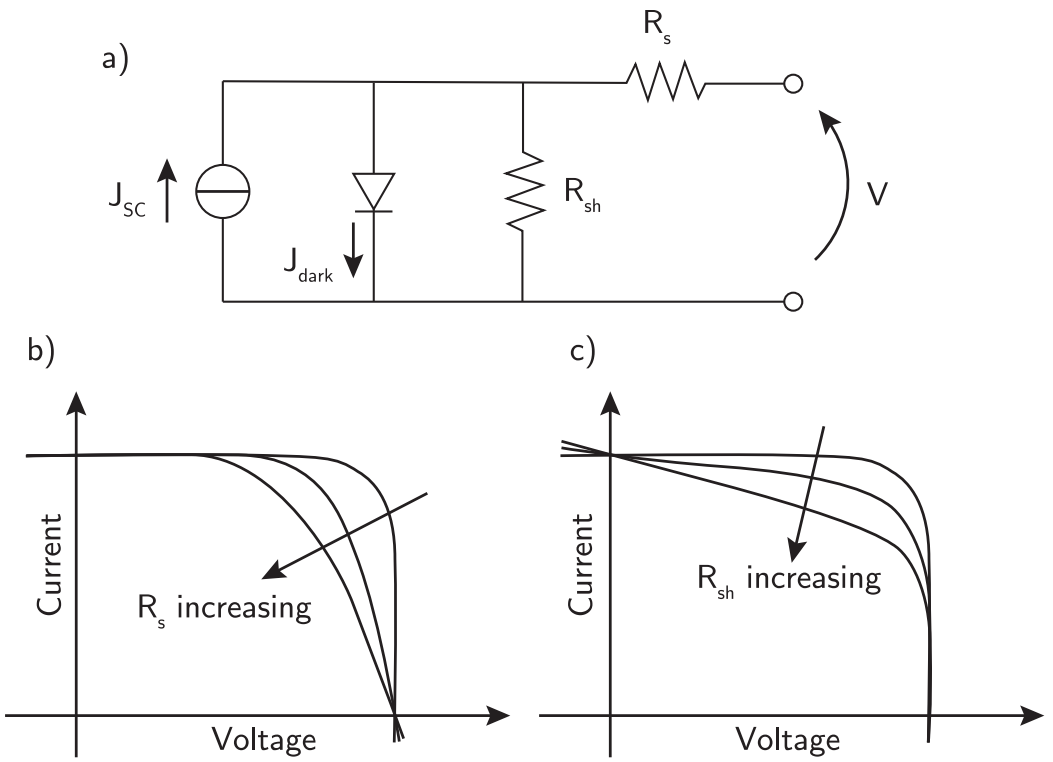

Figure 3.4: Equivalent circuit of a solar cell (a) and effects of series (b) and shunt resistance (c). An increasing shunt resistance modifies the behaviour of the cell at the open circuit voltage, while the shunt resistance changes the slope at the short-circuit point. In both cases the fill factor is reduced by parasitic resistances.

3.2 Structure of solar cells

This section will introduce the most common architectures of solar cells. The shared principle behind them is to create an asymmetry to separate holes and electrons after generation. The most common architecture is the p-n junction, normally realised with silicon, where doping is used to change the energetics in different regions of the device. Directly derived from the microelectronics industry, it is the most extensively studied for historical reasons and the common type of solar cell available commercially, covering more than 90% of the market.

Alternative concepts are based on p-i-n or n-i-p structures (where *i* means intrinsic). They are often junctions of different materials, with the intrinsic region being responsible for absorption of light and generation of carriers. The *n* and *p* layers to select and transport electrons and holes respectively. In this section are illustrated the technology which will be used in this thesis, which are solar cells on hybrid perovskites.

3.2.1 The p-n junction

The p-n junction is the most common realisation of solar cell. It consists of a junction between a p-doped semiconductor and an n-doped semiconductor. As described in Section 3.1.1, the Fermi level in the n-doped semiconductor is closer to the conduction band, while it is closer to the valence band in a p-doped semiconductor.

As the two semiconductors are brought together, the Fermi levels in both materials align to the same value, as a gradient of the Fermi level once the equilibrium is reached would generate an un-physical constant current of carriers, and the band bending shown in Figure 3.5 is reached.

Upon contact, the different concentrations of carriers in the n and p doped regions cause a current across the p-n interface until equilibrium is reached, building up a space-charge region (called depletion region, as there are no mobile carriers), creating

a built-in field. The potential difference between the two regions is called built-in potential V_{bi} which can be approximated with

$$V_{bi} = \frac{kT}{e} \ln \frac{N_A N_D}{n_i^2}, \tag{3.32}$$

where N_A and N_D are the dopant concentrations in the p and n region respectively. The depletion region depends on the doping levels, and is given by

$$w = \sqrt{\frac{2\epsilon_0 \epsilon_r}{e} \frac{N_A + N_D}{N_A N_D} V_{bi}}. \tag{3.33}$$

When a bias voltage is applied at the opposite side of the device, the p-n junction shows a rectifying behaviour. The reverse bias, i.e. positive voltage at the n-side and negative at the p-side, causes carriers in the neutral zone to flow towards the electrode, expanding the depletion region. This translates to an increase of the potential barrier at the junction, allowing only a small current to flow through the device, which is related to J_0. Under forward bias, carriers are flooded into the depletion region, causing the barrier to decrease and allowing a significant current to flow above a certain voltage, as shown in the diagrams of Figure 3.5.

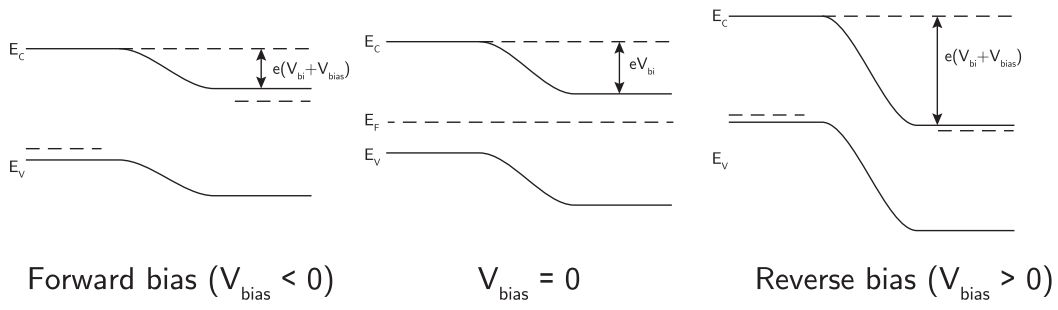

Figure 3.5: p-n junction in forward bias, unbiased, and reverse bias. The Fermi level in a un-biased p-n junction is constant across the device, and the different levels of the conduction and valence band generate a bending of the bands and a built-in voltage. When a forward bias is applied, the energy barrier between the n and p region is reduced, and more electrons can diffuse from the n to the p region, allowing a significant current to flow. In reverse bias, the potential barrier is higher, so fewer electrons can diffuse and the current is small.

When the junction is under illumination, photogenerated electrons (holes) coming from the p (n) region will move as minority carriers towards the depletion region. If

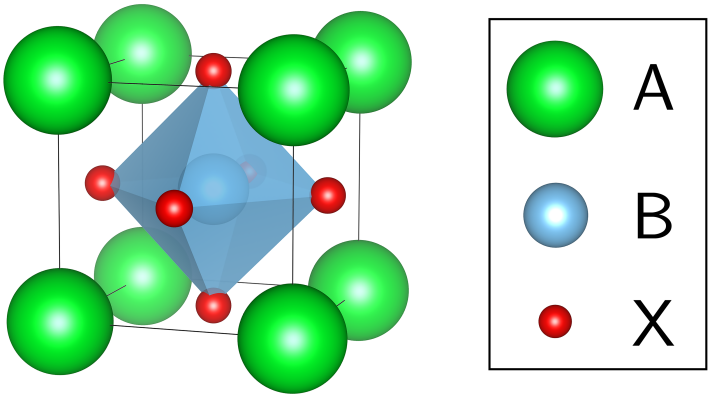

Figure 3.6: ABX3 unit cell characteristic of the perovskite crystal structure. The A site is normally occupied by cation such as Cs^+, methylammonium (MA, $CH_3NH_3^+$) and formamidinium (FA, $CH(NH_2)_2^+$). The metal cation at The B site is occupied by metal cations such as Pb or Sn. Halide anions occupied the site X.

free electrons (holes) in the p (n) region are generated within a recombination length from the junction, they can reach the depletion region and drift towards the n(p)-side where they will be majority carriers.

In the short-circuit condition, the extra photo-generated carriers exit the device, and there is no charge accumulation. Under open-circuit condition, photo-generated carriers can't exit the device and cause an accumulation of electrons in the n-type side of the p-n junction and an accumulation of holes in the p-type side of the p-n junction, creating a voltage opposite to the built-in voltage, therefore reducing the net field and increasing the diffusion current.

The equations governing the device are the same as described in Section 3.1.5.

3.2.2 Perovskite solar cells

Perovskite solar cells are devices based on materials having the same crystal structure as Calcium Titanate ($CaTiO_3$), known as Perovskite structure.[3] This has a ABX_3 structure, where A is a monovalent cation, B a divalent metal cation and X a halogen anion.

The perovskite structure can only exist for some values of the Goldsmith tolerance factor t, defined as

$$t = \frac{R_X + R_A}{\sqrt{2}(R_X + R_B)} \tag{3.34}$$

where R_i is the radius of the i ion.

A perfect cubic perovskite is obtained $t = 1$, however, a cubic perovskite can also be formed for values of $0.9 \leq t \leq 1$. With $0.7 \leq t \leq 0.9$ other structures like tetragonal, rhombohedral, hexagonal or orthorhombic are formed.

The archetypical perovskite material for solar cells employs methylammonium (MA, CH_3NH_3) on the A site, Lead (Pb) on the B site and Iodine (I) on the X side.

The polycrystalline film used in solar devices has a very high extinction coefficient[4], with a bandgap of $E_G \sim 1.55$eV. It has a very wide absorption across the visible spectrum, with a sharp edge around 780 nm, extending up to low wavelengths. It has a low trap density and a diffusion length exceeding 1 μm.[5,6] The high dielectric constant makes excitonic effects negligible, with an exciton binding energy of few meV[7] that causes the generation of immediatelt free carriers.

The most common device architecture is the n-i-p shown in Figure 3.7. Light is absorbed in the perovskite layer and charges are generated. This active layer is sandwiched between to carrier-selective layers to facilitate charge separation and reduce recombination. Electrons are collected by an n-type layer, typically TiO_2 or SnO_2. Electrodes are then collected by a transparent electrode, typically glass coated with fluorine-doped tin oxide (FTO). On the other side, the most common layer is 2,2',7,7'-Tetrakis[N,N-di(4-methoxyphenyl)amino]-9,9'-spirobifluorene (spiro-OMeTAD), a small-molecule working as a hole transporting material.[8] To increase the performances, spiro-OMeTAD is often treated with additives like 4-*tert* butylpyridine (tBP) to improve the holes extraction from the active layer[9] and lithium bis(trifl uoromethanesulfonyl)imide (Li-TFSI) salts to increase the mobility of the hole conducting layer.[10]

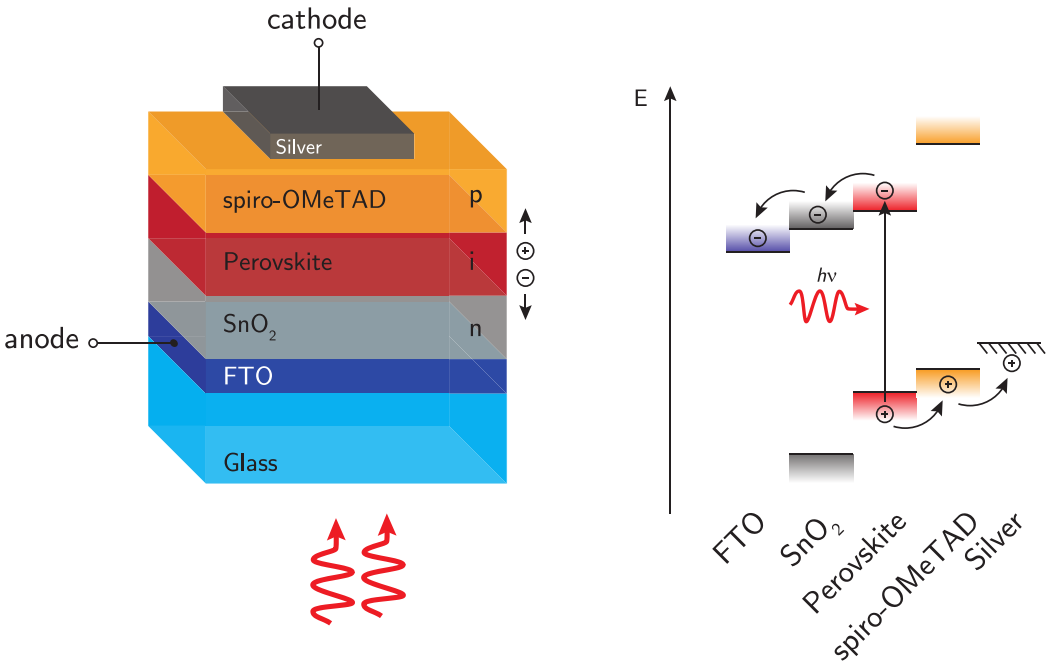

Figure 3.7: Structure of a perovskite solar cell and its energy bands diagram. (a) The schematic picture shows the layers of a typical solar cell. The light coming from the glass side is absorbed in the perovskite layer. Charges diffuse to the interface, with the hole being injected in the spiro-OMeTAD layer and the electrons in the SnO_2. The charges are the collected by the external circuit through the FTO and layer (anode) and the silver layer (cathode). (b) Qualitative alignment of the energy level diagram in perovskite solar cells. Electron generated in the perovskite layer have a favourable energetic landscape when travelling towards the FTO layer, while holes are blocked by the SnO_2 layer, but their transport can happen through the spiro-OMeTAD towards the silver electrode.

It is also possible to invert the architecture and build an n-i-p device, with the most common devices employing poly(3,4-ethylenedioxythiophene) polystyrene sulfonate (PEDOT:PSS) as a hole transporting layer and phenyl-C61-butyric acid methyl ester ($PC_{60}BM$) as an electron transporting layer.[11]

One of the major advantages of perovskites is the possibility to tune the optoelectronic properties, as any combination of materials satisfying the condition of Eq. 3.34 allows the formation of a perovskite.

By increasing the size of the cation of the A site with Cesium (Cs) or formamidinium (FA, $CH(NH_2)_2^+$), and replacing the Iodine on the B site with Bromide it has been possible to change the bandgap of the absorber, and by changing the ratio of the elements it is possible to tune the bandgap, making the material extremely appealing for tandem applications.[12,13]

A second important advantage is the ease of process. The most common technique on a lab-scale consists in spin-coating a solution containing the precursors of the perovskite and enabling the crystal formation by annealing the film, washing with an anti-solvent or a combination of the two.[14] This can be done in one step or in a sequential deposition of different precursors. Other successful deposition methods involve printing, spraying, vacuum deposition.

One of the main problems of perovskite solar cells regards their stability, both on a structural and chemical aspect.

Structural stability regards the phase change of perovskite depending on the operation temperature. Studies on MAPbX perovskites demonstrate the crystallographic stability of the material across a wide range of temperature. However, methylammonium halides have a very low melting point, causing perovskites of this class to rapidly degrade at 150°C.

The main problem lies in the chemical stability. Perovskites are highly sensitive to moisture or polar solvents, due to the hygroscopicity of the organic compound. The mechanism of the degradation process was described in detail by Leguy *et al.*[15] Moisture can penetrate the film through the grain boundaries at relative humidity as

low as 10%, inducing a chemical change of the perovskite, as water can form stronger bonds with the MA, which is normally bound to the perovskite structure via weak hydrogen bonds. The hydration has been shown to be reversible by re-heating the film, but an excess of moisture or an extended exposure leads to phase segregation, preventing the re-formation of the perovskite.

The hydration is a two-step process. First, for low exposure time, a single molecule of water entering in the perovskite unit cell forms the mono-hydrate phase $CH_3NH_3PbI_3 \cdot H_2O$. Then, additional exposure causes the formation of the di-hydrated phase, resulting in the separation of the lead iodide. This can be summarised with the following:

$4\,(CH_3NH_3)PbI_3 + 4\,H_2O \rightleftharpoons 4\,[CH_3NH_3PbI_3 \cdot H_2O] \rightleftharpoons (CH_3NH_3)_4PbI_6 \cdot 2\,H_2O + 3\,PbI_2 + 2\,H_2O$

With excessive exposure, the reaction is eventually pushed to the right, causing the dissolution of $CH_3NH_3{}^+$ and turning into an irreversible process via

$(CH_3NH_3)_4PbI_6 \cdot 2\,H_2O(s) \xrightarrow{H_2O(l)} 4\,CH_3NH_3I(aq) + PbI_2(s) + 2\,H_2O(l).$

Strategies to increase the stability mainly consist in modifying the perovskite or introducing barriers to encapsulate the material from moisture.

The first strategy showed good results by replacing the methylammonium (MA) with formamidinium (FA), which shows a slower degradation when heated.[12]. Despite the better stability, $FABI_3$ goes through a phase transition at room temperature, and the cubic phase co-exist with the hexagonal phase.[16] This is improved by using a mixed composition with a double cation FA/MA (with MA below 20%),[17] or with a triple cation with FA, MA and Cs.[18] Stability is further improved by mixing iodine and bromide on the B site.[17] The composition with Cs and FA alone has also demonstrated excellent lifetime, and it is today the one with the best stability performance.[13,19,20]

The second strategy consists in encapsulating the material, *i.e.* the use of barriers to keep the moisture out. One of the main problems lies in the Li-TFSI additive used to dope the hole transporting layer, as its hygroscopicity facilitate the moisture penetration into the device, so a focus has been put in synthesising new hole transporting

materials that do not require dopants and simultaneously able to encapsulate the perovskite.[21,22] Other approaches consist in adding a very thin barrier between the hole transporting layer and the perovskite, such as a layer of AlO_2 deposed via atomic layer deposition (ALD).[23] Finally, a very successful strategy developed by Habisreutinger *et al.*[24] has been the use of carbon nanotubes infiltrated with inert, hydrophobic polymers, which will be described more in detail in the following section 3.2.3.

3.2.3 Use of carbon nanotubes in perovskite solar cells

Due to their electronic properties, carbon nanotubes have generated a lot of interest for their use in solar cells, including perovskite solar cells. A comprehensive review has been written by Habisreutinger *et al.*[25], and the most notable works will be summarised here.

A first attempt to employ carbon nanotubes was made by Chen *et al.*[26], by embedding MWCNTs in a layer P3HT (2 wt%) in a solar cell with structure mp-TiO2/MAPbI3/P3HT–MWCNT/Au. They observed that the MWCNTs improved the crystallinity of the P3HT enhancing its conductivity. This resulted in a better fill factor (57% compared to 45%) and an improvement in the efficiency from 4.12% to 6.45%.

Li *et al.*[27] used a free-standing film of single- and double-walled CNTs laminated directly on the perovskite layer, acting simultaneously as a cathode and hole-extracting layer. The devices showed an efficiency of 6.02% with a fill factor 0.49 and a V_{OC} of 0.83 V. This was justified with a lack of carrier selectivity and the high resistivity of the CNTs film, and the performances were improved by spin-coating an additional layer of spiro-OMeTAD on top of the CNT, resulting in an efficiency of 9.9%, a V_{OC} of 1.0 V and a FF of 55%.

Similarly, Lee *et al.*[28] embedded MWCNTs in spiro-OMeTAD to increase its conductivity. While the FF of the device improved with the increase of the MWCNTs loading (form 0 wt% to 2wt%), the V_{OC} decreased as well as the efficiency, and this was attributed to a back-electron transfer when the MWCNT contacted the perovskite

directly. This was improved by adding a thin layer of pristine spiro-OMeTAD between the perovskite and the spiro-OMeTAD-MWCNT composite, resulting in an increase of the efficiency from 12.8% to 15.1%.

A different approach was used by Jeon *et al.*[29] They used inverted p-i-n devices using SWCNT as a transparent electrode, then removing the need for transparent conductive oxides such as indium-doped tin oxide (ITO) or FTO. They built flexible solar cells on PET covered with nitric acid (HNO_3) doped SWCNT. The acid treatment allowed them to deposit PEDOT:PSS on top of them as a hole transporting layer, while this is normally not possible due to the hydrophilic nature of PEDOT:PSS and the hydrophobicity of SWCNT. They then used $PC_{60}BM$ as an electron transporting layer, obtaining an efficiency of 5.38%.

Habisreutinger *et al.*[30] worked on the use of carbon nanotubes as a stable hole-extracting layer, with the aim of removing the need for the reactive and hygroscopic Li-TFSI dopants. In his work, he used P3HT wrapped SWCNT, with the hypothesis that the p-type P3HT wrapping the carbon nanotubes could improve the charge selectivity. The polymer-wrapped SWCNT were deposited on the perovskite and covered with a layer of undoped spiro-OMeTAD. This architecture reached an efficiency of 15.4%, and photoinduced absorption measurements demonstrated that charge extraction was improved by one order of magnitude compared to the use of neat spiro-OMeTAD.

Based on this result, in a follow-up work[24] the thin spiro-OMeTAD layer was replaced by an inert matrix of PMMA or polycarbonate (PC), (device structure in Figure 3.8) with the assumption that SWCNT were responsible on their own for the majority of charge extraction and transport.

The devices delivered a PCE of 15.3%, and despite being electrically inert, the polymer matrix resulted to be fundamental, as devices employing SWCNT only showed a very poor fill factor caused by a low shunt-resistance and a lower open-circuit voltage. It was then speculated that the polymer prevents direct contact between the metal

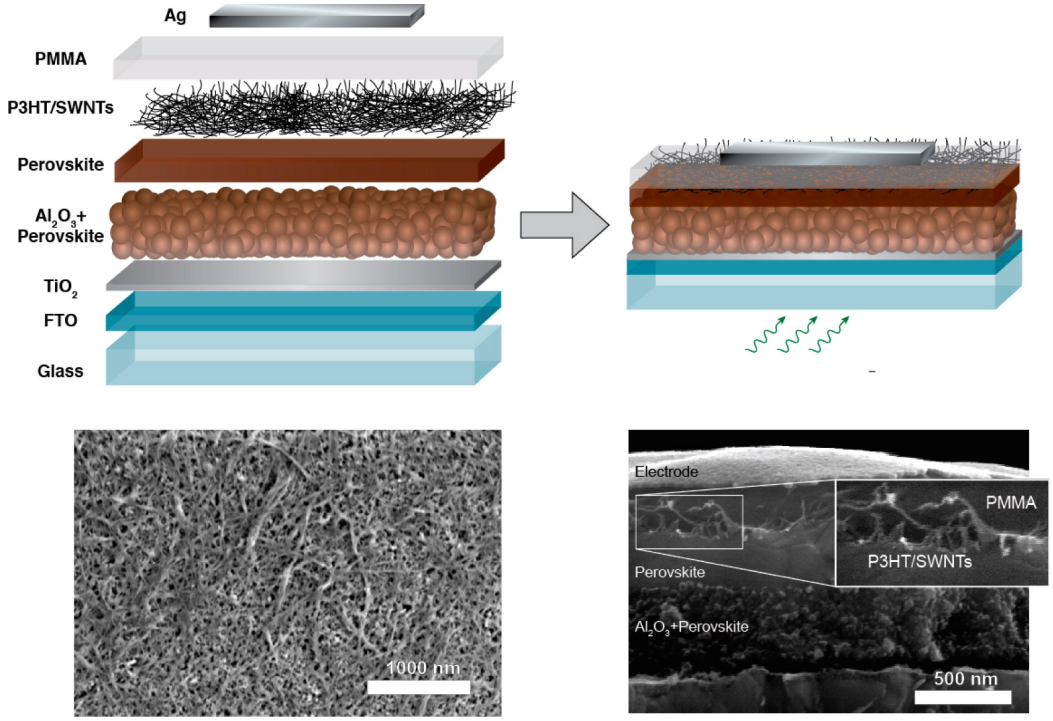

Figure 3.8: Schematic illustration of the solar cell with a carbon nanotube/polymer composite as hole-transporting structure. The schematic architecture of the investigated device consisting of sequential layers of FTO as a transparent electrode, a TiO2 compact layer, a mesostructured layer of Al2O3 coated with $CH_3NH_3PbI_{3-x}Cl_x$ and the hole transporting structure composed of a P3HT/SWNT layer in-filled with a PMMA matrix. Reproduced with permission from reference [24]. Copyright 2014 American Chemical Society.

electrode and the active layer by filling any gap in the SWCNT network, which would cause recombination and shunt pathways.

Additionally, the inert polymer matrix has the additional role of offering a protective barrier to encapsulate the perovskite film. Thermal stress experiments at 80°C showed that devices maintained ∼70% of their initial efficiency when using PC and ∼60% with PMMA, while standard devices with doped spiro-OMeTAD had a decrease to 20% of their original efficiency.

More impressively, the authors were able to expose the unencapsulated solar cell for 1 min under running water causing only negligible effects on the performance.

In a following study,[31] the authors showed that the devices with SWCNT can outperform the standard architecture using spiro-OMeTAD delivering a steady-state power output (SPO) of 18.8%. In that work, they used a perovskite with both mixed organic A-site cations and mixed halides $FA_{0.83}MA_{0.17}Pb(I_{0.83}Br_{0.17})_3$. The electron transporting layer was a film of SnO_2 and the hole-transporting layer again a film of P3HT-wrapped SWCNT infiltrated with undoped spiro-OMeTAD.

3.3 Summary

This chapter briefly discussed the fundamental concepts of photovoltaics. Starting with the description of semiconductors, it was described how these materials can be treated as 2 levels absorbers, and the processes of light absorption, carrier generation, recombination and transport were discussed.

It was then shown that with asymmetric transport this materials can be used as devices to transform light into electrical power, and the fundamental parameters to characterise such a device were introduced.

The second section of the chapter described the most common realisation of solar cells, starting with the very common p-n junction, which is currently the most commercially successful technology.

The last section described perovskite solar cells, which has been the fastest growing technology in the last decade. A description of the materials used and the device structure was given, with a particular focus on the instability issue, specifically in presence of water. This has been one of the main concerns in the scientific community, especially because the most used hole transporting material, spiro-OMeTAD relies on the uses of very hygroscopic Li-TFSI dopants. Finally, a review on the use of carbon nanotubes in these devices was presented, with a focus on their application as charge extraction layers. This has been a successful technology responding to the need of better electrodes, as it allows to remove the hygroscopic dopants and encapsulate the perovskite layer.

Bibliography

1. P. Würfel, *Physics of Solar Cells: From Basic Principles to Advanced Concepts*. Weinheim, Germany: Wiley-VCH Verlag GmbH, 3rd ed., 2009.

2. J. Nelson, *The Physics of Solar Cells*. London, UK: Imperial College Press, 2003.

3. R. S. Roth, "Classification of Perovskite and Other ABO3-Type Compounds," *Journal of Research of the National Bureau of Standards*, vol. 58, no. 2, pp. 75–88, 1957.

4. S. Sun, T. Salim, N. Mathews, M. Duchamp, C. Boothroyd, G. Xing, T. C. Sum, and Y. M. Lam, "The origin of high efficiency in low-temperature solution-processable bilayer organometal halide hybrid solar cells," *Energy Environ. Sci.*, vol. 7, no. 1, pp. 399–407, 2014.

5. S. D. Stranks, G. E. Eperon, G. Grancini, C. Menelaou, M. J. P. Alcocer, T. Leijtens, L. M. Herz, A. Petrozza, and H. J. Snaith, "Electron-Hole Diffusion Lengths Exceeding 1 Micrometer in an Organometal Trihalide Perovskite Absorber," *Science*, vol. 342, no. 6156, pp. 341–344, 2013.

6. G. Xing, N. Mathews, S. Sun, S. S. Lim, Y. M. Lam, M. Grätzel, S. Mhaisalkar, and T. C. Sum, "Long-range balanced electron-and hole-transport lengths in organic-inorganic $CH_3NH_3PbI_3$," *Science*, vol. 342, no. 6156 LB - Xing2013, pp. 344–347, 2013.

7. A. Miyata, A. Mitioglu, P. Plochocka, O. Portugall, J. T. W. Wang, S. D. Stranks, H. J. Snaith, and R. J. Nicholas, "Direct measurement of the exciton binding energy and effective masses for charge carriers in organic-inorganic tri-halide perovskites," *Nature Physics*, vol. 11, no. 7, pp. 582–587, 2015.

8. J. Salbeck, N. Yu, J. Bauer, F. Weissörtel, and H. Bestgen, "Low molecular organic glasses for blue electroluminescence," *Synthetic Metals*, vol. 91, no. 1-3, pp. 209–215, 1997.

9. S. N. Habisreutinger, N. K. Noel, H. J. Snaith, and R. J. Nicholas, "Investigating the Role of 4-Tert Butylpyridine in Perovskite Solar Cells," *Advanced Energy Materials*, vol. 7, no. 1, pp. 1–8, 2017.

10. T. Leijtens, J. Lim, J. Teuscher, T. Park, and H. J. Snaith, "Charge density dependent mobility of organic hole-transporters and mesoporous TiO2determined by transient mobility spectroscopy: Implications to dye-sensitized and organic solar cells," *Advanced Materials*, vol. 25, no. 23, pp. 3227–3233, 2013.

11. T. Liu, K. Chen, Q. Hu, R. Zhu, and Q. Gong, "Inverted Perovskite Solar Cells: Progresses and Perspectives," *Advanced Energy Materials*, vol. 6, no. 17, pp. 1–17, 2016.

12. G. E. Eperon, S. D. Stranks, C. Menelaou, M. B. Johnston, L. M. Herz, and H. J. Snaith, "Formamidinium lead trihalide: a broadly tunable perovskite for efficient planar heterojunction solar cells," *Energy & Environmental Science*, vol. 7, no. 3, p. 982, 2014.

13. D. P. McMeekin, G. Sadoughi, W. Rehman, G. E. Eperon, M. Saliba, M. T. Horantner, A. Haghighirad, N. Sakai, L. Korte, B. Rech, M. B. Johnston, L. M. Herz, and H. J. Snaith, "A mixed-cation lead mixed-halide perovskite absorber for tandem solar cells," *Science*, vol. 351, no. 6269, pp. 151–155, 2016.

14. M. M. Lee, J. Teuscher, T. Miyasaka, T. N. Murakami, and H. J. Snaith, "Efficient Hybrid Solar Cells Based on Meso-Superstructured Organometal Halide Perovskites," *Science*, vol. 338, no. 6107, pp. 643–647, 2012.

15. A. M. Leguy, Y. Hu, M. Campoy-Quiles, M. I. Alonso, O. J. Weber, P. Azarhoosh, M. Van Schilfgaarde, M. T. Weller, T. Bein, J. Nelson, P. Docampo, and P. R. Barnes, "Reversible hydration of $CH_3NH_3PbI_3$ in films, single crystals, and solar cells," *Chemistry of Materials*, vol. 27, no. 9, pp. 3397–3407, 2015.

16. M. T. Weller, O. J. Weber, J. M. Frost, and A. Walsh, "Cubic Perovskite Structure of Black Formamidinium Lead Iodide, α-$[HC(NH_2)_2]PbI_3$, at 298 K," *The Journal of Physical Chemistry Letters*, vol. 6, no. 16, pp. 3209–3212, 2015.

17. N. J. Jeon, J. H. Noh, W. S. Yang, Y. C. Kim, S. Ryu, J. Seo, and S. I. Seok, "Compositional engineering of perovskite materials for high-performance solar cells," *Nature*, vol. 517, no. 7535, pp. 476–480, 2015.

18. M. Saliba, T. Matsui, J.-Y. Seo, K. Domanski, J.-P. Correa-Baena, M. K. Nazeeruddin, S. M. Zakeeruddin, W. Tress, A. Abate, A. Hagfeldt, and M. Grätzel, "Cesium-containing triple cation perovskite solar cells: improved stability, reproducibility and high efficiency," *Energy & Environmental Science*, vol. 9, no. 6, pp. 1989–1997, 2016.

19. Z. Wang, D. P. McMeekin, N. Sakai, S. van Reenen, K. Wojciechowski, J. B. Patel, M. B. Johnston, and H. J. Snaith, "Efficient and Air-Stable Mixed-Cation Lead Mixed-Halide Perovskite Solar Cells with n-Doped Organic Electron Extraction Layers," *Advanced Materials*, vol. 29, no. 5, p. 1604186, 2017.

20. Z. Wang, Q. Lin, F. P. Chmiel, N. Sakai, L. M. Herz, and H. J. Snaith, "Efficient ambient-air-stable solar cells with 2D–3D heterostructured butylammonium-caesium-formamidinium lead halide perovskites," *Nature Energy*, vol. 2, no. 9, p. 17135, 2017.

21. Y. S. Kwon, J. Lim, H. J. Yun, Y. H. Kim, and T. Park, "A diketopyrrolopyrrole-containing hole transporting conjugated polymer for use in efficient stable organic-inorganic hybrid solar cells based on a perovskite," *Energy and Environmental Science*, vol. 7, no. 4, pp. 1454–1460, 2014.

22. L. Zheng, Y.-H. Chung, Y. Ma, L. Zhang, L. Xiao, Z. Chen, S. Wang, B. Qu, and Q. Gong, "A hydrophobic hole transporting oligothiophene for planar perovskite solar cells with improved stability," *Chem. Commun.*, vol. 50, no. 76, pp. 11196–11199, 2014.

23. D. Koushik, W. J. H. Verhees, Y. Kuang, S. Veenstra, D. Zhang, M. A. Verheijen, M. Creatore, and R. E. I. Schropp, "High-efficiency humidity-stable planar perovskite solar cells based on atomic layer architecture," *Energy & Environmental Science*, vol. 10, no. 1, pp. 91–100, 2017.

24. S. N. Habisreutinger, T. Leijtens, G. E. Eperon, S. D. Stranks, R. J. Nicholas, and H. J. Snaith, "Carbon nanotube/polymer composites as a highly stable hole collection layer in perovskite solar cells," *Nano Letters*, vol. 14, no. 10, pp. 5561–5568, 2014.

25. S. N. Habisreutinger, R. J. Nicholas, and H. J. Snaith, "Carbon Nanotubes in Perovskite Solar Cells," *Advanced Energy Materials*, vol. 7, no. 10, pp. 1–7, 2017.

26. H. Chen, X. Pan, W. Liu, M. Cai, D. Kou, Z. Huo, X. Fang, and S. Dai, "Efficient panchromatic inorganic-organic heterojunction solar cells with consecutive charge transport tunnels in hole transport material," *Chemical Communications*, vol. 49, no. 66, pp. 7277–7279, 2013.

27. Z. Li, S. A. Kulkarni, P. P. Boix, E. Shi, A. Cao, K. Fu, S. K. Batabyal, J. Zhang, Q. Xiong, L. H. Wong, N. Mathews, and S. G. Mhaisalkar, "Laminated carbon nanotube networks for metal electrode-free efficient perovskite solar cells," *ACS Nano*, vol. 8, no. 7, pp. 6797–6804, 2014.

28. J. Lee, M. M. Menamparambath, J.-Y. Hwang, and S. Baik, "Hierarchically Structured Hole Transport Layers of Spiro-OMeTAD and Multiwalled Carbon Nanotubes for Perovskite Solar Cells," *ChemSusChem*, vol. 8, no. 14, pp. 2358–2362, 2015.

29. I. Jeon, T. Chiba, C. Delacou, Y. Guo, A. Kaskela, O. Reynaud, E. I. Kauppinen, S. Maruyama, and Y. Matsuo, "Single-Walled Carbon Nanotube Film as Electrode in Indium-Free Planar Heterojunction Perovskite Solar Cells: Investigation of Electron-Blocking Layers and Dopants," *Nano Letters*, vol. 15, no. 10, pp. 6665–6671, 2015.

30. S. N. Habisreutinger, T. Leijtens, G. E. Eperon, S. D. Stranks, R. J. Nicholas, and H. J. Snaith, "Enhanced hole extraction in perovskite solar cells through carbon nanotubes," *Journal of Physical Chemistry Letters*, vol. 5, no. 23, pp. 4207–4212, 2014.

31. S. N. Habisreutinger, B. Wenger, H. J. Snaith, and R. J. Nicholas, "Dopant-Free Planar n–i–p Perovskite Solar Cells with Steady-State Efficiencies Exceeding 18%," *ACS Energy Letters*, vol. 2, no. 3, pp. 622–628, 2017.

CHAPTER 4

Materials and methods

This chapter provide a brief description of the material, methods and techniques used in this thesis. Information about the materials are reported as provided from the suppliers.

4.1 Materials

4.1.1 Single-walled carbon nanotubes

Carbon nanotubes used in this thesis are commercially available. They come in a dry powder, they differ from their production method and their characteristics are summarised in the following paragraphs.

HiPCO single walled carbon nanotubes

Carbon nanotubes produced with the high-pressure carbon monoxide disproportionation (HiPCO) method[1] by were purchased from Nanointegris in the "purified" grade and

used as received. The diamater range is 0.8 nm - 1.2 nm, and the length 100 nm - 1000 nm.

CG200 single walled carbon nanotubes

CG200 SWCNTs produced with the Cobalt–Molybdenum catalysts (CoMoCAT) method[2] were bought from Sigma-Aldrich and used as received. The diameter range is 0.7-1.4 nm.

Nanocyl MWCNT

Multiwalled carbon nanotubes produced via the Catalytic Chemical Vapor Deposition (CCVD)[3] method were provided by Nanocyl, and used as received. Typical lenght observed with AFM measurements is 1000 nm.

4.1.2 Polymers

Ethylene-vinyl acetate (EVA)

ethylene-vinyl acetate (EVA) was provided by DuPont free of charge in a 1 kg bag. The formulation is the "Elvax© 150", having a 32% by weight vinyl acetate comonomer content.

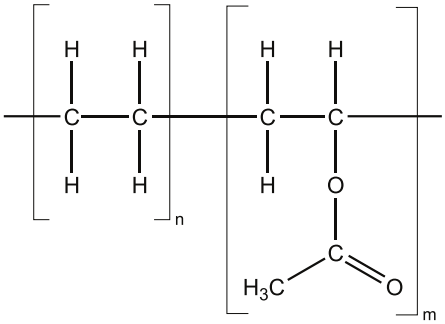

Figure 4.1: Chemical structure of ethylene-vinyl acetate

EVA is a widely used polymer when good mechanical properties and hydrophobicity are required. The composition used in this thesis is the same used to encapsulate

silicon solar modules. Such EVA films are know for their high transparent and has a low water vapour transmission rate (WVTR).[4]

P3HT

Regio-regular poly(3-hexylthiophene) (P3HT) was bought fro Rieke Metals Inc. and used as received. The average molecular weight is M_w = 50 000 g mol^{-1}, and the regioregularity is 95%.

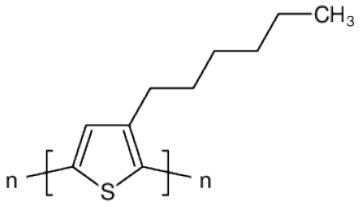

Figure 4.2: Chemical structure of poly(3-hexylthiophene) (P3HT)

4.2 Fabrication methods

4.2.1 Substrate preparation

Glass substrates used in this thesis are produced by Corning (Eagle XG glass) and supplied by Thin Film Devices Inc, (USA). FTO substrates (TEC7) for devices fabrication are provided by NGS, UK.

Substrates were cleaned by bath-sonication at 50°C sequentially in a 2% solution of Hellmanex in de-ionised water, pure de-ionised water, acetone, 2-propanol and dried with compressed dry air.

Before the deposition of films, substrates where additionally treated with a UV-Ozone cleaner for 10 minutes.

4.2.2 Spray-coating

CNT films in this thesis were fabricated using a custom-made spray coater built by Dr Grey Christoforo (Department of Physics, University of Oxford).[5]

The system was equipped with a heated stage where substrates are placed. The stage and as a result temperature was set to 100°C for all the experiments in this thesis. The solution was delivered to a pneumatic nozzle with a syringe pump, which atomises the solution with the aid of a high pressure stream of compressed air ($\sim$ 6 bars). The height of the nozzle is adjustable, and for all the experiments in this thesis has been set to 100 mm above the substrate. The deposition happens by rastering the substrates with multiple passes until the set amount of solution has been delivered. For the experiments in this thesis, a fixed amount of 40 mL was sprayed for every run, and the film thickness was controlled by changing the concentration of the solution.

In the case of poorly soluble materials like CNT, spray-coating offers the ability to uniformly deposit thicker layers with multiple depositions. This is achievable as the high flow of the carrier gas causes the evaporation of most of the solvent before the material reaches the substrate. On the contrary, with the majority of other solution-based techniques the evaporation of the solvent happens once the solution has been already deposited on the substrate, therefore a sequential deposition will risk washing any previously deposited layer, causing a non uniformity of the film.

4.2.3 Polymer wrapping of CNT

.

The polymer wrapping of CNT with EVA is novel in this thesis and is described in detail in Chapter 5. This section describes the procedure to prepare P3HT-wrapped CNT used in the control solar cellsof Chapter 7.

2.5 mg of CG200 SWCNT were dispersed in 5.0 mL of a solution of 0.6 mg/mL of P3HT in chlorobenzene by sonicating with a horn sonicator for 10 min. 5 mL of

chlorobenzene were added after the sonication, and the dispersion is centrifuged for 8 min at 10,000 g to remove non-wrapped carbon nanotubes. The precipitate was recovered and 10 mL of toluene were added and the solution heated to 80 °C for 1h to induce the aggregation of the functionalised tubes, while mantaining the excess P3HT dissolved. The mixture was then centrifuged at 16,000 g and the precipiate, consisting of P3HT-wrapped tubes, was recovered and dispersed in 6 mL of chloroform.

4.2.4 Solar cell fabrication

Perovskite solar cells were fabricated using a cleaned FTO-coated glass substrate.

Two different kind of pervoskite solar cells were prepared, $FA_{0.83}MA_{0.17}Pb(I_{0.83}Br_{0.17})_3$ and $FA_{0.83}Cs_{0.17}Pb(I_{0.9}Br_{0.1})_3$ (where FA is formamidinium, $CH(NH_2)_2$ and MA is metil-ammonium, CH_3NH_3). The fabrication procedure is the same, with the exception of the perovskite precursor solution.

A thin SnO_2 film was deposited according to the method described by Anaraki *et al.*[6] A solution of 0.05 M tin(IV) chloride pentahydrate ($SnCl_4 \cdot 5\,H_2O$, Sigma-Aldrich) dissolved in anhydrous isopropanol by stirring for 30 min at room temperature was deposited on FTO-coated glass substrates by spin-coating at 3000 rpm spin rate for 30 s. Substrates were then annealed in two steps: 100 °C for 10 min and 180 °C for 1 h.

The films were then treated with a chemical bath for 3 h at 70 °C. The bath solution prepared by dissolving 500 mg urea (Sigma-Aldrich) in 40 ml deionized water, then adding 10 ml of 3-mercaptopropionic acid (Sigma-Aldrich) and 0.5 mL of hydrochloric acid (37 wt%) and finally dissolving tin(II) chloride dihydrate ($SnCl_2 \cdot 2\,H_2O$Sigma-Aldrich) at a 0.002 M concentration by stirring for 2 min. The treated substrates were then rinsed in a sonication bath of deionized water for 2 min, dried with nitrogen and annealed at 180 °C for 1 h.

The $FA_{0.83}MA_{0.17}Pb(I_{0.83}Br_{0.17})_3$ precursor solution was obtained as described by Jeon *et al.*[7] by dissolving 1.25 M formamidinium iodide (FAI, Dyesol), 0.25

M methylammonium bromide (MAI, Dyesol), 0.25 M lead bromide ($PbBr_2$, Alfa Aesar), and 1.375 M lead iodide (PbI_2, TCI) in a 4:1 mixture by volume of N,N-dimethyformamide (DMF) and N,N-dimethyl sulfoxide (DMSO) and stirring it for 15 min at 65 °C.

The $FA_{0.83}Cs_{0.17}Pb(I_{0.9}Br_{0.1})_3$ perovskite precursor solution was prepared as described by McMeekin *et al.*[8] by dissolving 1.25 M formamidinium iodide (FAI, Dyesol), 0.25 M cesium iodide (CsI; Alfa Aesar), 0.25 M lead bromide ($PbBr_2$, TCI) and 1.375 M lead iodide (PbI_2, TCI) in a 4:1 mixture by volume of N,N-dimethyformamide (DMF) and N,N-dimethyl sulfoxide (DMSO) and stirred overnight in a nitrogen glovebox at room temperature.

The perovskite precursor solutions were spin-coated using a two step program (10 s at 1000 rpm and 35 s at 6000 rpm) with dripping of anisole (Sigma-Aldrich) as anti-solvent 10 s before the end of the second step. The films were then annealed at 100 °C for 60 min. All films were spin-coated in a drybox with relative humidity below 20%.

Depending on the experiment, a film of EVA-CNTs or P3HT-CNT was deposited. Films of EVA-CNTs were deposited by spray-coating, while films of P3HT-CNT where deposited by drop-by-drop spin-coating from 200 μL of solution.

A film of spiro-OMeTAD was then deposited to infiltrate the CNT. The solution was prepared by dissolving 85 mg of spiro-OMeTAD in 1 mL of chlorobenzene and stirring on a hotplate at 90 °C for 10 min. Once cooled down, 33 µL of tert-butylpyridine (tBP) were added, and the solution was deposited by spin-coating at 2,000 rpm for 45 s.

In devices without a polymer-CNT film, the spiro-OMeTAD solution was doped by adding 20 μL/mL of a solution of 500 mg/mL lithium bis(trifl uoromethanesulfonyl)imide (Li-TFSI) (Sigma-Aldrich) dissolved in 1-butanol (Sigma-Aldrich).

Finally, 100 nm thick gold or silver electrodes were deposited by thermal evaporation through a mask in a vacuum chamber with base pressure $<7\times10^{-6}$ mbar. The device area is defined by the overlap of the gold film and the FTO.

4.3 Characterisation

4.3.1 Absorption spectroscopy

Absorption spectroscopy measurements were carried out with a Perkin-Elmer Lambda 1050 UV-vis-NIR Spectrophotometer using 1 nm steps.

4.3.2 Photoluminescence excitation spectroscopy

photoluminescence excitation (PLE) excitation spectroscopy was carried out with a custom made setup, schematically represented in Figure 4.3. Light is generated by a 75W Xenon lamp (Photon Technology International Inc.) and it is filtered by a 30 cm monochromator in 5 nm steps. A short pass filter stops unwanted IR radiation, and in order to correct the spectral output of the Xenon lamp and the monochromator spectral response, a quartz beam splitter (BS) diverts a fraction of the light onto a silicon photodiode to measure the intensity, which is used to normalise the PLE signal. Light from the main beam then excites the sample, and the photoluminescence emission is filtered by a long pass filter to remove any radiation from the excitation lamp and resolved by a spectrometer, to get finally collected by a liquid nitrogen cooled InGaS photodiode array (OMA V, Princeton Instruments). The system is calibrated with a Neon lamp before each measurement.

4.3.3 Raman spectroscopy

Raman spectroscpy was carried out with a Jobin Yvon T64000 triple spectrometer, which is calibrated with a Silicon sample before each measurement. Samples were excited with a Melles griot He:Ne laser ($\lambda = 633nm$) or a Ventus solo Nd:YAG laser ($\lambda = 532nm$). The triple spectrometer uses the first two gratings to subtract the light at the excitation frequency, and the third stage resolves the Raman signal coming

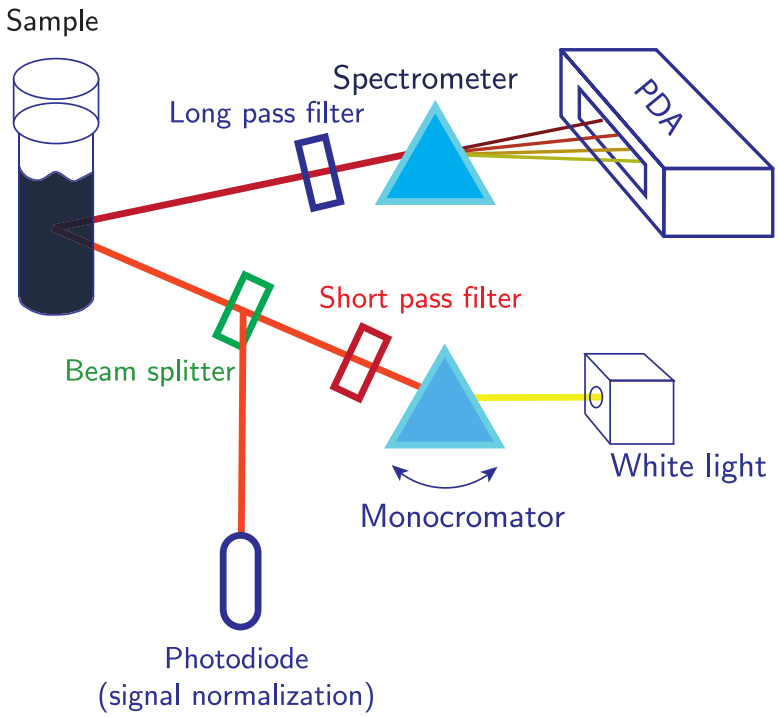

Figure 4.3: Schematic diagram illustrating the photoluminescence excitation setup. The white light is filtered through a monocromator and additionally filtered to remove any unwanted radiation. Part of the beam is reflected on a photodiode by a beam splitter to normalise the intensity, and the main beam exite the sample, which consist in a solution of carbon nanotubes. The PL is then collected by a filtered to remove any unwanted scattered radiation coming from the excitation light, resolved by a spectrometer and collected by an InGaS photodiode array (PDA).

from the sample, which is collected by a Andor DU420A-OE CCD. The power output of the laser is controlled to have an incident radiation on the sample P<1mW.

4.3.4 Sheet resistance measurements

Sheet resistance has been measured with a 4 point tungsten carbide probes from Jandel Engineering (0.635 mm spacing) and a Keithley 2450 source meter. A maximum current I_{max} is chosen depending on the sample to have a maximum voltage drop of 100 mV/cm, and a sweep scan (20 points, auto sweep delay, NPLC=1) from $-I_{max}$ to I_{max} was applied across the outer probes, while the voltage was measured across the inner probes. The sheet resistance was calculated from the slope of the current-voltage curves corrected with $\pi/\ln(2)$ correction factor for the in-line probe configuration.

Conductivity of carbon nanotubes films have occasionally also been measured in the Van Der Pauw geometry, and values resulted consistent with the four-in-line probes measurements.

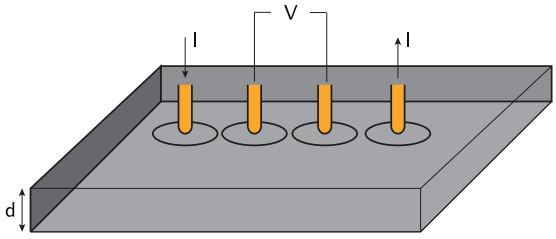

Figure 4.4: Schematic diagram of the four point probe measurement configuration. Probes are 0.635 mm apart. A current I is pushed through the outer probes, and the voltage V is measured across the inner probes.

4.3.5 Atomic Force microscopy

The topography of carbon nanotubes has been measured using an Asylum MFP-3D atomic force microscope. Images have been collected in non-contact mode, using a Bruker NCHV-A n-doped silicon probe with a scan rate of 0.6 Hz and 1024 sample/lines.

4.3.6 Solar cells characterisation

JV characteristics of solar cells were measured under a simulated AM1.5 light with 1000 W/m^2 intensity by a class AAB ABET Technologies Sun 2000 simulator with a Keithley 2400 sourcemeter. The lamp is calibrated monthly with an NREL-certified KG5 filtered silicon reference diode with a mismatch factor of 1.01 to a solar device having the same perovskite absorber of the devices under test. Solar cells have an active area defined by the overlap between the metal and the FTO electrode of about 12mm^2 and they are masked to have an illuminated area of 9.19 mm^2 during measurement. JV curves are obtained by applying a sweep voltage to the device between 0 V and 1.4 V at a rate of 0.38 V/s, and measuring the current passing through the device. As perovskite devices exhibit a hysteretic behaviour, resulting in a different JV characteristic depending on the direction of the sweep voltage, an additional parameter commonly reported is the steady-state power output (SPO). This is determined by holding the device at the voltage of maximum power output (V_{MPP}) for extended time and measuring the corresponding current until it the value measured is constat. In the experiment of this thesis, the SPO has been determined by holding the device at the V_{MPP} for 30s. Shunt resistance (R_{Sh}) values have been calculated with a linear fit of the JV characteristic between 0 V and 0.2 V, and series resistance (R_S) values have been calculated with a liner fit of the JV characteristic in the region of $\pm$ 0.1 V around the open-circuit voltage.

Bibliography

1. M. J. Bronikowski, P. A. Willis, D. T. Colbert, K. A. Smith, and R. E. Smalley, "Gas-phase production of carbon single-walled nanotubes from carbon monoxide via the HiPco process: A parametric study," *Journal of Vacuum Science & Technology A: Vacuum, Surfaces, and Films*, vol. 19, no. 4, pp. 1800–1805, 2001.

2. S. Noda, K. Hasegawa, H. Sugime, K. Kakehi, Z. Zhang, S. Maruyama, and Y. Yamaguchi, "Millimeter-Thick Single-Walled Carbon Nanotube Forests: Hidden Role of Catalyst Support," *Journal of Nanoparticle Research*, vol. 4, no. 1-2, pp. 131–136, 2007.

3. M. José-Yacamán, M. Miki-Yoshida, L. Rendón, and J. G. Santiesteban, "Catalytic growth of carbon microtubules with fullerene structure," *Applied Physics Letters*, vol. 62, no. 2, pp. 202–204, 1993.

4. G. Barber, G. Jorgensen, K. Terwilliger, S. Glick, J. Pern, and T. McMahon, "New barrier coating materials for PV module backsheets," in *Conference Record of the Twenty-Ninth IEEE Photovoltaic Specialists Conference, 2002.*, pp. 1541–1544, IEEE, 2002.

5. G. Christoforo, "LANDS - Large Area Nanoparticle Deposition System." `http://afmd.github.io/LANDS/`. Accessed: 05/10/2018.

6. E. H. Anaraki, A. Kermanpur, L. Steier, K. Domanski, T. Matsui, W. Tress, M. Saliba, A. Abate, M. Grätzel, A. Hagfeldt, and J.-P. Correa-Baena, "Highly efficient and stable planar perovskite solar cells by solution-processed tin oxide," *Energy Environ. Sci.*, vol. 9, pp. 3128–3134, 2016.

7. N. J. Jeon, J. H. Noh, W. S. Yang, Y. C. Kim, S. Ryu, J. Seo, and S. I. Seok, "Compositional engineering of perovskite materials for high-performance solar cells," *Nature*, vol. 517, no. 7535, pp. 476–480, 2015.

8. D. P. McMeekin, G. Sadoughi, W. Rehman, G. E. Eperon, M. Saliba, M. T. Horantner, A. Haghighirad, N. Sakai, L. Korte, B. Rech, M. B. Johnston, L. M. Herz, and H. J. Snaith, "A mixed-cation lead mixed-halide perovskite absorber for tandem solar cells," *Science*, vol. 351, no. 6269, pp. 151–155, 2016.

CHAPTER 5

Solubilisation of carbon nanotubes with a non-conjugated polymer

5.1 Introduction

Chapter 2 introduced the remarkable optical and electronic properties of carbon nanotubes. They have been frequently proposed as an excellent material to be used for transparent conductive coatings, electronic sensors, energy conversion and storage applications.

Commercially available CNTs come in a black powder, very difficult to handle due to the extreme volatility of the compound and the tendency to accumulate electrostatic charge, which cause them to easily fly when moved from their container, with an associated health hazard. The fabrication of films, or more generally the CNTs use in devices is then impeded by these processing difficulties.

An obvious solution to this problem is their solubilisation in suitable solvents, which enables their use exploiting the large variety of deposition from solution techniques

already used in many industries.

The solubility of carbon nanotubes in common organic solvents is very poor, ranging from less than 1 mg/L for ethanol and toluene to 95 mg/L for O-DCB.[1] Even in "good" solvents, carbon nanotubes tend to form aggregates, preventing the isolation of single nanotubes, their efficient use in devices or the study of their properties.

As introduced in section 2.4, the solubilisation of CNTs has been the focus of many works and enabled fundamental spectroscopic studies. The major breakthrough was obtained in 2002 by O'Connell *et al.*,[2] when the use of SDS as a surfactant allowed them to disperse individual SWCNT and measure their fluorescence. The process involved the ultrasonication of the SWCNTs in a solution containing the surfactant and the subsequent centrifugation of the solution to remove of the carbon nanotubes clusters. The formation of micelles around the tube keeps them isolated, preventing them from re-aggregating.

A similar process is commonly used with conjugated polymers. The solubilisation relies on the strong interaction of the π orbitals that causes a non-covalent bond between the polymer and the carbon nanotubes,[3] making them soluble. Being thought to be the main wrapping mechanism, research focused on the use of conjugated polymers, especially for the ability of some of them to select specific chiralities,[4] and only a few reports in literature make use of non-conjugated polymers.

This chapter will show how the use of a non-conjugated polymer, EVA, is able to solubilise carbon nanotubes to produce uniform and stable dispersions, and through solvent engineering it is possible to purify them from the excess, non-bound polymer. These nanohybrids have been studied in this thesis making use of spectroscopic and microscopy techniques, to understand their properties and asses the effective solubilisation of individual CNTs.

5.2 Solubilisation of SWCNTs with EVA

This section describes the preparation of EVA-SWCNT nanohybrids, where SWCNT are dispersed in a solvent through the polymer-wrapping mechanism. The solubilisation resembles the process shown by Nish *et al.*;[4] in this thesis, however, the non-conjugated EVA polymer has been used instead of PFO.

EVA was dissolved in chlorobenzene at a concentration varying between 0.5 mg/mL to 10 mg/mL, depending on the experiment.

5 mg of HiPCO single-walled carbon nanotubes were added to the solution and treated with an ultrasonic probe at a frequency of 23 kHz (25 μm amplitude) for 10 minutes.

During the ultrasonication, tubes bundles are split and the polymer can wrap individual tubes. The resulting solution appears black and uniform, while big tube agglomerates are normally visible by eye when no surfactant is used.

The dispersion was then centrifuged at 10,000 g for 8 minutes. The clustered and insoluble tubes precipitate, while the wrapped tubes stay in the supernatant, which is collected.

As a control, a solution of HiPCO tubes dispersed with SDBS in deuterium oxide (D_2O) was prepared. SDBS solubilises nanotubes in a non-selective way and has been the most common surfactant in a large number of spectroscopic studies in literature, so it offers an excellent reference. D_2O is used instead of water as its absorption in the infrared region is shifted and the overlap with the region of interest is reduced.

The control solution has been prepared by mixing 4 mg of HiPCO tubes in 10 mL of a 10 mg/mL solution of SDBS in D_2O with an ultrasonic probe. The solution is then centrifuged at 16,000 g for 45 minutes to remove any bundled tubes, and the upper 30% of the supernatant is collected.

Figure 5.1 shows the UV-VIS-NIR absorption of the resulting solutions. As a reference, the spectrum of neat EVA dissolved in chlorobenzene and neat SDBS in D_2O are shown.

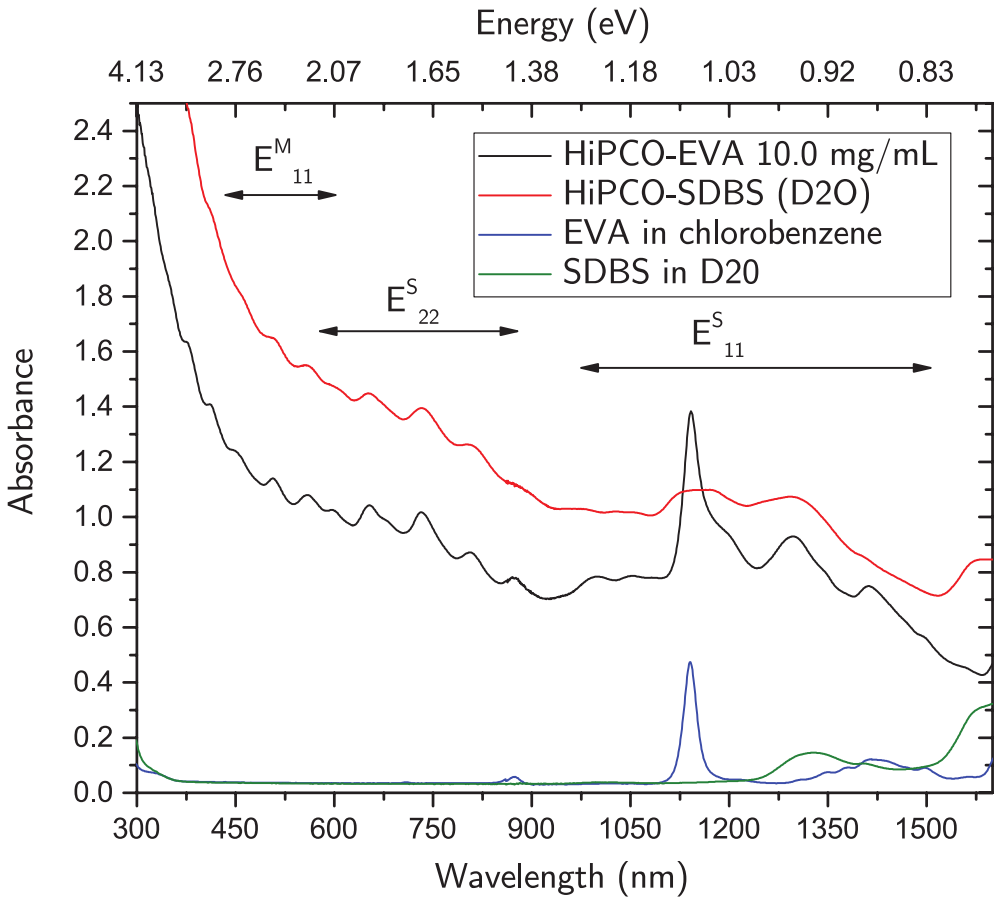

Figure 5.1: Comparison of the absorption spectra of a HiPCO-EVA dispersion in chlorobenzene (solid black line) and a HiPCO-SDBS dispersion in D_2O (red solid line). As a reference, the absorption spectra of the neat EVA in chlorobenzene (solid blue line) and SDBS in D_2O are shown. The HiPCO-EVA and HiPCO-SDBS spectra show numerous Van Hove absorption peaks, with no evident difference in the number or sharpness of peaks. The arrows mark the absorption associated with the E_{ii} transitions, and the superscript identifies metallic or semiconducting CNTs.

Each absorption spectrum shows numerous peaks, assignable to the single Van Hove transitions of individual SWCNTs. The peaks around 273 nm and 1140 nm in the HiPCO-EVA sample are to be attributed to the EVA-CB, as well as the shoulder at 1430 nm in all the spectra. Similarly the broad peaks at 1325 nm and 1600 nm in the HiPCO-SDBS derive from the solvent. Both dispersions show a broad background, which is common in nanotubes dispersions and can be attributed to particulates

generated during the sonication, carbonaceous impurities, and the presence of metallic SWCNT.[5]

The peaks in the higher energies are to be attributed to the E_{11} transitions of metallic tubes, followed by the E_{22} of semiconducting tubes and E_{11} again of semiconducting tubes, as marked by the arrows on the graph. The sharpness of the peaks deteriorates in the NIR-IR region, as many carbon nanotubes have very similar E_{22} transitions.[6]

Figure 5.2 shows the UV-VIS-NIR spectra of the solutions where the amount of SWCNT dispersed was kept constant at 0.5 mg/mL, and the amount of polymer concentration was varied.

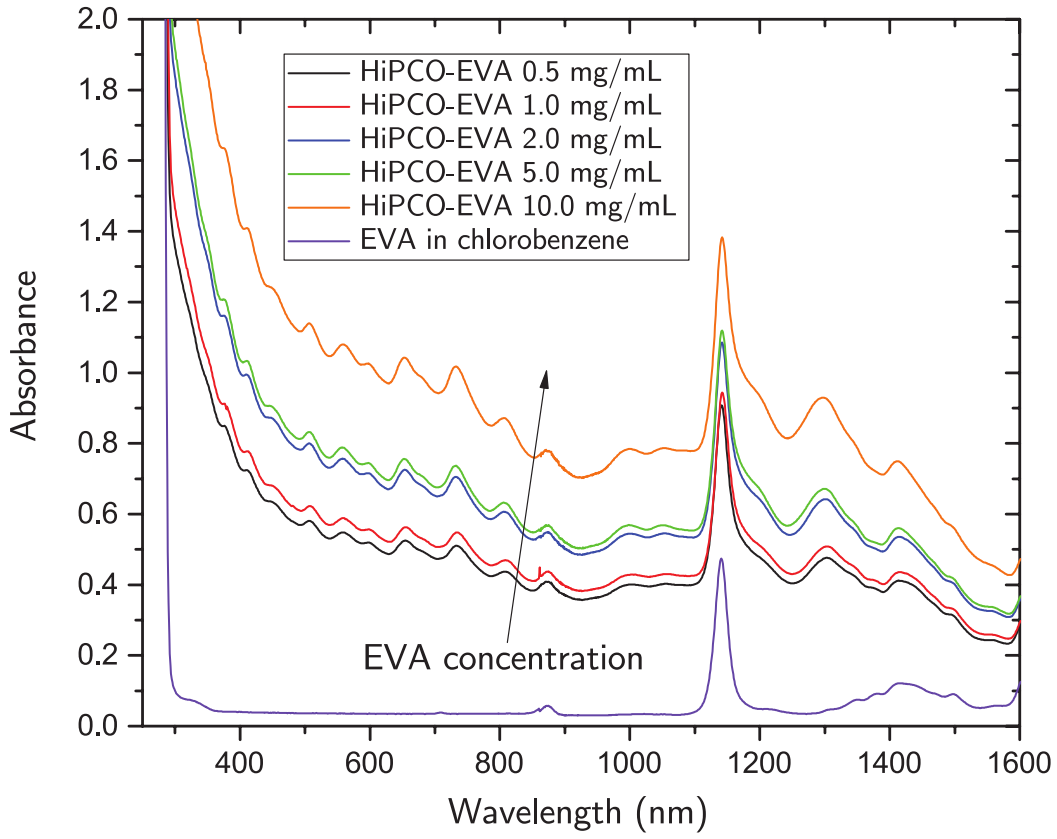

Figure 5.2: Comparison of the absorption spectra of HiPCO-EVA dispersion in chlorobenzene with different EVA concentrations, with the HiPCO initial concentration kept constant at 0.5 mg/mL. As a reference, the absorption of neat EVA in chlorobenzene (purple solid line) is also shown. The comparison shows an increased absorption for higher polyemer concentrations. The arrow marks the direction of increasing EVA concentration.

It can be seen that the increase of the dissolved polymer corresponds to a higher

absorbance of the dispersion, indicating a larger amount of nanotubes solubilised. This is also confirmed by the observed amount of precipitate after the centrifugation, which was higher in case of lower polymer concentrations, indicating that a smaller amount of carbon nanotubes were retained in the supernatant.

There is no observable change in the number of peaks or relative intensities, so the polymer concentration can be attributed to a more effective solubilization uniformly distributed across all the nanotubes, likely due to a better chance of the polymer to wrap carbon nanotubes every time a cluster is broken during the sonication process. The spectral congestion makes difficult to assign peaks to individual SWCNT chiralities.

5.3 Excess polymer removal

The solutions prepared according to the EVA-CNT nanohybrids went through an excess polymer removal process resembling the method developed by Schuettfort *et al.*[7]

Removing the excess polymer is an essential step for many device applications, as it allows the fabrication of films with good electronic qualities, as it will be shown in the following chapters.

The procedure is illustrated in the diagram in Figure 5.3. The first two steps are described in the previous section, with the carbon nanotubes being mixed in the polymer solution with an ultrasonic probe and centrifuged to collect only the solubilised tubes.

20 mL of toluene are then added to the supernatant, and the solution is put on a hotplate at 80°C for 1h. The solubility of carbon nanotubes in toluene is low,[1] so they aggregate while the polymer stays in solution, as it can be seen in Figure 5.4. This process is commonly performed with semiconducting polymers, and this is the first successful experiment where the purification is obtained with a non-conjugated polymer.

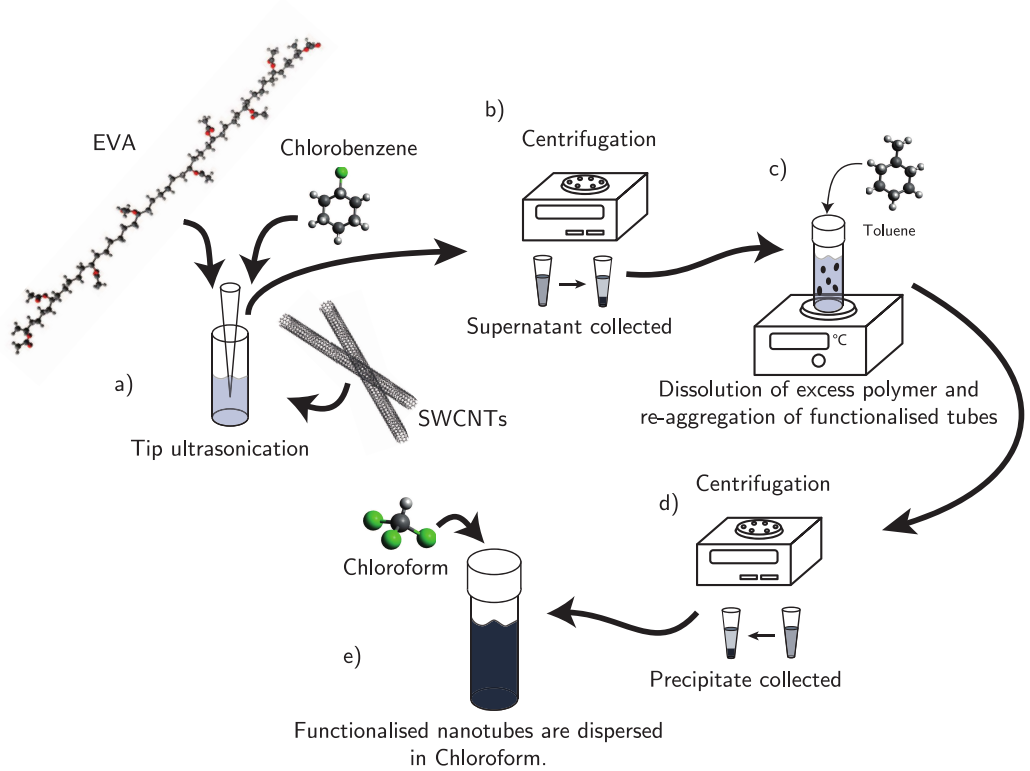

Figure 5.3: Diagram illustrating the preparation process of the HiPCO-EVA nanohybrids. a) The CNTs are sonicated in a solution of EVA dissolved in chlorobenzene. b) the solution is centrifuged to remove unsolubilised CNT. d) Toluene is added and the solution is put on a hotplate to induce the aggregation of the nanohybrids. d) The solution is centrifuged, and the precipitate collected. e) The pellets, containing the nanohybrids, are dispersed in chloroform.

Figure 5.4: Excess polymer removal process of EVA-CNT nanohybrids. Vials in the left picture show solutions immediately after the first centrifugation, and in the right picture after toluene has been added. The first bigger vial in each photo contains neat EVA dissolved in chlorobenzene. The smaller vials in each picture contain the HiPCO tubes solubilised in (from left to right) 2.0 mg/mL, 1.0 mg/mL, 0.5 mg/mL, 0.2 mg/mL. 0.1 mg/mL, 0.01 mg/mL EVA in chlorobenzene.

The aggregation is a first indication of the presence of a very thin layer of polymer wrapping the carbon nanotube, as it is enough to screen the Wan Der Waals forces causing aggregation[8] in good solvents like chlorobenzene,[9] but it still causes aggregation when a solvent such as Toluene for which CNT have lower solubility is used.[9] Further investigations on this will be presented in the following sections.

The polymer excess removal step was not successful in samples with 5.0 mg/mL and 10.0 mg/mL of EVA, as no aggregation is observed. A possible explanation is given by the high the polymer:solvent ratio, which might be high enough to screen the aggregation of the nanotubes even when toluene is added. Figure 5.4 shows the solutions before and after the addition of toluene for EVA concentrations of 2.0, 1.0, 0.5, 0.2, 0.1 and 0.01 mg/mL. In both figures, there is a larger vial with EVA in chlorobenzene with no carbon nanotubes to compare the colour of the solutions.

After the aggregation, the solution is centrifuged again at 16,000 g for 4 min, and the supernatant, containing the excess polymer, is discarded. Vials with 0.1 mg/mL and 0.01 mg/mL produced a very low amount of precipitate, which did not allow further measurements.

The precipitate consists of ∼50 mg to ∼250 mg of aggregated polymer-wrapped CNTs depending on the starting ratio of CNT:polymer:solvent. As this amount varies by changing the starting amount of CNTs, solvent and polymer, but it consistently

constant as long as the starting concentrations are the same, in the following sections the total amount of precipitate from a single batch will be referred to as "pellet".

After the centrifugation, the pellet is dissolved in chloroform, in a volume varying from 5 to 50 mL depending on the experiment.

Chloroform is chosen for its very low boiling point (61°C[10]), which will enable an easier deposition for the experiments of the following chapters.

The pellets solubilise immediately upon agitation of the solution, and to remove any residual aggregate the solution is sonicated at about 10% of the power used in the first step ($\sim 40W$). The resulting solution is homogeneous by eye, and no aggregation is observable even after months from the preparation.

5.4 Solubilisation of MWCNTs with EVA

The majority of the literature regarding the individual solubilisation of carbon nanotubes focuses on SWCNT. This is mainly due to the extreme interest in using SWCNT for electronic devices such as transistors, where a selection of semiconducting-only tubes is necessary and achievable by wrapping with conjugated polymers. There are no reported works of conjugated polymers normally used with SWCNTs successfully solubilising MWCNTs. One possible explanation is the stiffness of the polymer backbone, that in conjunction with the alkyl chains limits the coverage of the nanotube surface, which is larger in the case of MWCNTs.

The reports in the literature involving wrapping of MWCNTs do not normally discuss purification processes to remove the unbound polymers.[11]

Remarkably, the solubilisation and purification process using EVA described in the previous sections has been successful with MWCNTs.

Samples have been prepared according to sections 5.2 and 5.3, using an EVA polymer concentration of 0.5 mg/mL and 1 mg of Nanocyl MWCNT instead of 5 mg HiPCO tubes. Figure 5.5 shows the UV-VIS-NIR absorption spectra of EVA-MWCNT nanotubes in chloroform and the spectrum of neat EVA in chloroform for reference.

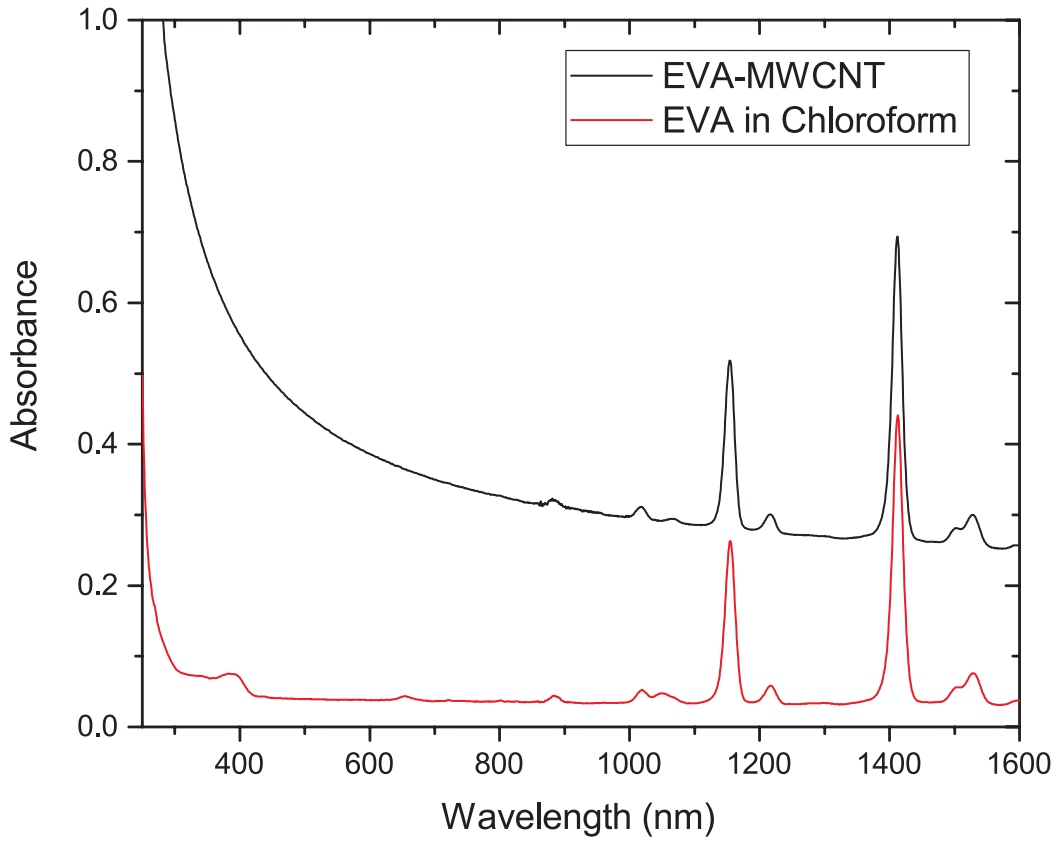

Figure 5.5: Absorption spectrum of a MWCNT-EVA dispersion in chloroform (solid black line). As a reference, neat EVA in chloroform is shown (solid red line). The spectrum shows a continuous absorption (with the exception of the peaks caused by the solvent), without any Van Hove singularity.

Differently from the SWCNT, there is no evidence of sharp peaks which is not attributable to the solvent, and the MWCNT show a continuous absorption without Van Hove peaks increasing as the radiation energy increases. This is due to the multiple shells composing each tube, offering a continuum of available states.

Due to this characteristic, no further optical investigations have been carried out on EVA-MWCNT. AFM measurements of individual tubes and the electrical properties of films will be shown in the following sections.

5.5 Photoluminescence excitation spectroscopy

PLE spectroscopy is a powerful tool to study the semiconducting population of nanotubes. Due to the very sharp DOS of carbon nanotubes, each absorption-emission duple uniquely identifies a single chirality SWCNT.

It only allows to detect semiconducting nanotubes, as excitations in metallic nanotubes decay non-radiatively due to the absence of a band gap.[12] Moreover, the presence of a photoluminescence signal indicates the individualisation of carbon nanotubes, since in a cluster of semiconducting and metallic tubes, the charge is transferred to the metallic tubes and decays again non-radiatively.

The maps of Figure 5.6 show the PLE map of HiPCO tubes dispersed in Chloroform-EVA (with excess polymer removed) and, for comparison, in D_2O-SDBS. The maps were taken with the help of Markus Dollmann (Department of Physics, University of Oxford).

The species were assigned using the Weisman and Bachilo empirical table,[6] based on a dispersion of HiPCO in water using SDS as a surfactant.

The species result homogeneously distributed in the SDBS-dispersed sample, with a slight predominance of (7,6), (9,4), (8,6).

The EVA-HiPCO in chloroform show well resolved peaks, a sign of a good separation of individual tubes due to the polymer. The sample is moderately more emissive than the SDBS, suggesting a lower presence of metallic tubes, or low presence of bundles

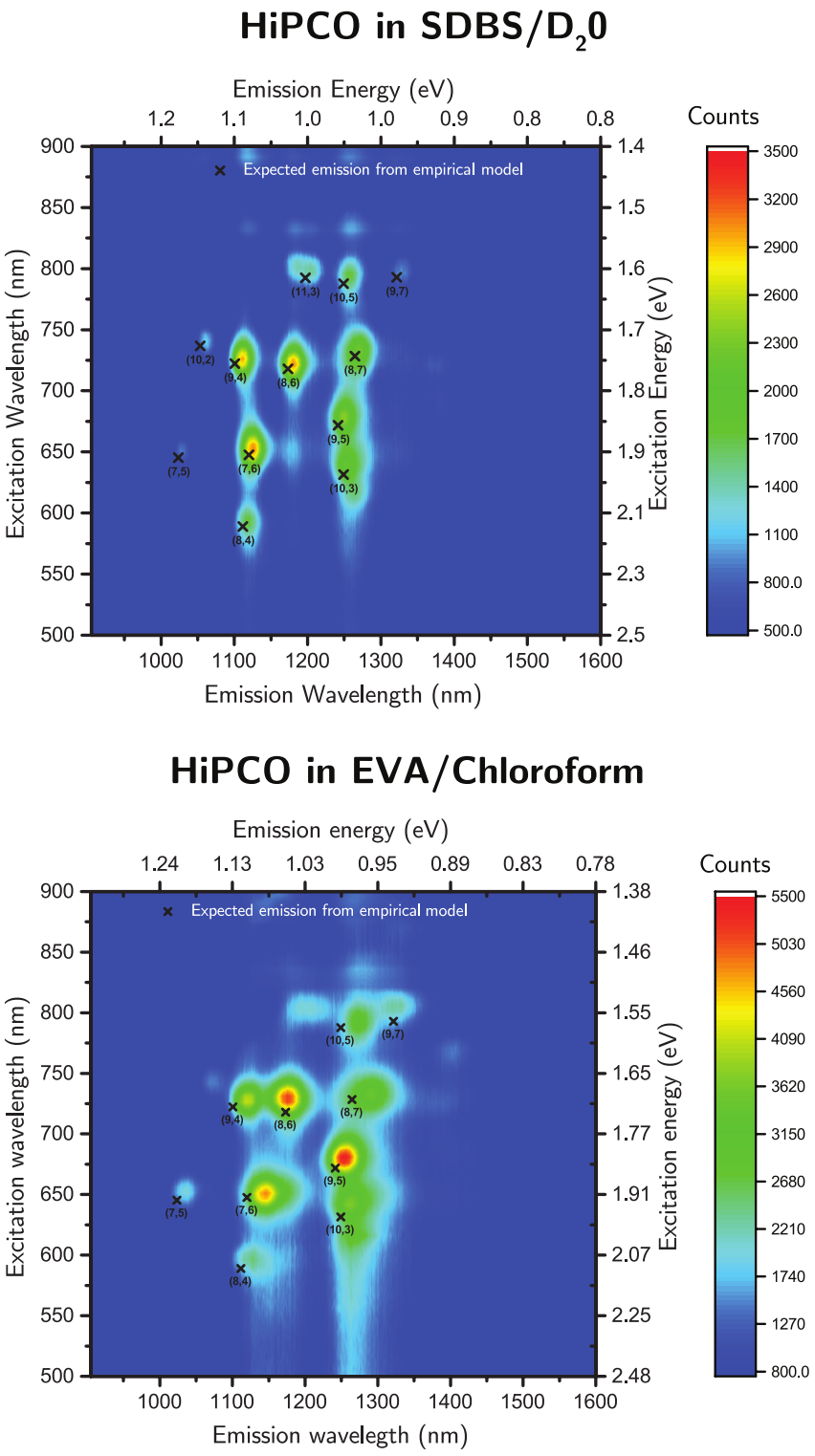

Figure 5.6: Photoluminescence excitation maps of SDBS-HiPCO (top) and EVA-HiPCO with excess polymer removed (bottom). Black crosses mark the expected emission for each chirality as reported by Weisman and Bachilo[6]. Maps show well resolved peaks, with a differences in peaks predominance between the two samples. Adapted with permission from reference [13]. Copyright 2019 American Chemical Society.

with metallic tubes, as they would quench the photoemission. The distribution of species shows changes compared to the control sample of SDBS-HiPCO, being now dominated by (9,5) and (8,6) tubes, followed by (7,6) and (9,4), and finally (10,3), (10,5), (9,7), (8,4) and (7,5). Despite some emission is visible where the (11,3) peak is expected, the peak profile is extremely broad and it is not possible to assign a position.

Peaks are slightly red-shifted compared to the expected emission. In the SDBS-HiPCO sample the shift is $\sim$10 meV, due to the slightly different dielectric screening of SDBS compared to SDS, which was used by Weisman and Bachilo to build the table.[6] The EVA-HiPCO sample has a more pronounced shift. This is in part to be attributed again to a different dielectric screening of the wrapping molecule and the different solvents, but also to the mechanical stress induced by the wrapping molecule, as it will be discussed in the next section.

In summary, the photo-luminescence excitation map suggests that the EVA is wrapping and solubilising individual tubes. The change in the relative intensity of the peaks shows a slight preference in wrapping specific chiralities, although the solubilisation is not completely selective. This suggests that EVA is unable to isolate single chiralities, but has the advantage of solubilising much higher concentrations of SWCNTs compared to selective polymers such as PFO and also solubilise MWCNTs.

5.6 Bond-induced stress

The shift observed in the absorption and emission for each tube in Figure 5.6 appears less consistent in samples solubilised with EVA.

This is because in addition to the different dielectric environment, a shift in energy can also be caused by a mechanical deformation of the nanotubes.

A shift caused by a mechanical strain would be an additional proof of the strong binding between the polymer and the carbon nanotubes. This is evaluated here by

analysing the peak displacements using a similar method to the one showed by Stranks *et al.*[14]

As described in chapter 2, all the optoelectronic properties of SWCNTs are strictly related to their geometry. It appears then natural that a mechanical stress inducing a geometrical deformation will affect the absorption and emission properties. The effect of strain on the electronic properties of SWCNT was first derived by Yang *et al.*[15]

This is represented in Figure 5.7. As shown in chapter 2, in an unmodified graphene lattice the Brillouin zone will be a hexagon and the Fermi point $\mathbf{k}_F$ will sit on the hexagon vertices. A strain will modify the hexagonal lattice, and as a consequence the position of the Fermi point $\Delta\mathbf{k}_F$, reaching the new position $\mathbf{k}'_F$.

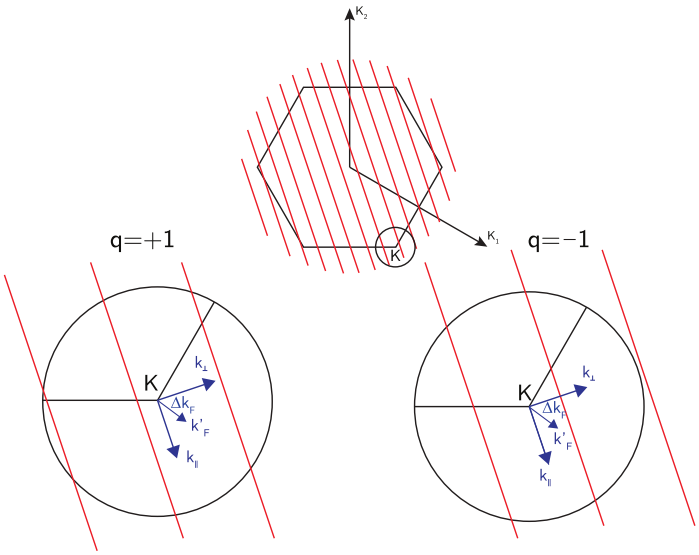

Figure 5.7: Brillouin zone of graphene and effect of the mechanical stress on the position of the Fermi point. The two circles show the different effect of a mechanical strain in different tubes. When q=+1, the mechanical strain shifts the fermi point to the new position $\mathbf{k}'_F$ further away from one of the allowed momenta. When q=-1, the new position $\mathbf{k}'_F$ is closer.

Depending on the classification parameter q of the carbon nanotube (see Eq. 2.22), the new position $\mathbf{k}'_F$ will be closer to one of the allowed momenta for q=+1, and further away for q=-1. It is then possible to recalculate the DOS using the same approximation shown in chapter 2 (see Eq. 2.26), and the new values for energy are given by

$$E_i = \frac{\sqrt{3}}{2} a_0 \gamma_0 \Delta k'_\perp,\ \Delta k'_\perp = |(3i - q) - \Delta k_{\perp,F}| \tag{5.1}$$

with the quantised component being[15]

$$\Delta k_{\perp,F} = \frac{\sqrt{3}}{a_0} \left[(1+\nu)\epsilon_\parallel \cos 3\theta + \epsilon_\perp \sin 3\theta \right] \tag{5.2}$$

where ν is the is the Young's modulus of the nanotube, θ is the chiral angle, a_0 the lattice constant and $\epsilon_\perp$ and $\epsilon_\parallel$ are the strains along the tube axis and circumference respectively.

The variation of the bandgap then becomes

$$\Delta E_{ii} = -\frac{4\gamma_0 a_0 i}{\sqrt{3}d}(\epsilon_\perp - \nu\epsilon_\parallel) + 3(-1)^{q+1}(-1)^{i+1}\gamma_0[(1+\nu)\epsilon_\parallel \cos 3\theta + \epsilon_\perp \sin 3\theta] \tag{5.3}$$

It is clear from the second term that the change in the bandgap changes depends on the q value. Specifically, the E_{11} transition increases in tubes having q=+1 and decreases when q=-1, while the E_{22} transition decreases when q=+1 and increases when q=-1. Differently from the screening caused by the different dielectric environment then, the mechanical strain will produce different shifts for different tubes.

The observed shift in the PLE maps is then given by

$$\Delta E_{ii} = \Delta E_{\text{environment}} + \Delta E_{\text{strain}} \tag{5.4}$$

The first term of the sum will have the same magnitude and sign for both absorption and emission, while the second term will be described by Eq. 5.3 and depends on the q value.

Since $\Delta E_{\text{environment}}$ has the same value for the absorption and the emission, it can be taken as the mean value

$$\Delta E_{\text{environment}} = \frac{\Delta E_{11} + \Delta E_{22}}{2} \tag{5.5}$$

so the ΔE_{strain} will be

$$\Delta E_{\text{strain}} = \frac{\Delta E_{11} - \Delta E_{22}}{2} \tag{5.6}$$

so considering Eq. 5.3 it becomes

$$\Delta E_{\text{strain}} = \frac{\Delta E_{11} - \Delta E_{22}}{2} = \frac{2\gamma_0 a_0}{d}(\epsilon_\perp - \nu\epsilon_\parallel) + 3q\gamma_0[(1+\nu)\epsilon_\parallel \cos 3\theta + \epsilon_\perp \sin 3\theta] \tag{5.7}$$

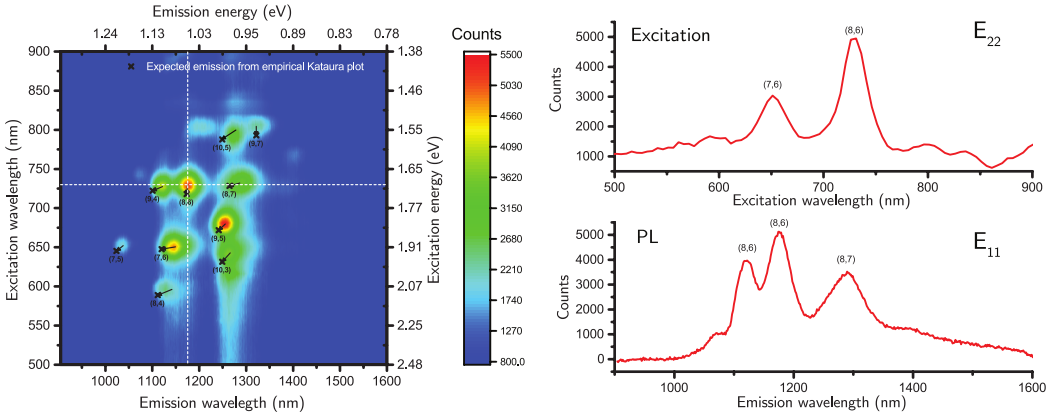

Figure 5.8: PL and absorption profiles for the (8,6) peak in a EVA-HiPCO sample. The two plots on the right show the profiles of the (8,6) peak, obtained slicing the graph on the vertical (absorption) and horizontal (PL) white dashed line on the PLE map. The peak has been fitted with a gaussian function to determine the position, and the procedure repeated for all the peaks. Adapted with permission from reference [13]. Copyright 2019 American Chemical Society.

Figure 5.8 highlights with black arrows the energy shift of the photoluminescence peaks from the Weisman and Bachilo empirical model,[6] where it can be clearly seen a different shift for different tubes.

The graphs on the right show the sections marked with the white dashed lines, and represent the emission and absorption peak for the (8,6) tube. These have been fitted with Gaussian functions to determine the peak position, and the error on the localisation has been taken as 1/10th of the FWHM.

Chirality	Emission peak (meV)	FWHM emission (meV)	Absorption peak (meV)	FWHM absorption (meV)
(7,5)	1195	54	1901	76
(7,6)	1079	47	1906	71
(8,4)	1086	96	2079	109
(8,6)	1055	49	1701	53
(8,7)	0963	57	1694	84
(9,4)	1106	54	1704	48
(9,5)	0987	34	1824	75
(9,7)	0938	52	1541	45
(10,3)	0980	46	1929	56
(10,5)	0972	49	1565	60

Table 5.1: Photoluminescence peaks position of a EVA-HiPCO dispersion. Values have been obtained by fitting a Gaussian function on the PLE maxima.

The same has been repeated for all the peaks and the values of ΔE_{11} and ΔE_{22} calculated.

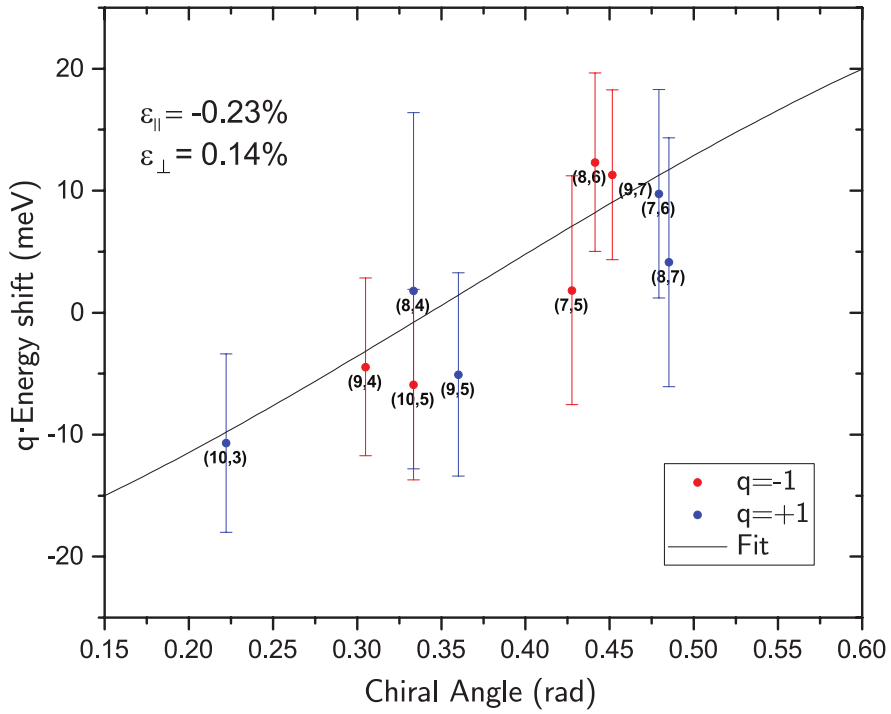

Figure 5.9: Energy shift caused by mechanical strain on the tube as a function of the chiral angle θ. Values have been multiplied by the parameter q to better show the trend given by the model of equation 5.7. The solid line shows the expected energy shift for tubes with longitudinal strain $\epsilon_{\parallel} = -0.23\%$ and perpendicular strain $\epsilon_{\perp} = -0.14\%$. Adapted with permission from reference [13]. Copyright 2019 American Chemical Society.

Figure 5.9 shows the resulting values plotted against the chiral angle. The first term of the sum of Eq. 5.7 is negligible, so the function has an inverse slope for opposite q values. For ease of visualization, the energy shifts in Figure 5.9 have been multiplied by their q value to have the same slope.

The black line represents Eq. 5.7 with $\epsilon_{\parallel} = -0.23 \pm 0.06\%$ and $\epsilon_{\perp} = -0.14 \pm 0.04\%$, which are the optimum values found with a Levenberg-Marquardt algorithm, using $\gamma_0 = 3.0$ eV, $a_{C-C} = 0.144$ Å, and $\mu = 0.20$.

Despite the relatively large errors, the energy shifts clearly show a trend predicted well by the model. It is then not possible to quantify exactly the strain induced on the tubes, but data allow to clearly state that the polymer is inducing a deformation on the tube, suggesting then a strong interaction between the polymer and the CNTs.

5.7 Raman spectroscopy

Raman spectroscopy is a powerful tool to study the chirality distribution of SWCNTs as each tube has a different radial breathing mode (see section 2.2). Differently from PLE, which only enables to study the semiconducting tubes,[12] Raman signal in CNTs is still present regardless of the metallic/semiconducting distribution in the sample.

Assigning peaks to different SWCNTs is less trivial than PLE.[16] While PLE offers a 2D map of the peaks position, with Raman spectroscopy there is a much higher spectral congestion, as different tubes can have a very similar diameter, thus a similar radial breathing mode.

In order to assign peaks, considerations have to be made on the excitation radiation. As illustrated in section 2.2, the Raman signal is much enhanced when the excitation is close to an E_{ii} transition. A useful tool for this task is the Kataura plot,[17] shown in Figure 5.10. This displays the expected transitions for every SWCNT against the tube diameter. In Figure 5.10 it has been redrawn against the expected radial breathing mode wavenumber (which is proportional to 1/d), according to the data calculated by Maultzsche *et al.*[16]

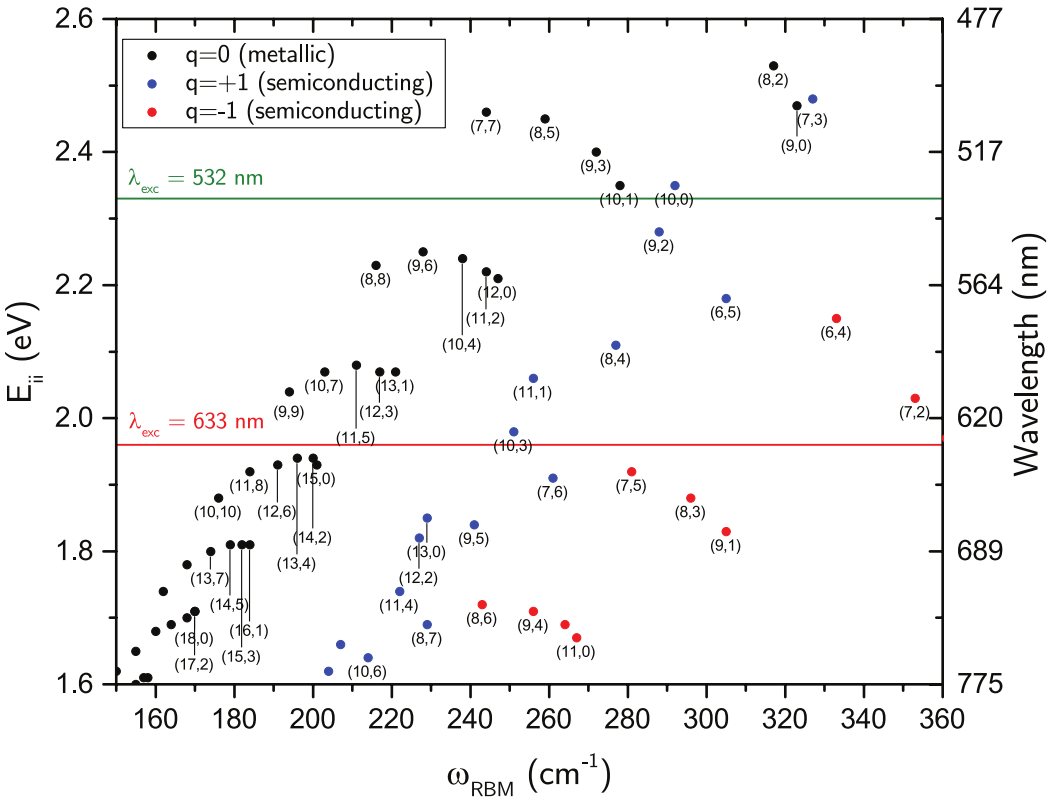

Figure 5.10: Empirical Kataura plot, data from reference [16]. The black dots show the resonance transitions of metallic nanotubes, the blue and red dots of semiconducting nanotubes, having q=+1 and q=-1 respectively. The energy of the excitations lasers used in the experiments is marked with the green and red horizontal lines, respectively for the Nd:YAG laser (532 nm) and the He:Ne laser (633 nm). SWCNT tubes having transitions close to the laser lines, will show a much enhanced Raman signal when excited with that laser.

In the graph the excitation energy used for these experiments has been highlighted with two horizontal lines; a solid red line for the 633 nm laser (1.96 eV) and a solid green light for the 532 nm laser (2.33 eV). SWCNTs having transitions close to these lines will show a large Raman signal when excited with the corresponding laser.

As it can be seen from the Kataura plot of Figure 5.10, the green laser allows the detection of metallic SWCNTs with ω_{RBM} <270 cm^{-1} and semiconducting tubes with ω_{RBM} >270 cm^{-1}, while the red laser is close to the resonance of many semiconducting tubes with 250 cm^{-1} < ω_{RBM} <360 cm^{-1} and of metallic tubes with ω_{RBM} <250 cm^{-1}.

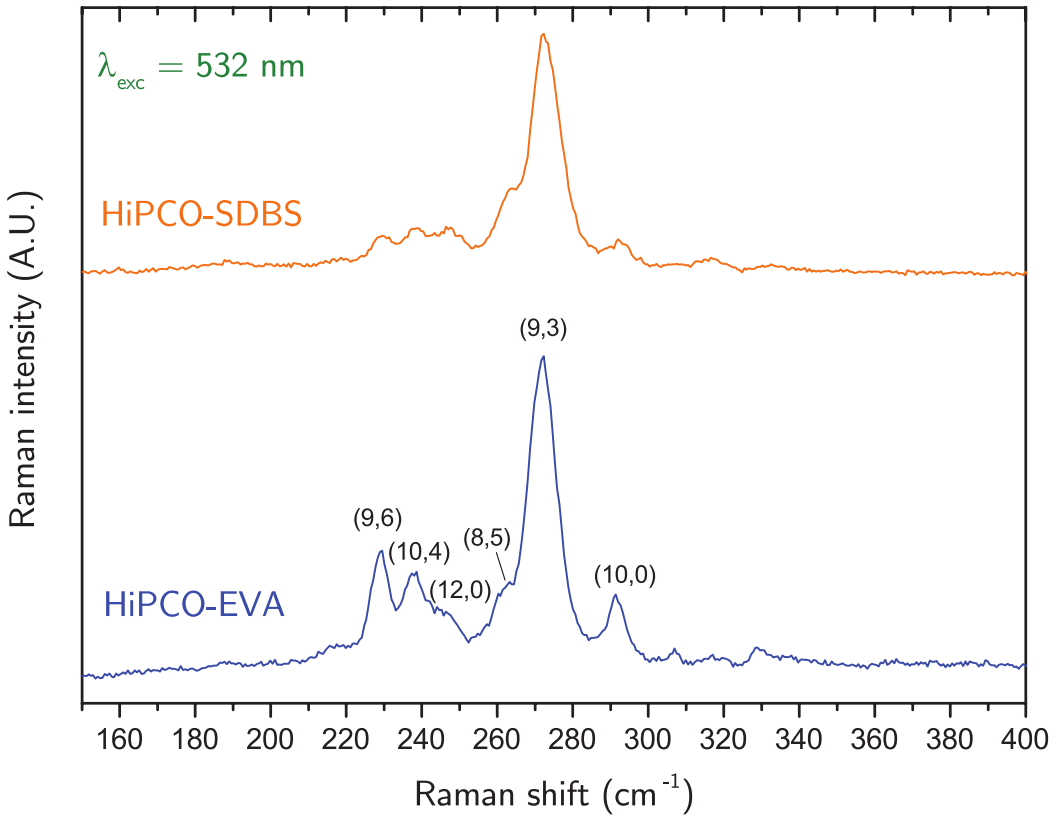

Figure 5.11: Raman spectrum of HiPCO-SDBS (solid orange line) and HiPCO-EVA (solid blue line) obtained with a 532 nm excitation laser. The region analysed corresponds to the RBM of SWCNTs. The spectra suggest a large number of metallic SWCNT, and the relative peaks height change when SDBS or EVA is used to solubilise the tubes. Adapted with permission from reference [13]. Copyright 2019 American Chemical Society.

Being dependent on the distance between the excitation and the energy of the transition, these Raman measurements cannot be used to asses quantitatively the

presence of each chirality. However, it is a powerful tool to asses relative changes in the composition with respect to a reference sample, which in this case has been again made of SDBS-solubilised HiPCO nanotubes.

Samples for this study were prepared by drop-casting the solutions prepared according to section 5.2 on a Silicon/Silicon dioxide substrate and let them dry in ambient conditions.

Figure 5.11 shows the comparison of EVA-HiPCO and SDBS-HiPCO when a 532 nm laser is used to excite the sample. It can be seen immediately that numerous metallic tubes are detected [(9,6),(10,4),(12,0),(8,5),(9,3)], and the (10,0) chirality is the only semiconducting species detected. The relative peaks height suggest a change in the composition between the EVA-HiPCO and SDBS-HiPCO, with a more predominant presence of (9,6), (10,4) and (12,0) tubes compared to (9,3) tubes. This suggests a preference for the polymer to solubilise specific metallic chiralities.

Figure 5.12 compares the Raman emission of the same samples studied in Figure 5.11 when excited with a 633 nm laser radiation. There are 6 semiconducting species detected [(11,4), (10,3), (11,1), (7,6), (7,5), (8,3)] and a single metallic chirality (13,1). It is again possible to observe a difference in the relative height of the peaks. Interestingly, the peaks corresponding to (10,3),(11,1),(7,6) chiralities merge into a single peak in the SDBS-HiPCO sample, suggesting a better physical separation of tubes when solubilised with EVA.

In summary, Raman measurements confirm the conclusions outlined by the PLE experiments. Peaks from the EVA-HiPCO samples are again well resolved, sometimes better resolved than SDBS-HiPCO tubes, suggesting again an individual wrapping of the tubes. The presence of numerous metallic tubes confirms the non-selectivity of the polymer, which appears to wrap indistinctly metallic and semiconducting polymers.

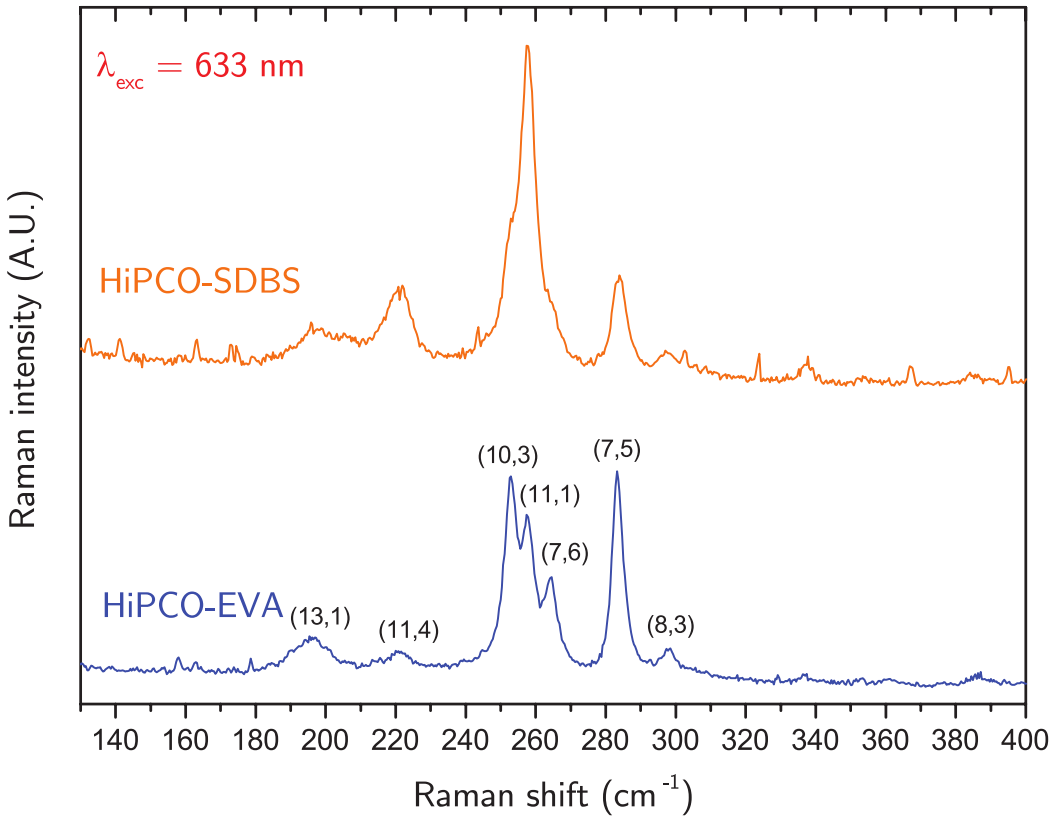

Figure 5.12: Raman spectrum of HiPCO-SDBS (solid orange line) and HiPCO-EVA (solid blue line) obtained with a 633 nm excitation laser. The region analysed corresponds to the RBM of SWCNTs. The spectra show a different relative heights between peaks, and the (10,3),(11,1),(7,6) peaks merge into a single peak in the HiPCO-SDBS sample. Adapted with permission from reference [13]. Copyright 2019 American Chemical Society.

5.8 Atomic force microscopy

To study the morphology of the nanohybrids, AFM images of individual tubes were taken. Samples were prepared by spin-coating a very diluted solution of CNT-EVA at high-speed. The solutions were prepared as described in sections 5.2 and 5.3, but the final pellets have been dispersed in 50 mL of chloroform. This solution was further diluted to a 1:5 v/v ratio and deposited on glass substrate by spin-coating at 5000 rpm, and AFM maps of the samples obtained.

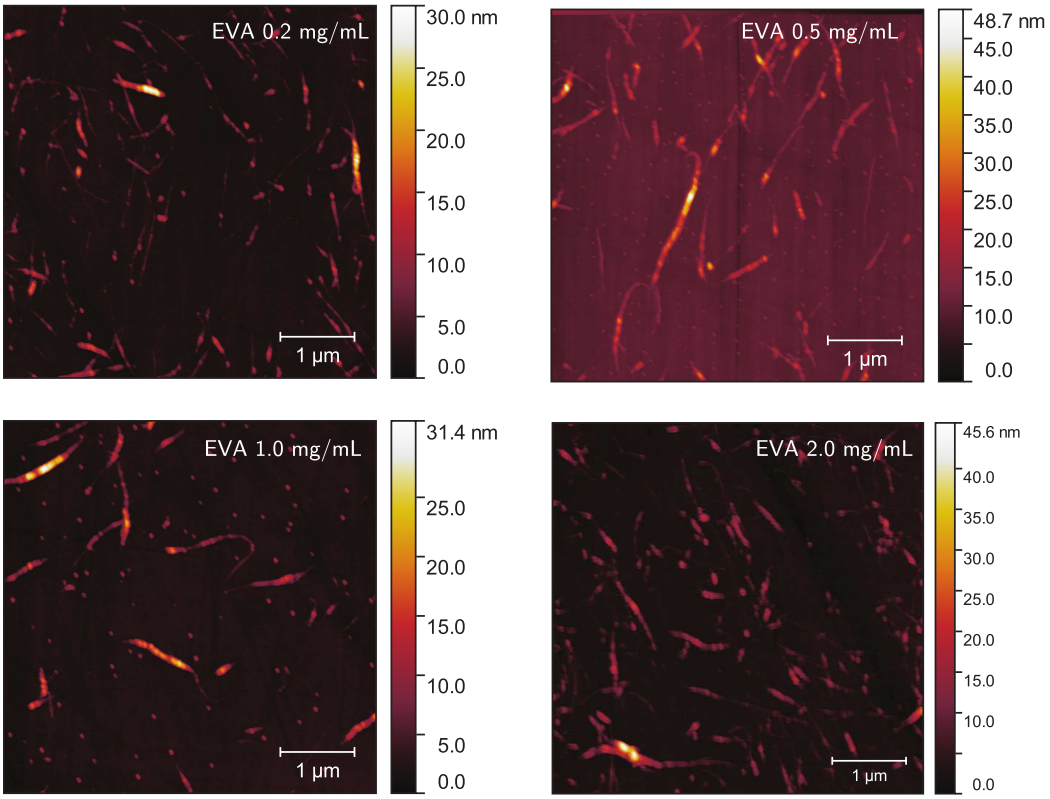

Figure 5.13: AFM maps of EVA-HiPCO nanohybrids on glass prepared with different initial polymer concentrations: 0.2 mg/mL, 0.5 mg/mL, 1.0 mg/mL, and 2.0 mg/mL. The maps show individual tubes, with little difference in the morphology when different concentrations are used. Adapted with permission from reference [13]. Copyright 2019 American Chemical Society.

Figure 5.13 compares the film of EVA-HiPCO tubes prepared using 4 different initial concentrations of EVA: 0.2 mg/mL, 0.5 mg/mL, 1.0 mg/mL, and 2.0 mg/mL. All the images show a very similar morphology, suggesting that a very thin layer of polymer binds to the CNT and the remaining polymer is removed by the purification

process. Nevertheless, the sample made with 0.2 mg/mL appears to have thinner CNTs, than the remaining samples, likely indication of a non-self-limiting process, whit thicker coatings in case of an abundance of the polymer.

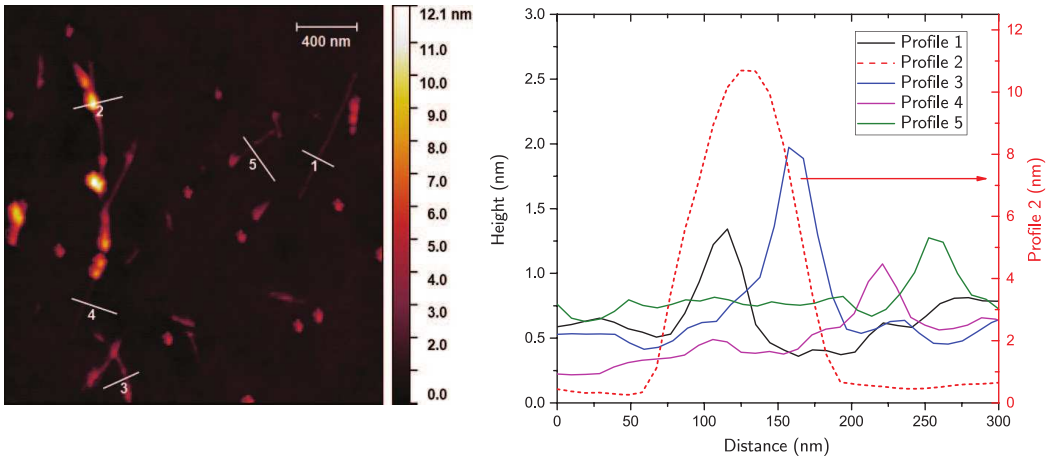

Figure 5.14: AFM map of EVA-HiPCO nanohybrids on glass (left) and height profiles of single tubes (right). The paths of the profiles in the right plot are marked by the white segment on the AFM map. The red, dashed profile is plotted on a different scale, shown on the right axis. Adapted with permission from reference [13]. Copyright 2019 American Chemical Society.

To better understand the morphology of the single SWCNTs, Figure 5.14 shows the AFM map of a sample prepared with a 0.5 mg/mL EVA starting concentration on a closer scale. The white lines mark the paths of the profiles reported in the plot on the right. The profile lines show numerous regions on the SWCNT with a height of 1 to 2 nm, suggesting a thin polymer coating of one or two layers around a single nanotube. Other regions show a thicker profile of up to 10-11 nm (Profile 2), probably due to some bundled tubes or a thicker polymer coating, the latter suggesting again that the polymer-wrapping is a non-self-limiting process.

The MWCNT sample (Figure 5.15) show again a very thin height profile (5-7 nm in the thinnest regions, up to 25 nm in the thickest), also suggesting single or small bundle solubilisation. It is worth noting that despite the AFM studies showing the possibility of nanotube bundles in the films, the very well-defined peaks in the PLE maps suggest a very limited bundling of tubes in the SWCNT dispersion, since bigger bundles of tubes would broaden and completely quench the PL emission, especially considering the presence of metallic tubes revealed by the Raman measurements.

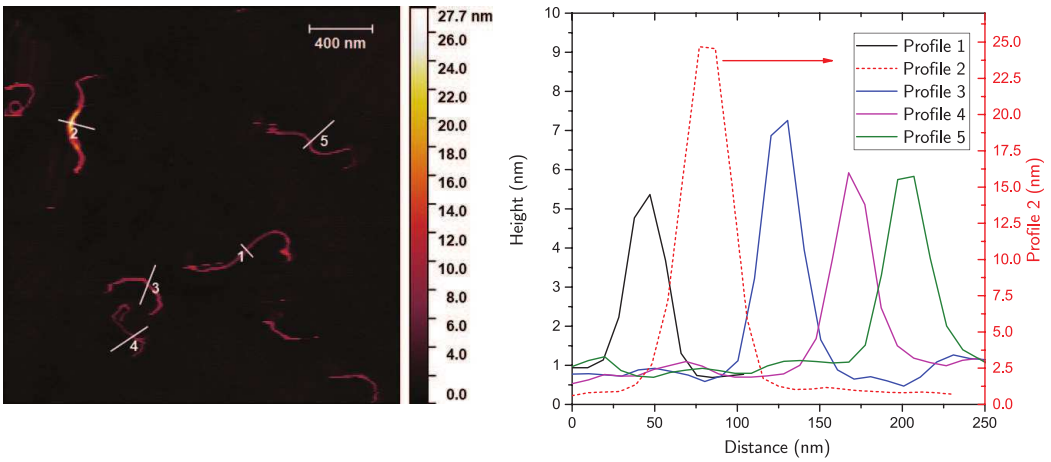

Figure 5.15: AFM map of EVA-MWCNT nanohybrids on glass (left) and height profiles of single tubes (right). The paths of the profiles in the right plot are marked by the white segment on the AFM map. The red, dashed profile is plotted on a different scale, shown on the right axis. Adapted with permission from reference [13]. Copyright 2019 American Chemical Society.

In conclusion, AFM maps show individual or small bundles of CNT, confirming the effective individual solubilisation of the nanotubes. There is no obvious difference in the morphology when different starting polymer concentrations are used, although the use lower concentration shows a larger number of thinner nanohybrids. The profiles suggest a very thin polymer coating, with some regions with a larger accumulation.

5.9 Conclusions

This chapter showed how EVA, a common non-conjugated polymer, is able to individually solubilise SWCNT and MWCNT, making it possible to easily process them.

Using solvent engineering, it is possible to purify the solutions from the excess, non-bound polymer, to obtain a dispersion containing only carbon nanotubes covered with polymer.

The photoluminescence measurements showed the presence of well-resolved peaks, excluding the presence of big bundles, as photoluminescence would be quenched by metallic SWCNT in this scenario.

Raman spectroscopy revealed the presence of numerous metallic SWCNTs, showing the non-selectivity of this solubilisation process, however the results still suggests a

preference for the polymer to wrap metallic chiralities. The presence of well-defined peaks re-confirms the conclusions drawn from the PLE measurements.

AFM maps allowed to study the morphology of the nano-hybrids revealing the presence of individual or small clusters of tubes. The starting polymer concentration does not appear to have a significant effect on the morphology. The profiles analysis on individual SWCNTs and MWCNTs suggests again a very thin polymer coating on each tube, indicating that only the polymer that is strongly bound to the CNT does not get removed by the purification process.

The absence of π orbitals in the EVA polymer excludes the wrapping mechanism claimed by conjugate-polymers commonly used in organic electronics. The presence of numerous CH-groups, however, could explain the strong binding inferred from the PL shift, as CH-π interactions have been shown to be the driving mechanism for binding between non-conjugated polymers and nanotubes.[18] Despite being much weaker than the π-π interaction, the high number of -CH groups in the EVA polymer could provide sufficient binding force. Furthermore, the low glass transition of the polymer (T_G= -43°C)[19] is indicative of a low rigidity of the polymer backbone, allowing it to easily wrap along the side wall of the nanotubes permitting numerous interactions with the -CH groups.[20]

The use of a polymer like EVA, already used in many industrial application and mass-produced, can offer a very inexpensive solution to solubilise carbon nanotubes, and with the purification process described here has a big potential for a large-scale deposition of carbon nanotubes. The polymer coating of CNT shown by the AFM measurements might be thin enough to allow charges to percolate through a network of these nano-hybrids allowing their use in electronic devices. The electronic properties and the use of these networks will be the subject of the next chapters.

Bibliography

1. J. L. Bahr, E. T. Mickelson, M. J. Bronikowski, R. E. Smalley, and J. M. Tour, "Dissolution of small diameter single-wall carbon nanotubes in organic solvents?," *Chemical Communications*, no. 2, pp. 193–194, 2001.

2. M. J. O'Connell, S. M. Bachilo, C. Huffman, V. C. Moore, M. S. Strano, E. H. Haroz, K. L. Rialon, P. Boul, W. H. Noon, C. Kittrell, J. Ma, R. H. Hauge, R. B. Weisman, and R. E. Smalley, "Band Gap Fluorescence from Individual Single-Walled Carbon Nanotubes," *Science*, vol. 297, no. 5581, pp. 593–596, 2002.

3. C. A. Hunter and J. K. M. Sanders, "The nature of $\pi - \pi$ interactions," *Journal of the American Chemical Society*, vol. 112, no. 14, pp. 5525–5534, 1990.

4. A. Nish, J.-Y. Hwang, J. Doig, and R. J. Nicholas, "Highly selective dispersion of single-walled carbon nanotubes using aromatic polymers," *Nature Nanotechnology*, vol. 2, no. 10, pp. 640–646, 2007.

5. A. V. Naumov, S. Ghosh, D. A. Tsyboulski, S. M. Bachilo, and R. B. Weisman, "Analyzing absorption backgrounds in single-walled carbon nanotube spectra," *ACS Nano*, vol. 5, no. 3, pp. 1639–1648, 2011.

6. R. B. Weisman and S. M. Bachilo, "Dependence of Optical Transition Energies on Structure for Single-Walled Carbon Nanotubes in Aqueous Suspension: An Empirical Kataura Plot," *Nano Letters*, vol. 3, no. 9, pp. 1235–1238, 2003.

7. T. Schuettfort, H. J. Snaith, A. Nish, and R. J. Nicholas, "Synthesis and spectroscopic characterization of solution processable highly ordered polythiophene–carbon nanotube nanohybrid structures," *Nanotechnology*, vol. 21, no. 2, p. 025201, 2010.

8. L. A. Girifalco, M. Hodak, and R. S. Lee, "Carbon nanotubes, buckyballs, ropes, and a universal graphitic potential," *Phys. Rev. B*, vol. 62, pp. 13104–13110, Nov 2000.

9. D. S. Kim, D. Nepal, and K. E. Geckeler, "Individualization of single-walled carbon nanotubes: Is the solvent important?," *Small*, vol. 1, no. 11, pp. 1117–1124, 2005.

10. T. Tyner and J. F. Secretary, "Chloroform," in *ACS Reagent Chemicals*, pp. 0–3, Washington, DC: American Chemical Society, 2017.

11. A. Liu, I. Honma, M. Ichihara, and H. Zhou, "Poly(acrylic acid)-wrapped multiwalled carbon nanotubes composite solubilization in water: definitive spectroscopic properties," *Nanotechnology*, vol. 17, no. 12, pp. 2845–2849, 2006.

12. S. Reich, M. Dworzak, A. Hoffmann, C. Thomsen, and M. S. Strano, "Excited-state carrier lifetime in single-walled carbon nanotubes," *Physical Review B*, vol. 71, no. 3, p. 033402, 2005.

13. G. Mazzotta, M. Dollmann, S. N. Habisreutinger, M. G. Christoforo, Z. Wang, H. J. Snaith, M. K. Riede, and R. J. Nicholas, "Solubilization of carbon nanotubes with ethylene-vinyl acetate for solution-processed conductive films and charge

extraction layers in perovskite solar cells," *ACS Applied Materials & Interfaces*, vol. 11, no. 1, pp. 1185–1191, 2019.

14. S. D. Stranks, J. K. Sprafke, H. L. Anderson, and R. J. Nicholas, "Electronic and Mechanical Modification of Single-Walled Carbon Nanotubes by Binding to Porphyrin Oligomers," *ACS Nano*, vol. 5, no. 3, pp. 2307–2315, 2011.

15. L. Yang and J. Han, "Electronic Structure of Deformed Carbon Nanotubes," *Physical Review Letters*, vol. 85, no. 1, pp. 154–157, 2000.

16. J. Maultzsch, H. Telg, S. Reich, and C. Thomsen, "Radial breathing mode of single-walled carbon nanotubes: Optical transition energies and chiral-index assignment," *Physical Review B*, vol. 72, no. 20, p. 205438, 2005.

17. H. Kataura, Y. Kumazawa, Y. Maniwa, I. Umezu, S. Suzuki, Y. Ohtsuka, and Y. Achiba, "Optical properties of single-wall carbon nanotubes," *Synthetic Metals*, vol. 103, no. 1-3, pp. 2555–2558, 1999.

18. D. Baskaran, J. W. Mays, and M. S. Bratcher, "Noncovalent and nonspecific molecular interactions of polymers with multiwalled carbon nanotubes," *Chemistry of Materials*, vol. 17, no. 13, pp. 3389–3397, 2005.

19. E. F. Cuddihy, C. D. Coulbert, R. H. Liang, A. Gupta, P. Willis, and B. Baum, "Applications of ethylene vinyl acetate as an encapsulation material for terrestrial photovoltaic modules," tech. rep., NASA Jet Propulsion Lab., California Inst. of Tech.; Pasadena, CA, United States, Pasadena, CA, 1983.

20. M. Naito, K. Nobusawa, H. Onouchi, K.-i. Yasui, A. Ikeda, M. Fujiki, and M. Nakamura, "Stiffness- and Conformation-Dependent Polymer Wrapping onto Single-Walled Carbon Nanotubes Stiffness- and Conformation-Dependent Polymer Wrapping onto Single-Walled Carbon Nanotubes," *Journal of the American Chemical Society*, no. 18, p. 16697, 2008.

CHAPTER 6

Electrical properties of EVA-CNT films

6.1 Introduction

Chapter 2 described the potential applications of CNTs networks in devices, mainly given by the interesting electronic properties of this class of materials. The difficulties in fabricating uniform films with scalable methods have been the main factor hindering the widespread use of CNT networks.

It was shown in the previous chapter that EVA offers an excellent solution to individually solubilise carbon nanotubes, producing uniform and stable dispersions. The very low-cost of EVA compared to conjugated polymers makes it a very interesting option for large-area applications. Moreover, the very low optical absorption of the EVA polymer reduces any parasitic absorption normally introduced by conjugated polymers and makes this material promising in applications where transparency is

required.

This chapter will present a study on the electrical properties of films made with EVA-CNT nanohybrids, comparing the performances of the EVA-SWCNT and the EVA-MWCNT materials, showing that despite the insulating nature of the polymer wrapping the nanotubes it is possible to obtain conducting films.

6.2 Films fabrication by spray coating

The films studied in this chapter have been deposited by spray coating, which, as explained in chapter 4, offers the ability to control the thickness of the film well and obtain high uniformity over large areas.

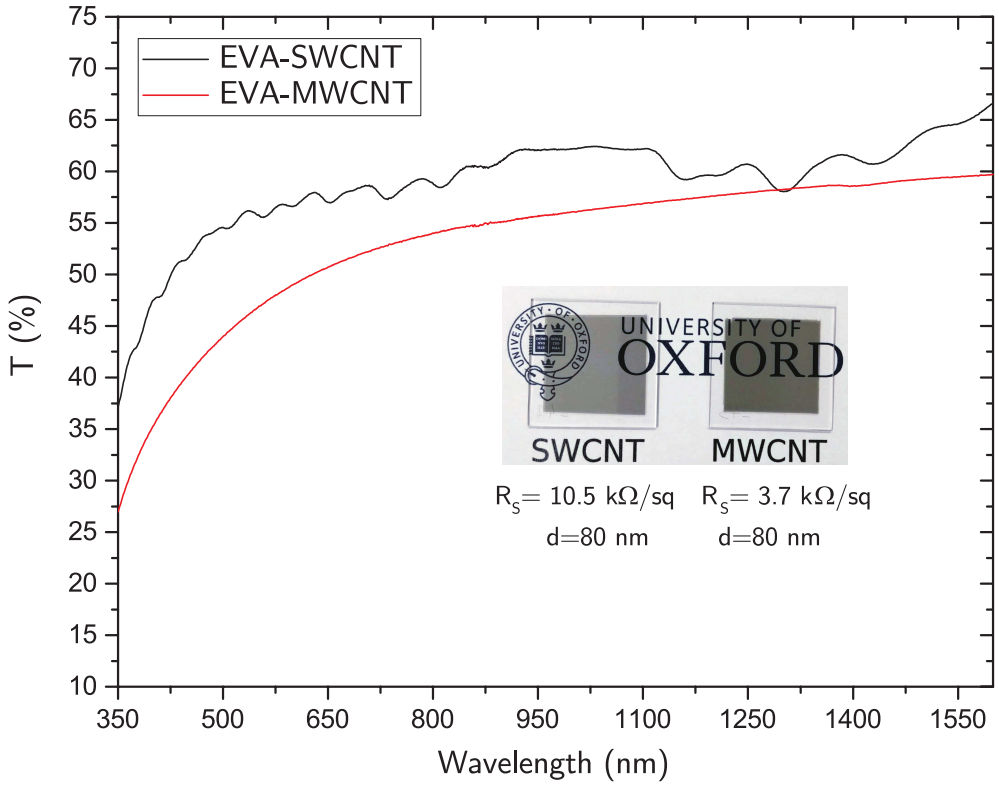

Figure 6.1: Transmittance spectrum of the sprayed EVA-SWCNT tubes and EVA-MWCNT on glass. The inset shows an image of the semi-transparent films, having a 47% transmittance at 550 nm for MWCNT and 56% for SWCNT tubes, where the losses due to the glass substrate have not been removed. The films have both a thickness of (80 ± 5) nm and an electrical conductivity of (10.5 ± 0.1) kΩ/sq and (3.7 ± 0.1) kΩ/sq respectively, corresponding to a conductivity of (11.9 ± 0.1) S/cm and (33.8 ± 0.3) S/cm. Adapted with permission from reference [1]. Copyright 2019 American Chemical Society.

Figure 6.1 shows the transmittance spectra and the images of an EVA-SWCNT film and an EVA-MWCNT film deposited on a glass substrate. Both films have been fabricated to have the same thickness (80 $\pm$ 5 nm) in order to compare their optical and electrical properties. In both spectra, the reflection losses due to the glass substrate, ($\sim$5.5%), have not been removed.

The black solid line shows the absorbance of the EVA-SWCNT film on glass. This film has a transparency between 55% and 75% in the near infrared region, dropping to values of 40-55% in the visible region due to the E_{22} and M_{11} transitions of the nanotubes, which are visible as individual absorption features from the different nanotube species present in the starting material. The sprayed film has a sheet resistance of (10.5 $\pm$ 0.1) kΩ/sq, corresponding to a conductivity of (11.9 $\pm$ 0.1) S/cm.

The red solid line shows the transmittance spectrum of a MWCNT-EVA film which shows a continuous absorption of the MWCNT, which, due to the presence of multiple shells of several diameters in each tube, does not show Van Hove singularity peaks. The 80 nm thick film has a sheet resistance of (3.7 $\pm$ 0.1) kΩ/sq, corresponding to a conductivity of (33.8 $\pm$ 0.3) S/cm, slightly larger than EVA-SWCNT.

The images in the inset of Figure 6.1 show the uniformity of the films obtained by spray-coating, which do not show any inhomogeneity.

These measurements show that despite the presence of an insulating polymer wrapping each tube, it is still possible to achieve good contact between the tubes and obtain conductive films. Higher values of conductivities can be reached with CNT, mainly through doping, chemical modification and the use of the use of ultra-long tubes,[2] however this process here offers an easy, versatile and inexpensive way to produce coatings with intermediate conductivities and transparency.

Remarkably, this is the highest values ever obtained for the combination of EVA and CNT.[3] This is achieved thanks to the purification process, in which any excess polymer is removed. This step leads to a much enhanced inter-tube contact and

better connected percolation paths, which in turn results in a conductivity increase by several orders of magnitudes compared to values found in literature.

6.3 Percolation studies in EVA-CNT films

This section is a study of the conductivity of the film as the density of the network changes from a sparse network to a thick film. Percolation theory predicts that the change of conductivity of the films depends on the density of carbon nanotubes. It predicts that in a random network of "conductive sticks", the density dependence of the conductivity is described by[4]

$$\sigma = \begin{cases} 0, & D < D_0 \\ \sigma_0 (D - D_0)^t, & D > D_0, \end{cases} \tag{6.1}$$

where σ is the conductivity of the material, σ_0 is a proportionality constant, D_0 is the critical density upon which percolation is reached, D is the density of conductive sticks and t is the critical exponent solely depending on the dimensionality of the system. For a 2D system, $t = \frac{4}{3}$[5] while for a 3D system $t = 1.9 - 2.0$.[6,7]

In these experiments, the density of nanotubes in the film is changed by increasing the concentration of EVA-CNT in the sprayed solution.

Defining the concentration in common units (e.g. g/L, %wt, *etc.*) is not possible in this case, as the process for the preparation of the solution (see Section 5.2) does not allow to determine exactly the weight of carbon nanotubes in the sprayed solution. This is due to the fact that after the first sonication it is not possible to discern the amount of polymer and carbon nanotubes discarded after each step. However, it is possible to have a relative measure of the concentration based on the starting material. The last centrifugation step in the purification process (step *d* in Figure 5.3) produces a pellet by centrifuging the solution containing the aggregated CNT, which is always the same as long as the starting quantities of materials are the same.

This pellet has been used as the unit for the amount of CNT in solution. Therefore, concentrations for this experiments are defined in number of pellets / 50 mL, as 50 mL is the typical volume used during the spray coating process.

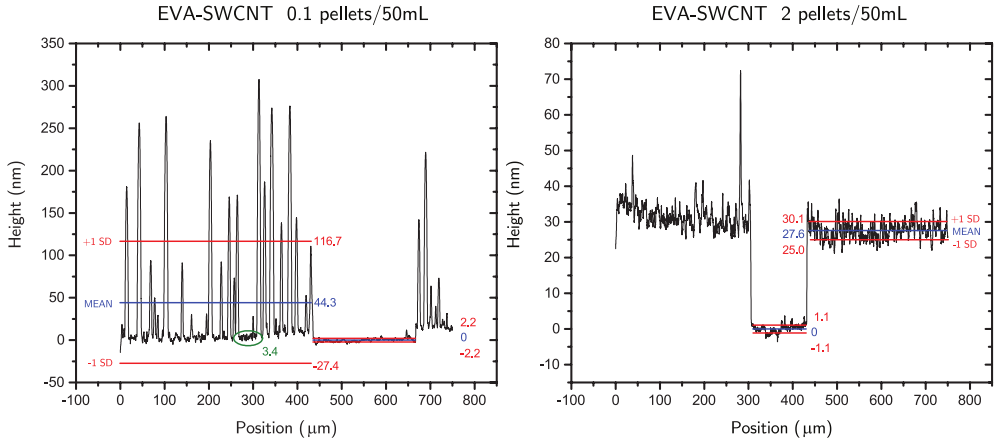

Figure 6.2: Height profiles of EVA-SWCNT films deposited from a solution of 0.1 pellets/50 mL (left) and 2 pellets/50 mL (right). In each graph the blue numbers represent the mean value of the height in the section marked with the blue line, while the red numbers indicate the height 1 standard deviation away from the mean value. While the film deposited from 2 pellets/ 50 mL clearly allows to determine the thickness of the film, when fabricated with 0.1 pellets/50 mL the numerous artefact do not allow to clearly determine the thickness. In the left graph, an additional value is indicated in green, and it represents the mean value of the area in the green circle.

An additional problem in this percolation studies is given by the difficulties in determining the thickness of the films. This can be easily done when the thickness of the film is above 20 nm, but it becomes less trivial when fabricated from very diluted solutions. Figure 6.2 compares the profile measured with a profilometer for a film sprayed from a solution containing 0.1 pellets/50 mL and 2 pellets/50 mL. In both films, the thickness has been measured by scratching the film with a syringe needle and measuring the height difference between the region where material has been removed and the surrounding area. While in a film of about 26 nm thickness it is possible to clearly measure the thickness with a relatively low error, thin films such as those made with 0.1 pellets/50 mL are more difficult to assess. The very low concentration likely delivers a non-complete coverage of the substrate, causing the measuring tip to get blocked and bounce while scanning the sample, resulting in the numerous artefacts shown in the profile. Despite the mean value is 43.5 nm, the

standard deviation is 72.4 nm. A more realistic value of the thickness is the shown in the green circle, where the mean value is 2.6 nm, but this measurement shows that is not possible to have a clear value for the thickness.

The problem of measuring the thickness, necessary to determine the conductivity can be circumvented by studying the 2D problem, as already shown by Hu *et al.*[8] for films of CNT, where the sheet conductance is used instead of the bulk conductivity. The carbon nanotubes density was there defined by the concentration of the solution used to produce the film. The sheet conductance is then expected to be

$$G = \begin{cases} 0, & C < C_0 \\ G_0(C - C_0)^{\alpha}, & C > C_0, \end{cases} \tag{6.2}$$

.

The graphs of Figure 6.3 are built by measuring the transmittance and sheet conductance of several films with different densities, for EVA-SWCNT and EVA-MWCNT. The blue curves represent the fit of Eq. 6.2 obtained with a Levenberg-Marquardt algorithm. The parameters and their standard error of the best fit are summarised in Table 6.1.

	G_0	ΔG_0	C_0	ΔC_0	α	$\Delta\alpha$
EVA-SWCNT	2.12E-5	1.08E-5	0.1	0.34	1.44	0.34
EVA-MWCNT	1.63E-4	4.4E-5	0.1	0.2	1.38	0.26

Table 6.1: Best fit parameters for the percolation curves of Figure 6.3

Experimental data are in agreement with the model. The critical exponents are found to be 1.44 for EVA-SWCNT and 1.38 for EVA-MWCNT. These are both very close (within the standard error) to the theoretical value of 1.33 expected for a 2D percolation, with the value for EVA-SWCNT being slightly higher than EVA-MWCNT. This can be due to the fact that the theoretical percolation model considers paths of conductive sticks having the same characteristics. As shown in the previous chapter the EVA-SWCNTs films are composed of both metallic and semiconducting species,

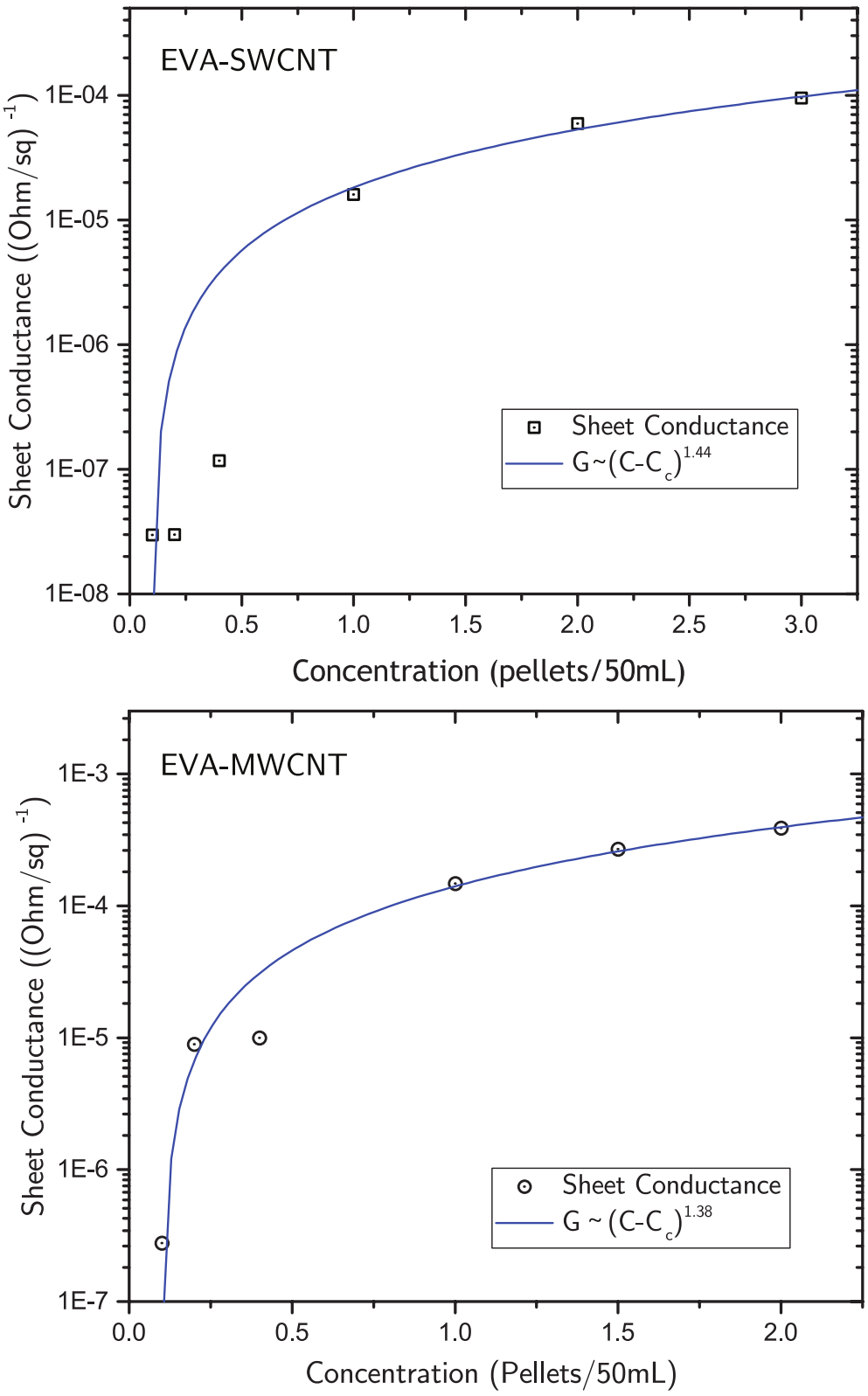

Figure 6.3: Sheet conductance against concentration of the solution used to fabricate the film for EVA-SWCNTs and EVA-MWCNTs film. The squares and circles represent the measured values, while the blue line represent the fit of equation 6.2.

resulting in higher resistance when the junction is between semiconducting-metallic tubes (see section 2.3). On the other side in the EVA-MWCNT samples, the multiple cylinders composing each MWCNT reduces the probability of having large differences in the characteristics of each conductive stick, resulting in a fit closer to the expected values.

The critical concentration has a value of 0.1 pellets/50 mL for both types of films, although the standard error is 340% for SWCNT and 200% for MWCNT. A film with 0.1 pellets/50mL has been fabricated for both. The EVA-SWCNT did not show any conductivity, while a current was measured in the EVA-MWCNT, however values are not reported here as the measurement did not allow to extrapolate a significant value for the sheet resistance due to the large noise, likely due to the impedance of the film being comparable to the input impedance of the instrument ($\sim$10 TΩ).

6.4 DC to optical conductivity ratio

The conductivity measurements also allow to evaluate the properties of the material as a transparent conductor. The relation between the transmittance and the sheet resistance of a thin conductive film can be modelled by[9,10]

$$\mathrm{T} = \left(1 + \frac{\mathrm{Z}_0}{2\mathrm{R_S}} \frac{\sigma_{\mathrm{ac}}}{\sigma_{\mathrm{dc}}}\right)^{-2}, \tag{6.3}$$

where Z_0 is the impedance of free space, σ_{dc} is the direct current conductivity, σ_{ac} is the optical conductivity and R_S is the sheet resistance. The relation is valid when the film thickness is small compared to the wavelength.

The graphs of Figure 6.4 are build measuring the transmittance at 550 nm (where the losses due to the substrate have been removed in this case, as Eq 6.3 only refers to the transmittance of EVA-CNT films).

The fitting allows to obtain the DC to optical conductivity ratio, which is a commonly used figure of merit to compare transparent conductors. The DC conductivity is related to the transport in response to an applied constant field, while the optical

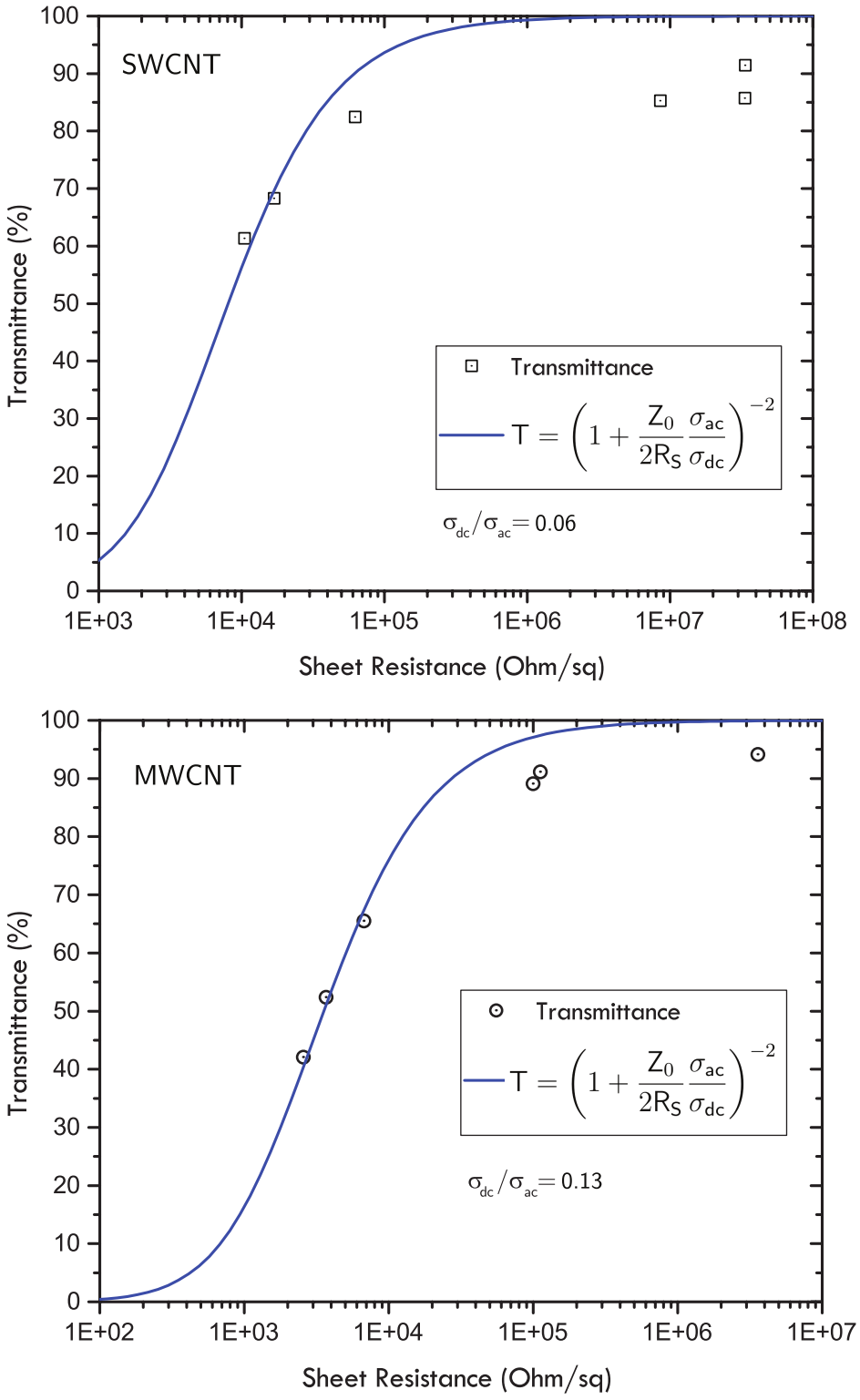

Figure 6.4: Transmittance against sheet resistance of EVA-SWCNTs and EVA-MWCNTs films. The squares and circles represent the measured values, while the blue line represent the fit of equation 6.3, reported in the inset.

conductivity is related to the response of the film to an electromagnetic wave. This figure of merit allows to evaluate different transparent conductors, as it relates the two equally important parameters (sheet resistance and transparency), while it would be otherwise difficult comparing low T - low R_S conductors with high T - high R_S. A good transparent conductor has the highest possible σ_{dc}/σ_{ac} ratio. To give a reference, commercially available ITO film, have a typical σ_{dc}/σ_{ac} of 500.[11]

The fits of figure 6.4 shows a very low value of 0.06 for EVA-SWCNT, and a value of 0.13 for EVA-MWCNT, more than two times higher.

It is worth noting that the model fails for low values of conductivity. This can be due to the fact that the network is likely very sparse for high levels of transparency, while the model assumes a uniform film.

The data confirm the better performance of EVA-MWCNT compared to EVA-SWCNT. This could appear counter-intuitive as the absorbance of MWCNT is higher due to the numerous shells composing each tube. However, a large diameter might offer a better contact between tubes, thus enhancing the conductivity, which is mainly limited by the inter-tubes connections. The better σ_{dc}/σ_{ac} ratio can then to be justified by the superior electrical performances, which compensate for the optical disadvantage.

6.5 Maximum current

Conductivity measurements of carbon nanotubes were taken with a four-point probes setup, as shown in chapter 4. Currents are chosen to avoid voltages above 100 mV/cm, as thermal effects might affect the measurement.[12]

However, exceeding this recommendation can reveal important information on the maximum allowed current in the film. Figure 6.5 shows the I-V curves for films made with different EVA-CNT concentrations.

It can be seen that all the curves show a similar behaviour, having a lower resistance for low values of current and higher resistance for higher currents. The change in

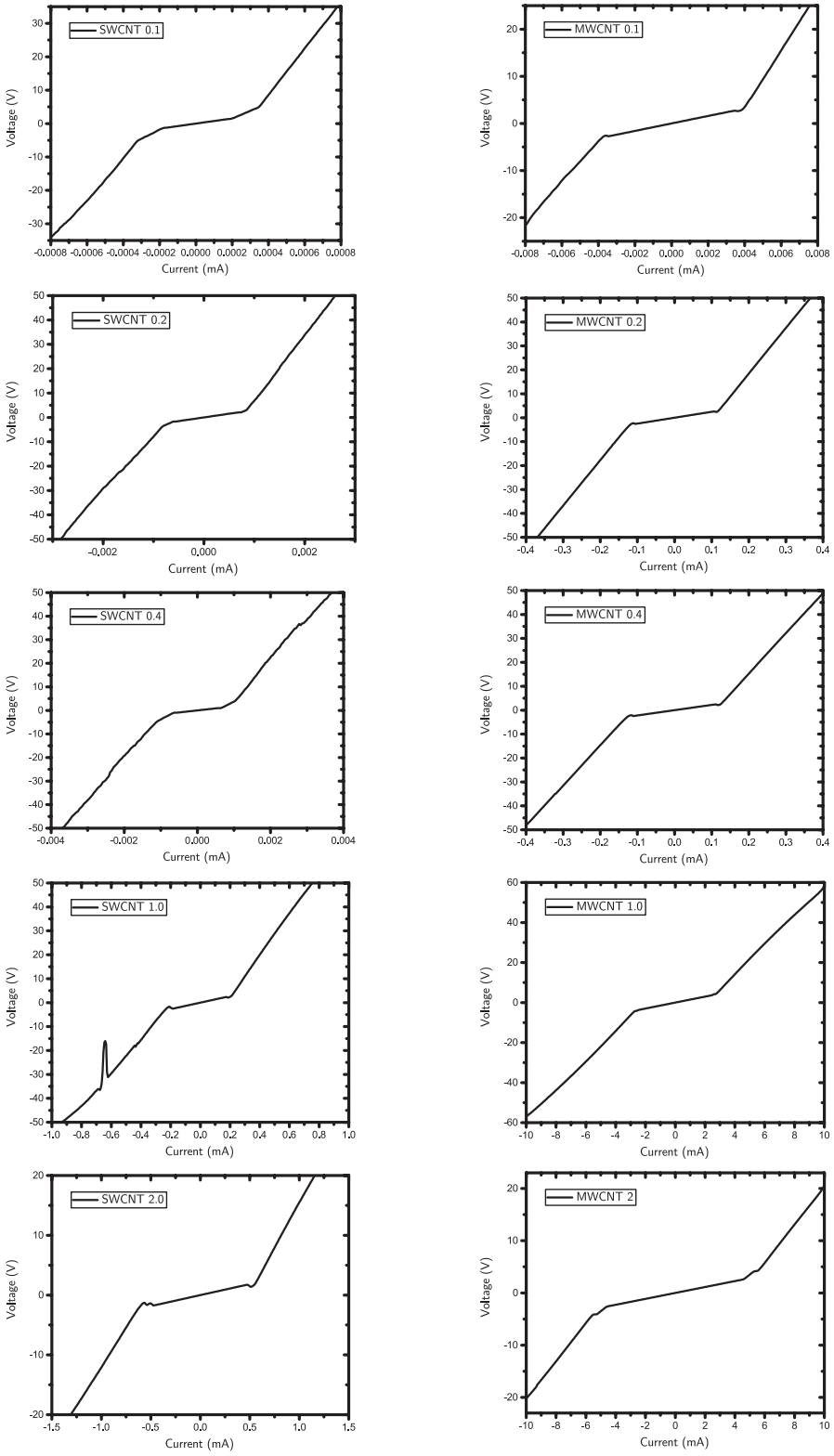

Figure 6.5: I-V curves of the EVA-CNT films. The graphs on the left column represent the I-V curve of 5 films fabricated from EVA-SWCNT solutions, while the right column represent analogous films fabricated from from EVA-MWCNT. From top to botton, each row corresponds to a different concentration used: (0.1, 0.2, 0.4, 1.0, 2.0) pellets /50mL.

resistance does not appear to follow any trend, with the resistance becoming 1-9 times higher for high currents values (values reported in table 6.2).

	SWCNT	**MWCNT**
Conc. (pellets/50mL)	R/R_0	R/R_0
0.1	8.13	7.55
0.2	4.7	7.44
0.4	8.83	7.62
1	5.94	4.98
2	8.13	6.41

Table 6.2: Ratio between film resistance in the high current regime (R) and resistance in the low current regime (R_0)

Reasons for this change in resistivity are unclear. The high symmetry of the curve around 0 A excludes the formation of Shockley barriers, which would result in a diode-like response.

An obvious justification could be found in thermal effect. However, this has to be discarded as an increase of the temperature in carbon nanotubes networks generally corresponds to an increase in conductivity,[13] and the same behaviour is observed in polymer-CNT composites.[14]

It is worth noting that current densities corresponding to the change of slope are extremely high. A quick estimation of the current density can be done considering a probe on a thin film of thickness d, as shown in Figure 6.6. The current density in the cylindrical shell of equipotential is given by $J = I/2\pi rd$.

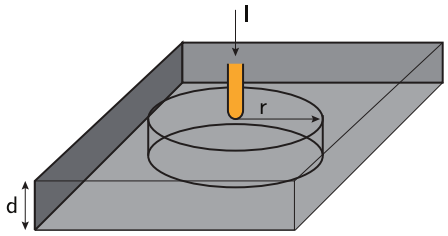

Figure 6.6: Picture representing the equipotential cylindrical shell in a thin film where current is injected by a probe. This model has been used to estimate the current density in the film.

If we consider as an example the film deposited from a EVA-SWCNT solution of 2 pellets/50 ml having a thickness of about 27 nm (height profile in Figure 6.2) and a

change in the I-V slope at 0.7 mA, the resulting current density at 0.65 mm from the injection (i.e. the distance between the probes) is $\sim 1.5 \cdot 10^5$ A/cm^2.

A damage induced by the extremely high current is then possible. However, the change in resistance seems reversible, as I-V sweeps started from the maximum negative, crossed 0 and continued towards the maximum positive current, and reverse scans perfectly overlaps the direct scans. A possible explanation could be a temporary degradation of the interface between the sensing probe (which are in between the probes injecting current) and the film, due to local heating.

Despite the forward and reverse measurement overlap, inspection with the optical microscope clearly shows some degradation on the film when high currents are injected. Figure 6.7 shows the comparison between a typical mark left by a probe on a EVA-MWCNT film when low currents are injected and a similar film where high currents have been injected, where is clearly visible a de-colouration of the area around the contact point.

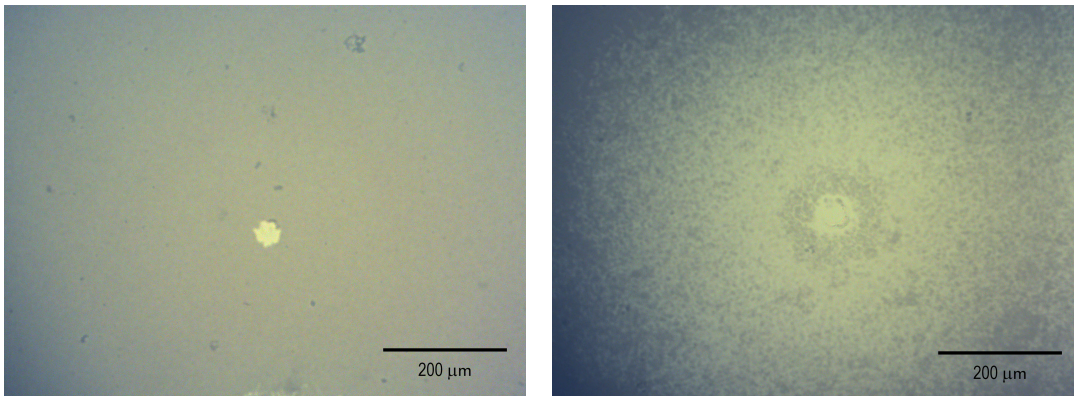

Figure 6.7: Mark left by the testing probe on a film when low (left) and high (right) currents are used. A decoloration around the contact area can be observed in the case of high currents.

To compare the two types of films, the points where the V-I slope change happens have been plotted again the EVA-CNT concentration used to fabricate the corresponding film, shown in Figure 6.8. The points have been found by fitting a linear function in the two different regions of the I-V and calculating the intercept. A power function has been fitted in both graphs to compare the growth of the maximum current before a change in resistance happens.

In both cases the best fit is superlinear, with a faster growth in the case of EVA-SWCNT, ($I \sim C^{1.9}$) and slower for EVA-MWCNT ($I \sim C^{1.3}$). These measurements are not sufficient to offer a model explaining the reason for this differences. However, since the percolation studies show a slightly faster increase of the conductivity in the case of EVA-SWCNT, this could translate in a better tolerance of high currents in these films as the network density increases.

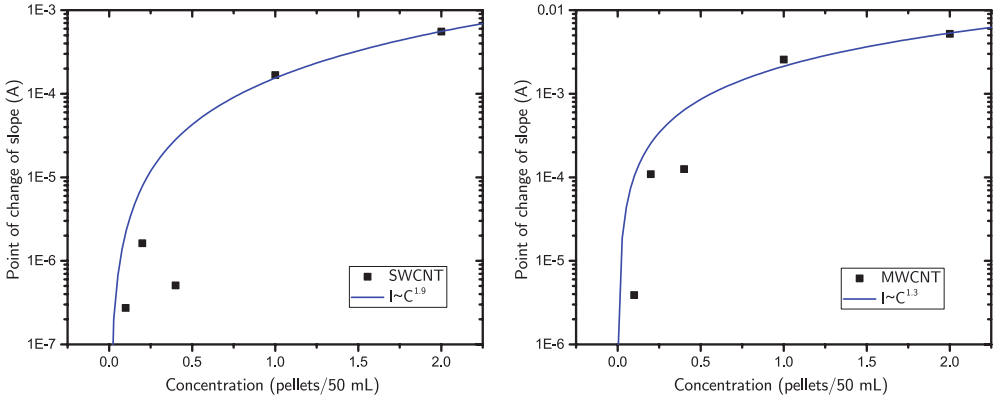

Figure 6.8: Point of change of slope against concentration for EVA-SWCNT and EVA-MWCNT films. The y axes shows the values of current at which a change in the slope in the V-I curve in the positive quadrant is observed. The solid squares show the measured data, while the blue curve is the fit of a power function.

6.6 Conclusions

This chapter showed how it is possible to obtain highly uniform semitransparent conductive film from the EVA-CNT solutions prepared in the previous chapter.

EVA-MWCNT allows to produce films with higher conductivities than EVA-SWCNT (33.8 S/cm compared to 11.9 S/cm), however, their optical absorption is higher when the thickness is the same, having EVA-MWCNT exhibiting a transmittance at 550 nm of 46.8% and EVA-MWCNT a transmittannce of 55.7%.

Percolation studies on films showed a good agreement with the theoretical model, with EVA-MWCNT resulting in a critical exponent closer to the expected value of 1.33 (1.38 for EVA-SWCNT and 1.44 for EVA-MWCNT). This can be interpreted as a higher uniformity of the electrical properties between different tubes, while in

EVA-SWCNT the different chiralities might bring a more heterogeneous landscape, and a more refined percolation model might be needed.

The study of the DC to optical conductivity ratio confirmed the better performances of EVA-MWCNT, exhibiting a σ_{dc}/σ_{dc} value of 0.13 compared to a value of 0.06 for EVA-SWCNT, which despite having a larger optical absorption, they have a better conductivity which compensates for that.

Studies with high currents showed that the film appears to have two different resistances depending on the current regime. The current densities where the change happens are extremely high and in the order of 10^5 A/cm^2, so very far from typical electronic devices applications where currents are in the order of 10^{-3} A/cm^2, but it provides useful information on the limits of the system. The maximum current allowed before the behaviour changes appear to increase faster than the thickness of the film. A model explaining this change in behaviour has not be found. Further temperature-dependent measurements could give a better understanding of the phenomenon, however. These investigations are left for future works, as this effect does not affect the operational regimes of the applications that will be shown in the next chapter.

Bibliography

1. G. Mazzotta, M. Dollmann, S. N. Habisreutinger, M. G. Christoforo, Z. Wang, H. J. Snaith, M. K. Riede, and R. J. Nicholas, "Solubilization of carbon nanotubes with ethylene-vinyl acetate for solution-processed conductive films and charge extraction layers in perovskite solar cells," *ACS Applied Materials & Interfaces*, vol. 11, no. 1, pp. 1185–1191, 2019.

2. Y. Zhou and R. Azumi, "Carbon nanotube based transparent conductive films: progress, challenges, and perspectives," *Science and Technology of Advanced Materials*, vol. 17, no. 1, pp. 493–516, 2016.

3. Z. Zhang, T. Zhai, X. Lu, M. Yu, Y. Tong, and K. Mai, "Conductive membranes of EVA filled with carbon black and carbon nanotubes for flexible energy-storage devices," *J. Mater. Chem. A*, vol. 1, no. 3, pp. 505–509, 2013.

4. D. Stauffer and A. Aharony, *Introduction to Percolation Theory*. London, UK: Tarylor and Francis, 2003.

5. D. Stauffer and A. Aharony, *Introduction to Percolation Theory*. London, UK: Taylor & Francis, 1998.

6. J. P. Clerc, G. Giraud, J. M. Laugier, and J. M. Luck, "The electrical conductivity of binary disordered systems, percolation clusters, fractals and related models," *Advances in Physics*, vol. 39, no. 3, pp. 191–309, 1990.

7. D. J. Bergman and D. Stroud, "Physical Properties of Macroscopically Inhomogeneous Media," *Solid State Physics - Advances in Research and Applications*, vol. 46, no. C, pp. 147–269, 1992.

8. L. Hu, D. S. Hecht, and G. Grüner, "Percolation in Transparent and Conducting Carbon Nanotube Networks," *Nano Letters*, vol. 4, no. 12, pp. 2513–2517, 2004.

9. D. Hecht, L. Hu, and G. Grüner, "Conductivity scaling with bundle length and diameter in single walled carbon nanotube networks," *Applied Physics Letters*, vol. 89, no. 13, pp. 1–3, 2006.

10. M. Dressel and G. Grüner, *Electrodynamics of Solids: Optical Properties of Electrons in Matter*. Cambridge University Press, 2002.

11. S. De, T. M. Higgins, P. E. Lyons, E. M. Doherty, P. N. Nirmalraj, W. J. Blau, J. J. Boland, and J. N. Coleman, "Silver Nanowire Networks as Flexible, Transparent, Conducting Films: Extremely High DC to Optical Conductivity Ratios," *ACS Nano*, vol. 3, no. 7, pp. 1767–1774, 2009.

12. J. K. Hargreaves and D. Millard, "The accuracy of four-probe resistivity measurements on silicon," *British Journal of Applied Physics*, vol. 13, no. 5, pp. 231–234, 1962.

13. K. Yanagi, H. Udoguchi, S. Sagitani, Y. Oshima, T. Takenobu, H. Kataura, T. Ishida, K. Matsuda, and Y. Maniwa, "Transport mechanisms in metallic and semiconducting single-wall carbon nanotube networks," *ACS Nano*, vol. 4, no. 7, pp. 4027–4032, 2010.

14. R. Bhatia, K. Kumari, R. Rani, A. Suri, U. Pahuja, and D. Singh, "A critical review of experimental results on low temperature charge transport in carbon nanotubes based composites," *Reviews in Physics*, vol. 3, no. December 2017, pp. 15–25, 2018.

CHAPTER 7

EVA-CNT films in solar cells as charge extraction layer

7.1 Introduction

As introduced in Chapter 2, one of the most interesting applications of carbon nanotubes is their use in electronic devices. Among these, CNTs in solar cell devices have been widely investigated.

A very successful application was developed by Habisreutinger *et al.*,[1,2] where they managed to use CNTs as an additive in spiro-OMeTAD to replace the lithium salts dopant (Li-TFSI).

The use of spiro-OMeTAD as a hole transporting layer in perovskite solar cells normally relies on the use of Li-TFSI dopants to increase its conductivity, which would otherwise not be enough for an efficient carrier extraction. Habisreutinger *et al.* developed a new system where a film of P3HT-wrapped SWCNTs is deposited on the perovskite layer, and subsequentially infiltrated with undoped spiro-OMeTAD. In

their work they demonstrated that a significant injection of holes photogenerated in the perovskite absorber happens in the P3HT-SWCNT, which were then responsible for the transport to the metal electrode. The two steps deposition turned out to be the best procedure for the solar cell fabrication, with the first step involved the deposition of P3HT-SWCNT, which allows the creation of a dense network directly contacting the perovskite, and the second step involving the filling of all the pores by spiro-OMeTAD, which avoids a direct contact between the perovskite and the metal electrode, which is evaporated on top.

This system has been used here as a benchmark to test the electronic properties of the new EVA-CNTs to understand whether the EVA wrapping individual tubes affects negatively the possibility of using this new nano-hybrid as electronic material. This chapter will illustrate the performances of solar cell using EVA-CNTs as hole transporting layer, with the main scope of understanding whether the substitution of the P3HT impedes the charge transfer from the perovskite to the CNT.

7.2 Device structure

The device structure used in the experiments is shown in Figure 7.1. Light is primarily absorbed in the perovskite layer, which generates excited and free carriers. Depending on the experiment the perovskite was either a mixed cation-mixed anion with $FA_{0.83}MA_{0.17}Pb(I_{0.83}Br_{0.17})_3$ [3] or a $FA_{0.83}Cs_{0.17}Pb(I_{0.9}Br_{0.1})_3$.[4]

Photogenerated electrons are injected in a layer of SnO_2, which allows their transport to the anode while also blocking holes. The anode is a transparent conductor made of FTO deposited on a glass substrate.

Holes are injected in the EVA-CNT layer, which is deposited by spray coating on the perovskite film. Spiro-OMeTAD is deposited on top of the EVA-CNT layer, infiltrating the holes and avoiding a direct contact between the perovskite and the cathode, which is a film of silver or gold.

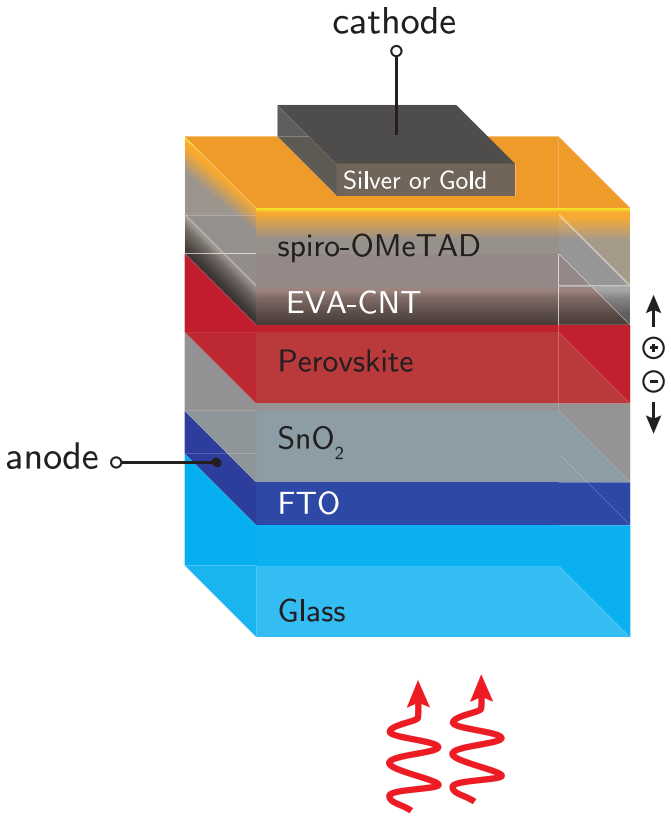

Figure 7.1: Schematic drawing of the perovskite solar cell stack under test. The spiro-OMeTAD is infiltrated in the EVA-CNT film.

7.3 EVA-SWCNTs in $FA_{0.83}MA_{0.17}Pb(I_{0.83}Br_{0.17})_3$ perovskite devices

The first experiment reproduced exactly the structure studied by Habisreutinger *et al.*,[2], employing a perovskite with both mixed organic A-site cations and mixed halides, $FA_{0.83}MA_{0.17}Pb(I_{0.83}Br_{0.17})_3$, and having the structure represented in Figure 7.1, where the cathode was silver. The experiment compared devices with the new nano-hybrid EVA-SWCNT against the P3HT-SWCNT. The P3HT-SWCNT were prepared used CoMoCat CG200 SWCNT instead of the HiPCO used in the EVA-SWCNT nano-hybrids, in order to exactly reproduce the already optimised structure by Habisreutinger.

Two different thicknesses of EVA-SWCNT were compared, a film deposited from a solution of 3 pellets/50 mL (thick) and a film from a solution of 1 pellet/ 50 mL (thin).

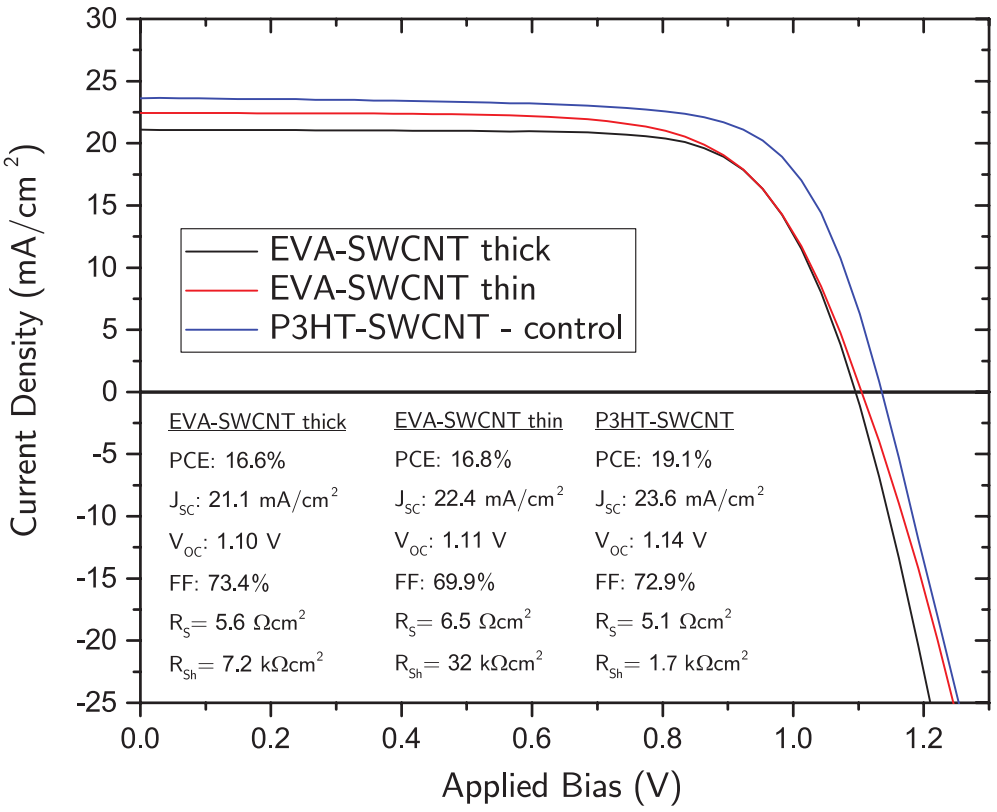

Figure 7.2: JV curves of the $FA_{0.83}MA_{0.17}Pb(I_{0.83}Br_{0.17})_3$ perovskite devices under test. The black solid line shows the characteristic of a solar cell employing a thick layer of EVA-SWCNT, the red solid line a thin layer of EVA-SWCNT and the blue solid line is the characteristic of the control device, employing a layer of P3HT-SWCNT.

The film of P3HT-SWCNT was fabricated dynamically by drop-by-drop spin-coating of 200 μL of solution prepared according to section 4.2.4. The devices were fabricated with the help of Dr Severin Habisreutinger (Department of Physics, University of Oxford), who also fabricated the control devices.

Figure 7.2 shows the JV curves of the best performing devices for each EVA-CNT thickness and the control device. The EVA-SWCNT devices exhibit similar efficiency, with a value of 16.6% in the case of the thin CNTs layer and 16.8% in case of the thick one. The main difference is the slightly higher photocurrent in case of the thin device. A possible justification is given by the smaller optical density of the thin EVA-SWCNT layer, which reduces the parasitic absorption of the back-reflected light which can be absorbed by the perovskite layer once reflected from the cathode. The open circuit voltages are comparable, being 1.10 V for the "thick" device and 1.11 V for the "thin"

device. A big difference is observed in the FF, being 73.4% in the "thick" device and 69.9% in the "thin" device. This is mainly caused by the slightly higher series resistance in the "thin" device (5.6 Ω cm^2 compared to 6.5 Ω cm^2, calculated with a linear fit around the open circuit point), and can the result of a better coverage in case of a thicker EVA-SWCNT layer.

Both devices were outperformed by the control device employing P3HT-SWCNT in the hole-collecting layer. The most important difference is found the the short-circuit current, being 23.6 mA/cm^2 in the control device, and a higher V_{OC} of 1.14 V, with a PCE of 19.1%.

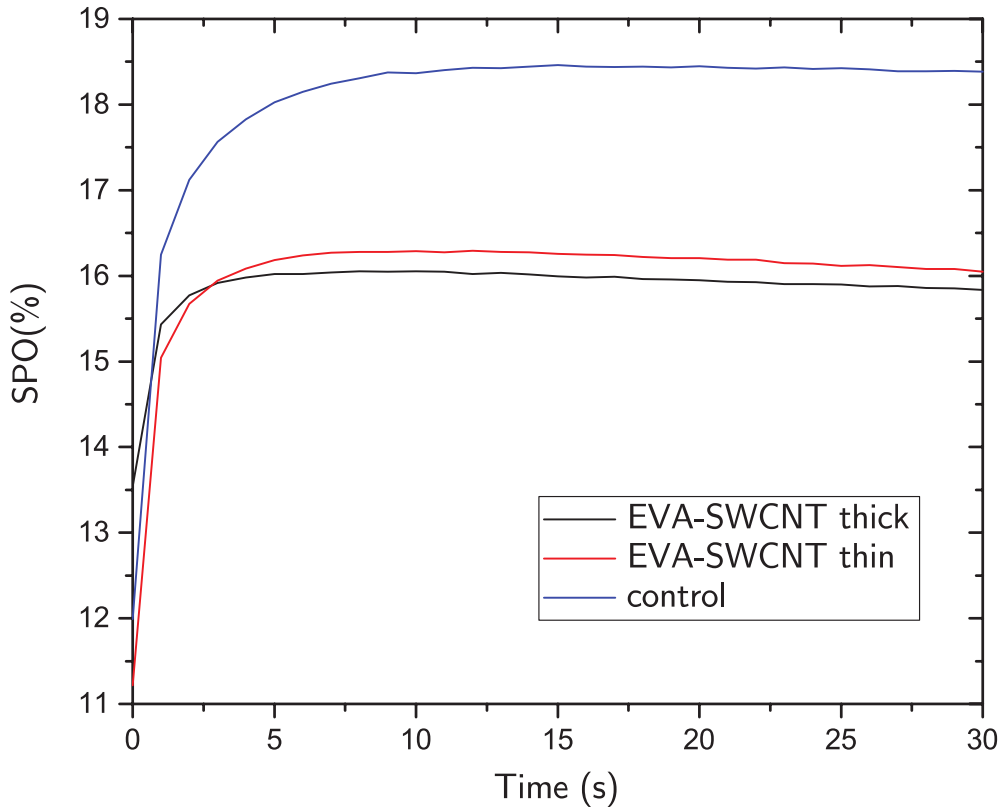

Figure 7.3: SPO of $FA_{0.83}MA_{0.17}Pb(I_{0.83}Br_{0.17})_3$ perovskite devices under test. The black solid line shows the characteristic of a solar cell employing a thick layer of EVA-SWCNT, the red solid line a thin layer of EVA-SWCNT and the blue solid line is the characteristic of the control device, employing a layer of P3HT-SWCNT.

Figure 7.3 shows the SPO of the devices. In perovskite devices, the current-voltage characteristics exhibit a typical hysteretic behavior, with big discrepancies between the forward and the reverse scan.[5] This depends on the testing conditions, mainly

on the sweep scan speed and on the device history such as light soaking and pre-biasing resulting in a difficult comparison between measurements, as the measurement parameters affecting the hysteresis are not regulated by the international measurement standards. A common parameter used to compare solar cells by taking this effect into account is the SPO, obtained by holding the solar cell at the maximum power point voltage (V_{MPP}) for extended time. The SPO for the cell with the thick carbon nanotubes layer and the cell with the thick layer are 15.8% and 16.0% respectively, resulting in SPO/PCE_max of 95.2% for both type of devices, while the control device delivered a SPO of 18.4%, resulting in SPO/PCE=96.3%.

Figure 7.4 shows the statistics of the performance parameters and reflects the observations from the best devices, with the main differences observed in the J_{SC}. The FF is comparable and reaches record values in devices with a thicker layer of carbon nanotubes, which can be due to a better coverage of the perovskite film, allowing for an easier collection of charges thus reducing the series resistance. It is also noticeable that the thinner layer samples showed less device to device variation in the performance parameters.

The most interesting parameters for this study is the V_{OC}, as it is the main indicator of charge recombination in general, but given the comparable stack here it depends on the the perovskite/EVA-SWCNT interface, implying an efficient charge injection. The mean values for the EVA-SWCNT samples differ of about 10mV, and the difference between thin EVA-SWCNT and the control sample is $\sim$ 40 mV. The slightly lower V_{OC} in thick devices could be explained with the lower number of inter-tubes transfers, thus reducing the chance of recombination in thinner devices. The larger difference to the control samples could be explained by the presence of P3HT, which has been observed to shift the Fermi level and p-dope SWCNT.[6] This could lead to an improved band alignment reducing the chance of recombination.

The slightly better SPO/PCE value of the control devices would also confirm this hypothesis, as it is indicative of a decreased charge extraction efficacy.[7,5]

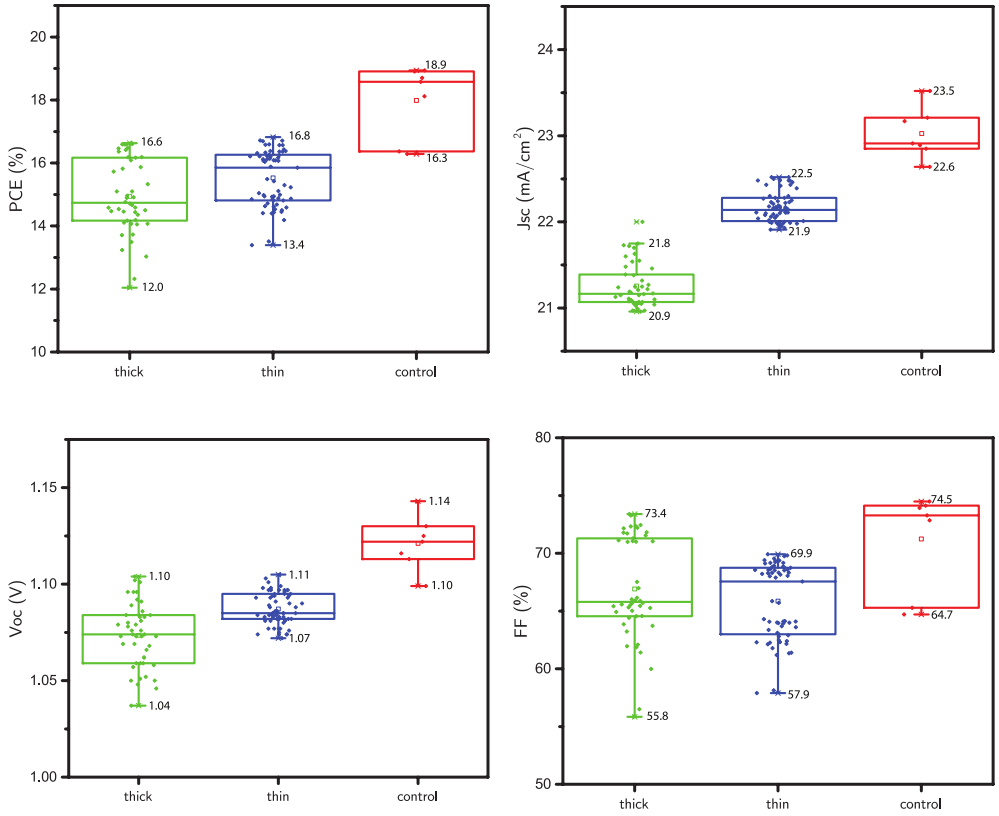

Figure 7.4: Statistics of the performance parameters of $FA_{0.83}MA_{0.17}Pb(I_{0.83}Br_{0.17})_3$ perovskite devices under test. The green box plots shows the statistics of devices employing a thick layer of EVA-SWCNT, the blue box plot corresponds to devices with a thin layer of EVA-SWCNT and the blue box plots are the control devices, employing a layer of P3HT-SWCNT.

However, the losses are minimal, as a heavy interference of the EVA coating on the charge transport is expected to bring much higher drops in the value of the V_{OC}.

Moreover, these devices here containing EVA-SWCNT are a proof of concept and not yet optimised, and a tuning of the fabrication parameters might improve the values observed.

7.4 EVA-CNTs in $FA_{0.83}Cs_{0.17}Pb(I_{0.9}Br_{0.1})_3$ perovskite devices

To test the versatility of the system, the EVA-CNT nanohybrids have also been tested in devices employing a different absorber, the mixed-cation mixed-halide $FA_{0.83}Cs_{0.17}Pb(I_{0.9}Br_{0.1})_3$, which does not contain the MA and which has been widely studied for its better stability.[4,8,9] The device structure is again the same reported in

Figure 7.1, where the cathode is thin gold film. The control device in these experiments uses doped spiro-OMeTAD as hole transporting layer as it is the most optimised material for this absorber, and carbon nanotubes have never been used with it.

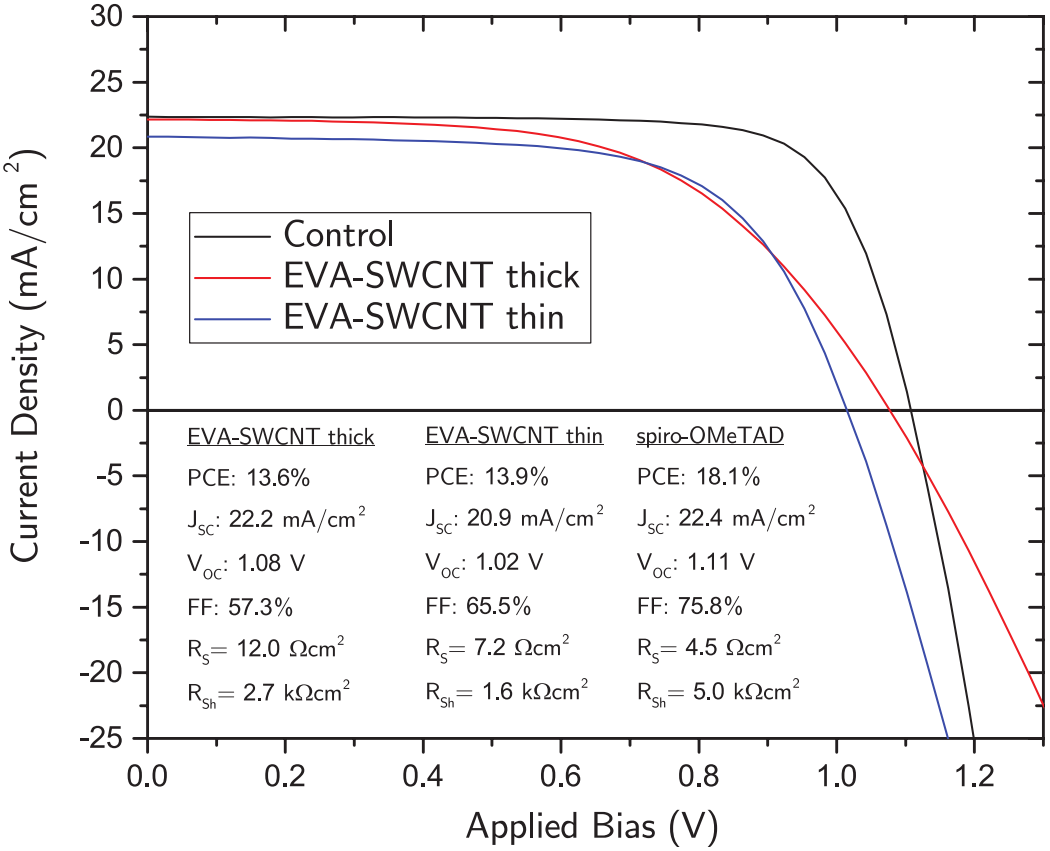

Figure 7.5: JV curves of the $FA_{0.83}Cs_{0.17}Pb(I_{0.9}Br_{0.1})_3$ perovskite devices under test. The red solid line shows the characteristic of a solar cell employing a thick layer of EVA-SWCNT, the blue solid line a thin layer of EVA-SWCNT and the black solid line is the characteristic ofthe control devices, employing a layer of doped spiro-OMeTAD.

In this set of experiments EVA-MWCNTs have also been tested, which have never been used before in this type of architecture. Again two different thicknesses for each EVA-CNT nanohybrids were compared. In the case of EVA-SWCNT the film labelled as "thick" was deposited from a solution of 3 pellets/50 mL, while the "thin" film from a solution of 1 pellet/ 50 mL. In the case of EVA-MWCNT the "thick" film is fabricated from a solution of 2 pellets/50 mL, and the "thin" again from 1 pellet/50 mL. The different choice for the thick layer was derived from the conductivity values reported in the previous chapter, which in the case of EVA-MWCNT are higher. Devices from

this section were fabricated with the help of Dr Zhiping Wang (Department of Physics, University of Oxford), who also fabricated the control devices.

Figure 7.5 shows the JV curves of the best performing devices using EVA-SWCNT as hole transporting layer and the JV curve of the control device with doped spiro-OMeTAD. The performance appears to be much reduced compared to the previous experiment. A thick layer of EVA-SWCNT introduces a large series resistance, which heavily affects the FF, while a thin layer delivers a very low shunt resistance, equally affecting the fill factor and reducing the V_{OC}. Despite the lower performances, the V_{OC} is above 1V in all the devices.

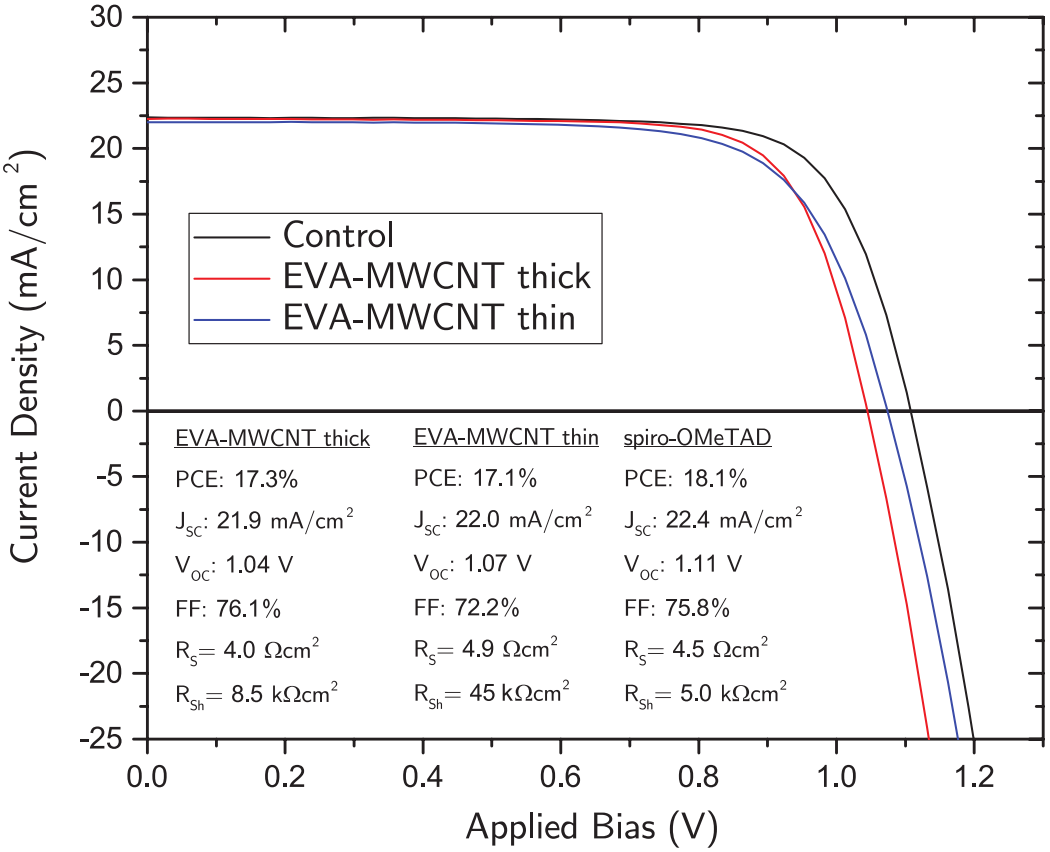

Figure 7.6: JV curves of the $FA_{0.83}Cs_{0.17}Pb(I_{0.9}Br_{0.1})_3$ perovskite devices under test. The red solid line shows the characteristics of a solar cell employing a thick layer of EVA-MWCNT, the blue solid line a thin layer of EVA-MWCNT and the black solid line is the characteristic of the control devices, employing a layer of doped spiro-OMeTAD only.

Figure 7.6 shows the JV curves of the best devices using EVA-MWCNT, with the same control device shown in Figure 7.5. Performances are significantly better than

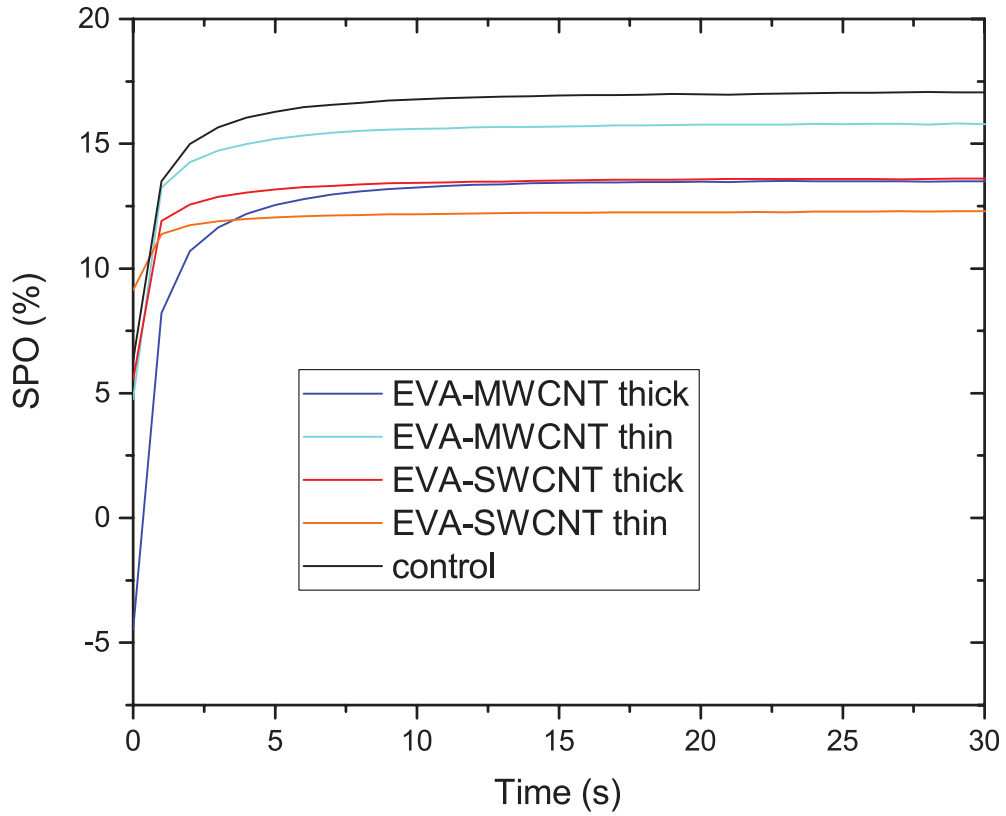

Figure 7.7: Stedy-state power output of $FA_{0.83}Cs_{0.17}Pb(I_{0.9}Br_{0.1})_3$ perovskite devices under test.

devices using EVA-SWCNT, mainly due to the better FF. This is a consequence of the lower series-resistance, very close or better than the control device. The "thick" and "thin" devices show very similar performances, with the main difference observed in the V_{OC} and in the FF.

	SPO (%)	PCE (%)	SPO/PCE
EVA-MWCNT thick	13.5	17.3	0.78
EVA-MWCNT thin	15.8	17.1	0.92
EVA-SWCNT thick	13.6	13.6	1.00
EVA-SWCNT thin	12.3	13.9	0.88
control	17.1	18.1	0.94

Table 7.1: Steady-state power output, power conversion efficiencies and SPO/PCE ratio of the $FA_{0.83}Cs_{0.17}Pb(I_{0.9}Br_{0.1})_3$ perovskite devices.

The SPO of the devices is shown in Figure 7.7, and the SPO/PCE ratio from the JV curves summarised in Table 7.1. It can be seen that despite having the lowest efficiency, devices with a thin layer of the EVA-SWCNT do not show any difference in

the PCE calculated from the J-V curve and the SPO. All the other EVA-CNT devices show a lower SPO/PCE ratio, with the worst ratio given by the thick EVA-MWCNT device.

The statistics of the performance parameters of all the devices described in this section are compared in Figure 7.8. The control device is still the best performing, but the range of efficiency values overlaps with devices containing a thick layer of EVA-MWCNT. The worst performing structure is the one containing a thick layer of EVA-SWCNT, which also shows a very high variability in the values of PCE, J_{SC} and FF. Interestingly, despite this very large variation, the values for V_{OC} are very consistent and above 1V, and outperform the devices with a thick layer of EVA-SWCNT.It can be seen that the main parameter affecting the performances is the FF, being significantly lower than other devices.

The large difference in the performance of devices containing EVA-SWCNT compared to the previous experiments is unclear. The V_{OC} values, lower but comparable to the control device, exclude a significantly higher recombination at the interface between the perovskite and the EVA-SWCNTs. The low fill factor and high shunt resistance suggest a problem of conductivity in the film. An hypothesis justifying this is a possible different surface energy of the $FA_{0.83}Cs_{0.17}Pb(I_{0.9}Br_{0.1})_3$ perovskite used in this section compared to the $FA_{0.83}MA_{0.17}Pb(I_{0.83}Br_{0.17})_3$ used in the previous one, which might affect the morphology of the CNT film. The use of carbon nanotubes in this structure relies on the presence of a percolation path within the CNTs network from the perovskite to the metal electrode.[10] A different surface energy of the perosvkite could lead to a different morphology, resulting in a less rough CNTs film, and the subsequent deposition of spiro-OMeTAD could lead to a less efficient penetration or the creation of a capping layer. A stratification without an efficient penetration of the spiro-OMeTAD in the carbon nanotubes layer would bring to a stack of a highly conductive mesh of CNTs covered by a poorly-conductive undoped spiro-OMeTAD, which would heavily affect the series resistance and the fill factor, resulting in a behaviour as shown in Figure 7.5. This would also explain why a thicker film has

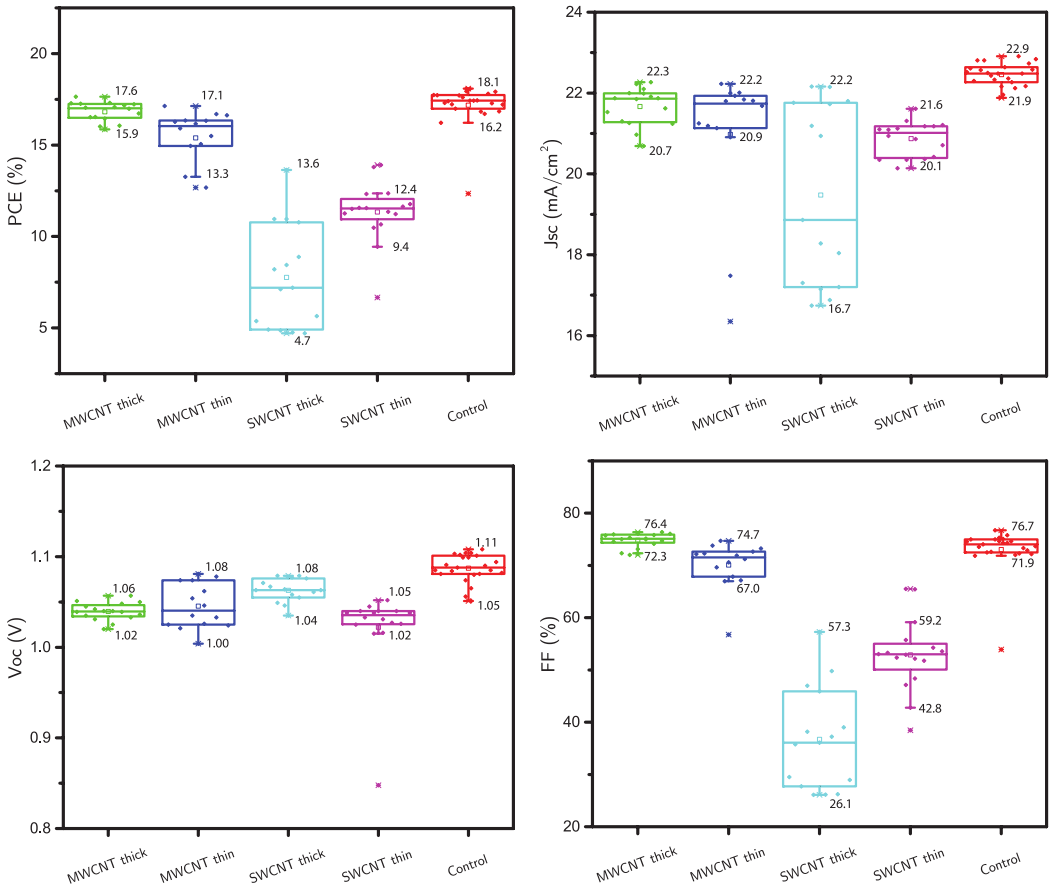

Figure 7.8: Statistics of the performance parameters of $FA_{0.83}Cs_{0.17}Pb(I_{0.9}Br_{0.1})_3$ perovskite devices under test. The green box plots shows the statistics of devices employing a thick layer of EVA-MWCNT, the blue box plot corresponds to devices with a thin layer of EVA-MWCNT. The light blue box plots of devices with a thick layer of EVA-SWCNT, the purple box plot corresponds to devices with a thin layer of EVA-SWCNT, and the light blue box and the blue box plots are the control devices, employing a layer of doped spiro-OMeTAD.

slightly better performance, as it could offer a bigger volume for the spiro-OMeTAD to penetrate. However, more measurements are necessary to confirm this speculation, and characterisation such as AFM microscopy could reveal a different morphology of the CNT film when deposited $FA_{0.83}Cs_{0.17}Pb(I_{0.9}Br_{0.1})_3$) or $FA_{0.83}MA_{0.17}Pb(I_{0.83}Br_{0.17})_3$.

This problem does not seem to affect devices with a EVA-MWCNT film, which have performances very similar to the control device. The most important consideration regarding the use of the material is the possibly low charge selectivity. MWCNT have numerous sub-shells in each tube, offering a larger number of available states which could induce a transfer of electrons from the perovskite and induce recombination. However this characteristic does not seem to heavily reduce the selectivity of the contact, as suggested by the V_{OC} values which are only slightly lower than the control device. The low SPO/PCE ratio in EVA-MWCNT devices would suggest a lower efficiency in the charge extraction, however the better results of the "thin" device would challenge this hypothesis. Further investigations such as time-correlated single photon counting (TCSPC) measurements could answer this question, but within the scope of this experiment it is already possible to affirm that despite the insulating nature of the polymer wrapping the CNT, the new EVA-CNT nanohybrid offer a valid charge extraction layer for perovskite solar cells.

7.5 Conclusions

This chapter investigated the use of the new EVA-CNT nanohybrids in perovskite cells as charge extraction layer.

A first experiment compared the efficiency of $FA_{0.83}MA_{0.17}Pb(I_{0.83}Br_{0.17})_3$ based devices using EVA-SWCNT or P3HT-SWCNT as hole extraction layer, the latter already known to efficiently work in this structure, with the aim of investigating weather the insulating polymer impedes the charge transfer to carbon nanotubes.

The resulting devices delivered a lower efficiency (16.8% compared to 19.1% when P3HT-SWCNT were used), however the lower but very similar values of V_{OC} (1.11 V

for EVA-SWCNT vs 1.14 V for P3HT-SWCNT) suggest a low recombination at the interface.

The comparison of EVA-SWCNT devices with different layer thickness showed that devices with thinner layers delivered a higher currents (22.4 mA/cm^2 compared to 21.1 mA/cm^2), possibly due to the reduced parasitic absorption of the back-reflected light, however the fill factor is lower (69.9% vs 73.4 %), likely due to a better coverage of the perovskite film.

EVA-CNT nanohybrids were also tested on $FA_{0.83}MA_{0.17}Pb(I_{0.83}Br_{0.17})_3$ perovskite devices. This experiments also included EVA-MWCNTs.

EVA-SWCNTs did not perform as well as demonstrated with $FA_{0.83}MA_{0.17}Pb(I_{0.83}Br_{0.17})_3$, with a best PCE of 13.9% compared to the 18.1% of the control device. However, the V_{OC} maintained very high values (with the higest value being of 1.08 V, compared to 1.11 V of the control device), indicating a good charge extraction. The lower efficiency is mainly attribuited to the lower fill factor (65.5% compared to 75.8%), which appears to be caused by a higher series resistance (7.2 Ω·cm^2 vs 4.5 Ω·cm^2), which could possibly derive from a different morphology of the film. A study of the film morphology with AFM and an optimisation of the device is left for future works to verify this hypothesis.

Devices with EVA-MWCNTs delivered an efficiency very close to the control device (17.3% vs 18.1%) and very similar V_{OC} values (1.08 V vs 1.11 V), again indicating a low recombination at the interface.

In conclusion, it has been shown that despite the insulating nature of the EVA polymer wrapping each CNT, this new nanohybrids can be used as an efficient charge exctraction layer in perovskite solar cells. Devices described here are only a proof of concept, and an optimisation of the device has the potential to deliver performances similar to the already established architecture, with the advantace of replacing high-cost semiconducting materials like P3HT with the inexpensive EVA polymer.

Bibliography

1. S. N. Habisreutinger, T. Leijtens, G. E. Eperon, S. D. Stranks, R. J. Nicholas, and H. J. Snaith, "Carbon nanotube/polymer composites as a highly stable hole collection layer in perovskite solar cells," *Nano Letters*, vol. 14, no. 10, pp. 5561–5568, 2014.

2. S. N. Habisreutinger, B. Wenger, H. J. Snaith, and R. J. Nicholas, "Dopant-Free Planar n–i–p Perovskite Solar Cells with Steady-State Efficiencies Exceeding 18%," *ACS Energy Letters*, vol. 2, no. 3, pp. 622–628, 2017.

3. N. J. Jeon, J. H. Noh, W. S. Yang, Y. C. Kim, S. Ryu, J. Seo, and S. I. Seok, "Compositional engineering of perovskite materials for high-performance solar cells," *Nature*, vol. 517, no. 7535, pp. 476–480, 2015.

4. D. P. McMeekin, G. Sadoughi, W. Rehman, G. E. Eperon, M. Saliba, M. T. Horantner, A. Haghighirad, N. Sakai, L. Korte, B. Rech, M. B. Johnston, L. M. Herz, and H. J. Snaith, "A mixed-cation lead mixed-halide perovskite absorber for tandem solar cells," *Science*, vol. 351, no. 6269, pp. 151–155, 2016.

5. H. J. Snaith, A. Abate, J. M. Ball, G. E. Eperon, T. Leijtens, N. K. Noel, S. D. Stranks, J. T.-W. Wang, K. Wojciechowski, and W. Zhang, "Anomalous Hysteresis in Perovskite Solar Cells," *The Journal of Physical Chemistry Letters*, vol. 5, no. 9, pp. 1511–1515, 2014.

6. N. M. Dissanayake and Z. Zhong, "Unexpected Hole Transfer Leads to High Efficiency Single-Walled Carbon Nanotube Hybrid Photovoltaic," *Nano Letters*, vol. 11, no. 1, pp. 286–290, 2011.

7. G. Richardson, S. E. O'Kane, R. G. Niemann, T. A. Peltola, J. M. Foster, P. J. Cameron, and A. B. Walker, "Can slow-moving ions explain hysteresis in the current-voltage curves of perovskite solar cells?," *Energy and Environmental Science*, vol. 9, no. 4, pp. 1476–1485, 2016.

8. Z. Wang, D. P. McMeekin, N. Sakai, S. van Reenen, K. Wojciechowski, J. B. Patel, M. B. Johnston, and H. J. Snaith, "Efficient and Air-Stable Mixed-Cation Lead Mixed-Halide Perovskite Solar Cells with n-Doped Organic Electron Extraction Layers," *Advanced Materials*, vol. 29, no. 5, p. 1604186, 2017.

9. Z. Wang, Q. Lin, F. P. Chmiel, N. Sakai, L. M. Herz, and H. J. Snaith, "Efficient ambient-air-stable solar cells with 2D–3D heterostructured butylammonium-caesium-formamidinium lead halide perovskites," *Nature Energy*, vol. 2, no. 9, p. 17135, 2017.

10. S. N. Habisreutinger, T. Leijtens, G. E. Eperon, S. D. Stranks, R. J. Nicholas, and H. J. Snaith, "Enhanced hole extraction in perovskite solar cells through carbon nanotubes," *Journal of Physical Chemistry Letters*, vol. 5, no. 23, pp. 4207–4212, 2014.

CHAPTER 8

Conclusions and outlook

8.1 Conclusions

This thesis investigated the use of an insulating polymer, EVA, to solubilise carbon nanotubes and produce semitransparent conductive thin films for device applications.

The first chapter studied the solubilisation of carbon nanotubes, both single- and multi-walled, through the use of the EVA polymer. Most of the work in the literature focuses on the individual wrapping of carbon nanotubes with conjugated polymers, while non-conjugated polymers are mainly used as a host matrix for CNT-filled polymers. It has been shown in this work for the first time that this non-conjugated polymer can individually solubilise carbon nanotubes, and through solvent engineering, it is possible to purify the material removing the unbound polymer, resulting in a dispersion of polymer-wrapped CNT. The analysis of the shift of the CNTs PL peaks showed that the polymer is inducing a mechanical stress on the nanotubes, suggesting then a tight bond, confirming the polymer wrapping. The wrapping mechanism does not appear to be selective for a specific chirality, as shown by photoluminescence excitation (PLE)

and Raman measurements, the latter also indicating a slight preference for the polymer to solubilise metallic nanotubes.

The second chapter investigated the electrical properties of such CNT films. The dispersion obtained by solubilising the CNTs with the EVA polymer enables the production of very uniform films by spray-coating. The films are semi-transparent and, despite the insulating polymer, delivered conductivities of 11.9 S/cm for EVA-SWCNT films and 33.8 S/cm for EVA-MWCNT films, which is two orders of magnitude higher than ever reached with this combination of materials. This values allow to produce semitransparent conductive films, which could be use for conductive coatings. The spray-coating allows a very fine control of the film, and this was used to produce films with different CNTs densities and thicknesses. Percolation studies on this film showed a good agreement with a 2D percolation model, with a better fit in the case of EVA-MWCNT films. The studies of the sheet resistance in relation to the transmittance measurements revealed the better qualities of EVA-MWCNT as a transparent conductor, with a DC to optical conductivity ratio of 0.13, compared to 0.06 of EVA-SWCNT, due to the higher conductivity shown by the EVA-MWCNT. Moreover, it was shown that the film can tolerate very high current densities (in the order of 10^5 A/cm^2) before a change in the electrical properties happens. This allows to use the materials in electronic devices, where current densities are 8 orders of magnitude lower, and opens the potential to applications where higher currents are needed, such antistatic coatings.

The last part of the thesis studied the use of this new EVA-CNT nano-hybrid in electronic devices. Specifically, it was investigated whether the use of an insulating polymer wrapping individual tubes prevents the use of the nanotubes as a hole transporting material in perovskite solar cells. A $FA_{0.83}MA_{0.17}Pb(I_{0.83}Br_{0.17})_3$ perovskite device using P3HT-SWCNTs as a hole extraction layer was chosen as a benchmark test architecture, and it was studied whether the new EVA-SWCNTs can replace P3HT-SWCNTs. Although devices with EVA-SWCNTs result in lower efficiencies, the good values of the V_{OC} (above 1 V) showed that the insulating polymer does not

impede the holes extraction, demonstrating the good quality of this new nano-hybrid. From this result, additional tests were conducted on a different perovskite absorber, $FA_{0.83}Cs_{0.17}Pb(I_{0.9}Br_{0.1})_3$, to show the versatility of the technology. This second test also included EVA-MWCNTs, which have never been used in similar structures before. The experiment confirmed the ability of the EVA-CNTs to extract and transport holes, however device efficiency and reproducibility when EVA-SWCNTs was lower than the previous experiment. Despite the lower efficiency (PCE=13.9% compared to PCE=16.8% for the previous experiment), V_{OC} was again consistently above 1 V, indicating a good charge selectivity of the EVA-SWCNT layer, and the poor performance was speculated to be caused by a non optimised structure, however this hypothesis needs to be confirmed by additional studies. By contrast, EVA-MWCNTs outperformed the EVA-SWCNTs and delivered efficiencies very close to the control devices (above 17%), showing for the first time that EVA-MWCNT can be used in this architecture.

8.2 Outlook

The work of this thesis showed that a simple insulating polymer like EVA can replace a conjugated polymer in polymer-wrapped CNTs, with no significant degradation of the electronic properties of the film, re-evaluating the required properties of wrapping polymers for carbon nanotubes in electronic devices. The majority of the work in the literature focuses on π-conjugated polymers, as the $\pi - \pi$ interaction is thought to be one of the main mechanisms driving the wrapping process. It was hypothesized in this work that the binding between EVA and CNT could be induced by the interaction of the π-orbitals of the CNT and the numerous -CH groups on the polymer. However, this hypothesis needs to be verified by additional studies. Tests with polymers rich in -CH groups and different chain stiffnesses could clarify the process. Additional measurements using FTIR or Raman spectroscopy, with a specific focus on the frequencies associated with the -CH vibrations could provide useful information about

this hypothesis, as the vibrations are expected to change if a strong interaction with the CNT happens.

The studies on the electrical properties of these new nano-hybrids showed some potential for it being used in thin films as a semitransparent conductor, as the high transparency of the wrapping polymer offers an optical advantage compared to the majority of conjugated polymers, which tend to absorb light in the visible region. However, transparency and sheet resistance values are at this point not enough to replace conventional transparent electrodes such as ITO or FTO. Studying the effect of the length of the CNT, for example replacing the HiPCO tubes with ultra-long CVD-grown tubes could clarify whether this system can reach the transparency and conductivity values required to replace transparent conductive oxides. Additionally, the use of dopants such as MoOx or NH_3, which have been shown to decrease the resistivity of these films by several orders of magnitudes,[1] could improve the performances.

The use of the EVA-CNTs offers a route to drastically decrease the cost of the hole transporting layer, as replacing a conjugated polymer like P3HT with a widely produced insulating polymer like EVA could potentially reduce the cost of different order of magnitude (e.g. from $\sim$800 £/m^2 for P3HT-SWCNT to $\sim$70 £/m^2 for MWCNT/EVA with the lab-scale process described in this thesis, with the realistic potential of a further ten-fold reduction on a large scale production). The devices shown in this thesis were a proof of concept, and an optimisation of the fabrication parameters will be necessary to understand the real potential of this material. The very large hydrophobicity of the EVA polymer might be of additional benefit, as it adds protection to the active layers, and the use of the same EVA polymer to fill the gaps within the CNT mesh, resembling the structure developed by Habisreutinger *et al.*[2] might offer a new inexpensive protective electrode.

Additionally, the easy and inexpensive process shown in this theses has a lot of future potential beyond electronic applications , as the solubilisation of carbon nanotubes in organic solvents can be used from research to commercial applications

where an easy deposition of a well dispersed network of carbon nanotubes can improve the mechanical and electrical properties of materials.

Bibliography

1. L. Yu, C. Shearer, and J. Shapter, "Recent development of carbon nanotube transparent conductive films," *Chemical Reviews*, vol. 116, no. 22, pp. 13413–13453, 2016. PMID: 27704787.

2. S. N. Habisreutinger, T. Leijtens, G. E. Eperon, S. D. Stranks, R. J. Nicholas, and H. J. Snaith, "Carbon nanotube/polymer composites as a highly stable hole collection layer in perovskite solar cells," *Nano Letters*, vol. 14, no. 10, pp. 5561–5568, 2014.